DEVELOPMENT OF FABRICATION PLATFORM FOR MICROFLUIDIC DEVICES AND EXPERIMENTAL STUDY OF MAGNETIC MIXING AND SEPARATION

by

Athira Nair Surendran

A Thesis

Submitted to the Faculty of Purdue University

In Partial Fulfillment of the Requirements for the degree of

Master of Science in Mechanical Engineering

Department of Mechanical and Civil Engineering

Hammond, Indiana

December 2020

THE PURDUE UNIVERSITY GRADUATE SCHOOL
STATEMENT OF COMMITTEE APPROVAL

Dr. Ran Zhou, Chair

Department of Mechanical and Civil Engineering

Dr. Xiuling Wang

Department of Mechanical and Civil Engineering

Dr. Wubeshet Woldemariam

Department of Mechanical and Civil Engineering

Approved by:

Dr. Chenn Zhou

ACKNOWLEDGMENTS

First and foremost, I would like to express my sincere gratitude to my graduate advisor, Dr. Ran Zhou for providing me an opportunity to pursue my postgraduate degree at Purdue University. Her vision, dedication and motivation have inspired me to work hard during my postgraduate degree. Her guidance and patience have taught me about the bigger things in life and to always strive for the best. She has taught me invaluable knowledge that I will utilize in the foreseeable future. I would also like to thank her for her friendship and empathy. I will always be grateful to her for believing in me and funding me to be her graduate assistant.

I am extending my thanks to Professor Xiuling Wang and Professor Wubeshet Woldemariam for for serving as my committee members and lending their time, knowledge and expertise to my work; my friends, Ashreet Mishra, David Okposio, Obinna Aronu, and Kene Mozea for their helpful contributions during the course of my research work. This thesis is supported by the Start-up package from School of Engineering at Purdue University Northwest.

My deep appreciation for all my professors in the Mechanical and Civil Engineering department for their guidance during my courses. I am grateful for my parents, Surendran and Susila, sister, Bhaagya Nair, boyfriend Jesus Loe Jr and best friend Shaspreet Kaur for their unconditional love and support throughout my journey.

TABLE OF CONTENTS

LIST OF TABLES

LIST OF FIGURES

NOMENCLATURE

A	Magnetic potential
B	Magnetic flux density
C	Concentration of ferrofluid
C_m	Mixing degree
d	Depth of microfluidic channels and microstructures
d_p	Diameter of LED mount on the exposure platform
d_{LED}	Diameter of a single LED light
d′	Distance between the wall of the channel and the bottom surface of microparticle
$\mathbf{F}_b$	Buoyant force
$\mathbf{F}_d$	Drag force
$\mathbf{F}_g$	Gravitational force
$\mathbf{F}_m$	Magnetic force
f_D	Hydrodynamic drag force coefficient
g	Smallest distance between micromagnet and microchannel in single layer device
g	Gravitational acceleration
H_c	Coercivity
H	Magnetic field intensity
h	Height between master mold and light exposure platform
h_m	Height of rectangular magnetic structure in single layer device
h_p	Thickness of exposure platform
h_{LED}	Height of a single LED light
I	Light intensity
j	Width of magnetic connecting bar for rectangular structures in single layer device
λ	Wavelength
L	Length of single layer microchannel
l_g	Width of a gap between micromagnetic bars in two-layer magnetic array
l_m	Width of a single micromagnetic bar in two-layer magnetic array
μ	Dynamic viscosity
μ_r	Relative permeability

μ_0	Permeability of free space = $4\pi\times10^{-7}$ H/m
$\mathbf{M}_p$	Field-dependent particle magnetization
M_s	Saturation magnetization
$\mathbf{m}_p$	Dipole moment microparticle
N	Total number of pixels in the image
n	Width of micromagnetic array in two-layer device
η	Dynamic viscosity of the fluid
P	Pressure
ρ	Density of the fluid
ρ_f	Density of the fluid
ρ_p	Density of microparticle
Q	Total volumetric flow rate
r	Radius of the microparticle
σ	Electrical conductivity
t_d	Development time
t_e	Exposure time
u	Vertical distance between two rows of LED light mounts
$\mathbf{u}$	Velocity of the fluid
$\mathbf{u}_f$	Velocity of the fluid
$\mathbf{u}_p$	Velocity of the particle
v	Horizontal distance between two columns of LED light mounts
V_p	Volume of microparticle
w	Width of microchannel
w_m	Width of single rectangular magnetic structure in the single layer device
w_g	Gap between rectangular magnetic structures in the single layer device
X_i	Intensity of each pixel in the image
$\bar{X}$	Average intensity of all the pixels
χ_f	Magnetic susceptibility of undiluted ferrofluid
χ_p	Magnetic susceptibility of microparticle
$\Delta\chi$	Difference in magnetic susceptibilities between the magnetic microparticle (χ_p) and surrounding fluid (χ_f)

ABSTRACT

Microfluidics is a new and emerging field that has applications in a myriad of microfluidic industrial applications such as biochemical engineering, analytical processing, biomedical engineering and separation of cells. Microfluidics operations are carried out in microfluidic chips, and the traditional method of fabrication is carried out in a cleanroom. However, this fabrication method is very costly and also requires professional trained personnel. In this thesis, a low-cost fabrication platform was developed based on soft-lithography technique developed to fabricate the microfluidic devices with resolution at microscale. This fabrication method is advantageous and novel because it is able to achieve the microscale fabrication capability with simple steps and lower-level laboratory configuration. In the developed fabrication platform, an array of ultraviolet light was illuminated onto a photoresist film that has a negative photomask with a microfluidic design on it. The photoresist film is then developed, and a silicon polymer of polydimethylsiloxane (PDMS) is chosen to be the material for the device. In this work, the performance and resolution of the fabrication system was evaluated using scanning electron microscopy (SEM), polymer resolution test and light intensity analysis.

Based on the success of the development of microfluidics fabrication platform, various experiment of mixing and separation was conducted and studied because the utilization of the microfluidic device for mixing and separation is very valuable in biomedical and chemical engineering. Although there are a lot of applications reported, the precise separation and mixing at microscale still meet some difficulties. Mixing in micromixers is extremely time-consuming and requires very long microchannels due to laminar flow and low Reynolds number. Particle separation is also hard to be achieved because the size of micron bioparticles is very small and thus the force is not strong enough to manipulate their motion. The integration of magnetic field is an active method to strengthen both mixing and separation that has been widely applied in the biomedical industry overcome these difficulties because of its compatibility with organic particles. However, most magnetic mixing and separation use bulky permanent magnets that leave a large footprint or electromagnets that generate harmful Joule heat to organic and bio-particles. In this work, microscale magnet made of a mixture of neodymium powder and polydimethylsiloxane was developed and integrated into microfluidic system to achieve both rapid mixing of ferrofluids and separation of microparticles. Systematic experiments were conducted to discuss the effect of

various parameters on the performance of magnetic mixing and separation of microparticles. It was found that channel geometry, flow filed, and magnetic properties will affect the transport phenomena of ferrofluid and microparticles, and thus mixing and separation efficiency. These findings are of great significance for the high throughput sorting of cancer cells and its mixing between drug for therapy treatment.

1. INTRODUCTION

1.1 Overview of Microfluidics

Microfluidics is not only a new and emerging field in fluid mechanics, which was discovered only 30 years ago but it has multiple applications ranging from biomedical to chemical engineering [1],[2],[3],[4]. Krupenkin [5] published a patented project using microfluidics as a means to convert mechanical energy from working fluid into electrical energy. Parikesit et al. [6] developed a textile-based microfluidics platform to enhance paper-based and thread-based microfluidics. They investigated the feasibility of textile-based microfluidics by applying them to energy harvesting, liquid sorting, liquid mixing and modulated wetting. Next, Schiphorst et al. [7] proposed a low-cost method to fabricate microfluidic parts that usually have a high cost, such as pumps and valves, by integrating light-responsive material. It was found that by incorporating light-responsive materials to active parts in the device, the cost of the device was significantly reduced. Zhang [8] investigated the applications of microfluidics in the biological field using hydrogels. The properties of hydrogel are advantageous in microfluidics because of their temperature sensitivity and biocompatibility. However, this team has a deeper analysis on other significant advantages of gel-incorporation in microfluidics, that could potentially have benefits in industrial applications.

Microfluidics can be divided into two sections, which are passive and active methods, where passive method uses hydrodynamic forces and the geometry of the microchannels to manipulate fluids and particles, while active methods use external forces and fields to control fluids and particles. Examples of passive methods involves chaotic advection and spiral fluidic channels that creates a large inertial force on the fluids inside [9]. Examples of active methods include using magnetic, electrical, and acoustic fields.

The present work is focused on an active method of mixing reagents and separating magnetic particles. In this section, the fabrication of microfluidic devices will be discussed. Then, the applications of microfluidic devices in mixing reagents, followed by separating particles will be introduced.

1.2 Fabrication of Microfluidic Device

The fabrication of a microfluidic chip can vary depending on the usage of the chip. In the early ages of microfluidics, the chips were manufactured and fabricated in the cleanroom. A Class 10 (ISO 4) cleanroom can contain a maximum of 83 particles sized 1μm or larger [10]. This setup is suitable for most of the earlier technologies of fabrication of microfluidic devices and typically costs $300 per square foot due to the special fixtures and filter requirements to achieve a level of sanitation as high as ISO 4 [11]. Furthermore, individuals using a cleanroom need to be trained by specialized personnel to ensure the maintenance of the cleanroom and also for efficient fabrication process. Cleanroom was necessary during the discovery of this field because of the sensitivity of microfluidic chips as the resolution of the device depends on the quality of fabrication. Without a cleanroom, particles and dust in room air can be trapped in the microfluidic devices, which detriments the performance of the device. However, this leads to a higher cost in the fabrication and manufacturing these devices.

Fortunately, many current methods do not require the usage of a cleanroom for the fabrication of microfluidic devices [12]. There are a number of fabrication methods proposed in previous works such as the method of lamination, where multiple layers of laminates are bonded together to create microchannels [13]. This method laminates polymers and plastics which are cut precisely typically using a laser cutter, which are then aligned and bonded to other polymers using adhesives or thermal bonding. The alignment step is crucial in this method because a slight discrepancy in alignment can alter the geometry of the microfluidic channels and structures.

The next microfabrication method is injection molding where thermoplastic is converted from solid to liquid phase in a compression chamber [14]. Then a mold cavity typically made from micro milled metal is created in the middle of two casts in the required shape and size for the microfluidic channel. The molten thermoplastic is then injected into the mold cavity to replicate the shape of the microfluidic channels and structures. After the thermoplastic has cooled down, the cast is removed, and the microfluidic device is ready to be experimented. This method restricts the material to be thermoplastics, which restricts the applications of the resulted microfluidic device. Another method is the hot embossing, where thermoplastics in a high temperature and high-pressure environment are utilized to create microfluidic devices [15]. A solid thermoplastic film is placed in an empty mold chamber. The chamber is then passed through a phase of elevated pressure and temperature. This melts the thermoplastic, which conforms to the shape of the mold,

creating a thermoplastic cast. The cast is then cooled and removed from the mold, ready to use. The advantages and disadvantages are the same as the injection molding method because of the similar fabrication technique and material selection.

The next fabrication method is called etching, where a strong acid removes uncovered material on a surface. Etching is divided into two parts, wet-etching and dry-etching. Wet etching uses a liquid chemical to remove material from a surface [16]. A metal sheet is cleaned to remove oxides and particles. A photoresist is coated onto the metal sheet. Two pieces of clear film containing the microfluidic geometry is placed on top and on the bottom of the metal sheet, respectively. The alignment of this setup is important to ensure a high-quality fabrication. The setup is exposed to ultraviolet (UV) light and the photoresist that is exposed to the light becomes hardened. The unexposed photoresist is dissolved, and the developed metal sheet is passed through an etching machine, where an etchant (strong acid) is sprayed onto both sides of the sheet. When the etchant and metal interact, the metal dissolves and only the metal bonded to the photoresist remains. Finally, the resist is removed by applying resist stripper and a metal sheet of microfluidic device remains. This method is also called photochemical machining. A newer method of etching is called dry etching, where a strong acid is replaced by reactive ions for the etching process to dissolve the metal [17].

Recent printing technologies allow for newer advances in the microfluidic fabrication techniques, namely 3D printing. Multiple modeling methods have been developed to utilize 3D printing for microfluidics such as stereolithography and multi jet modeling. Stereolithography creates fine structures using a structured light source on a vat of resin that can be developed into many layers [18]. Multi jet modeling uses photosensitive resin that creates layers of structures. A droplet of resin is deployed onto a surface and a laser beam is illuminated to cure the photosensitive resin. This process is repeated for a number of droplets until the desired height is achieved [19].

Photolithography, which is similar to the method proposed in the present work, uses UV light to transfer microchannel shapes to a silicon wafer [20]. First, the wafer is treated with hydrogen peroxide to remove any contamination. A layer of silicone is placed on top of the wafer, which is now called a silicon wafer. The photoresist adhesion is increased by applying hexamethyldisilazane (HDMS), a type of primer, on the silicon wafer prior to spin coating a photoresist on the silicone. UV light is used to illuminate the photomask containing the microstructures needed for the microfluidic chip. Exposed photoresist is washed, and the

unprotected silicon is chemically removed. The photoresist is also removed chemically to expose the silicon. To create a chip, silicon dioxide is coated on the silicon to add more structures to the chip.

Although a cleanroom is not required for recent techniques, the cost of fabrication and training requirement are still high. Soft lithography is similar to photolithography, but it delivers high resolution microfluidic chips while keeping costs low [21].

In the present work, a low-cost method based on soft lithography was developed to fabricate high resolution microfluidic chips. This method uses a polymer known as polydimethylsiloxane (PDMS) to mold the shape of the microfluidic channel. On a clean copper plate, a dry photoresist film is illuminated, and the unexposed parts are dissolved. PDMS is poured onto the copper plate and cured, resulting in a microfluidic chip with a high resolution. After fabricating a microfluidic device, operations such as mixing fluids, focusing, sorting and separation of particles can be carried out for applications in different fields. The advantages of the developed fabrication platform are low cost of manufacture, feasibility of fabrication where minimal training is required to manufacture the devices and sustainability of the devices because the devices can be reused multiple times successfully.

1.3 Mixing of Fluids on a Microscale

One of the applications of microfluidic devices is mixing. Mixing in microfluidics is beneficial in fields such as pharmaceutical and biomedical engineering. Mixing of reagents is an important step in many processes in the biomedical field, such as polymerization, extraction, purification, chemical synthesis and reaction [22]. It is also the preliminary step before proceeding to focusing, separating, and sorting cells. Mixing in microfluidics is a huge attraction towards researchers because of the enigmatic issue that comes with microfluidics, which is laminar flow. Since the width of the channels are miniscule, the corresponding Reynolds number for all microfluidic channels is small, which means laminar flow is prominent. On a macro scale, laminar flow is more desirable compared to turbulent flow because turbulent flows cause a lot of mechanical issues in components present in pipelines and wind turbines. However, the opposite is true on a microscale where turbulent flow is necessary for mixing of different fluids.

The mixing degree of fluids with different properties is low on a micro level, where the only means of mixing is by molecular diffusion. Mixing in this method consumes a long reaction time,

long channel length, and a large sample size. Turbulent flow accelerates mixing time, shortens the length of channels and only require a small sample size. Hence, numerous methods have been developed to induce turbulent flow and in turn increase mixing on a micro scale. The degree of mixing is calculated using different methods and criteria, but the most common methods are the time taken for complete mixing to occur and the degree of homogeneity at the outlet of the channel.

Mixing can be categorized into two parts, which are the active and passive methods. Examples of passive methods include microfluidic channels that cause inertial forces and chaotic advection. Yang et al. [23] developed a 3D micromixer that uses the principles of inertial forces through spiral microchannels. They combined two spiral channels to maximize inertial forces and minimize the size and footprint of the device. Clark et al. [24] investigated the Dean flows in non-rectangular channels with serpentine geometry. Passive methods have an advantage compared to active methods, in which they do not rely on external forces, instead they depend on their inherent fluid properties and channel geometry to increase mixing efficiency.

However, active methods have proven to have a faster and higher performance. First, electrical field creates chaotic electrical fields and discrepancies in the midst of the flow field to create advection. Lynn et al. [25] applied a localized electrical field perpendicular to the flow field to create a helical motion as a result of the reaction between the flow field and the electrical field. This created a disruption in the flow and resulted in a complete mixture. Chen and Cho [26] designed a mixing chamber with a rectangular cross section. They applied uniform electrical field to the four corners of the rectangular cross section and resulted in complex flow behavior and a high mixing performance.

The next active method is the usage of acoustic field produced by piezoelectric transducers to create a micromixer. Yeo and James [27] investigated the sound waves resonating from the side wall of microchannels using surface chaotic waves (SAW). This then induces chaotic oscillation in the fluid field, resulting in complete mixing. Ahmed et al. [28] designed a microchannel that has grooves on the sidewall. The purpose of these grooves is to trap microbubbles which are then spun by the external acoustic field. This results in the mixing of fluids due to microstreaming that is caused by the air bubbles.

Thermal field uses thermal microbubbles and thermoelectricity to induce mixing. Kunti et al. [29] designed a micromixer that is semi active and semi passive using an alternating current electrothermal micromixer. Pairs of electrodes were placed on the top and bottom walls of the

channel, with an addition of grooves on the bottom wall of the channel. Alternating current is fed to the electrodes, which then increased the temperature and caused mixing. Ajarostaghi et al. [30] performed thermal mixing using a porous block in a Y-shaped micromixer. The aspect ratio, porosity and thermal conductivity of the block was varied to study the thermal mixing and cooling performance of the microfluidic system.

The final active method is magnetic mixing, which uses magnetic fields and high magnetic gradients to impart magnetic forces on magnetic fluids, inducing chaotic mixing. The source of the magnetic field are usually permanent magnets or electromagnets. For example, a combination of nickel-iron and permanent magnets is designed to strategically move superparamagnetic beads in a flow field of two or more liquids as a means of mixing proposed by Ballard et al. [31]. Nouri et al. [32] proposed a simple positioning of a permanent magnet close to a Y-shaped microchannel to deviate the flow of magnetic fluid into the flow of nonmagnetic fluid. Maleki et al. [33] numerically explored the magnetic mixing phenomenon that happens inside of microdroplets which is beneficial for non-contaminated micromixed fluids. Owen et al. [34] fabricated a microfluidic device with orbiting magnetic microbead array that was activated using an external rotating magnetic field. The magnetic field polarity changed with respect to the rotation, hence moving the microbeads and causing micro streams that mixed two fluids with different properties. Hejazian et al. [35] used three permanent magnets to generate nonuniform magnetic field to mix magnetic and nonmagnetic fluids.

Unlike other active methods, magnetic field imposes great mixing performance at a low cost and footprint. However, the current methods use permanent magnets and electromagnets. Permanent magnets are bulky and leave a big footprint while electromagnets generate heat that may not be suitable for many biological applications. Furthermore, the fabrication cost for most of the active methods are higher compared to the cost to fabricate passive micromixers.

In the present work, a simple and high throughput micromixer is proposed for complete and rapid mixing of ferrofluid and distilled water. Two different designs were developed, where one design contains a single layer of microfluidic system bonded to a glass slide. The second design consists of a two-plane microfluidic system without a glass slide. These systems do not use permanent magnet or electromagnet but uses embedded microscale permanent magnet made from a mixture of neodymium powder and PDMS. The novelty of the proposed method is most magnetic micromixers are associated with permanent magnets, which are bulky or electromagnets that

generate heat, which is harmful for biological reagents. The advantage of the proposed method is the micromagnet generates high-throughput and homogeneous mixing of ferrofluid and distilled water. Furthermore, the proposed micromagnet has a small footprint and does not generate heat while generating a strong magnetic field gradient.

1.4 Separation of Microparticles in Microfluidics

Another application of microfluidics is separation of particles and cells. The most common application of separation in microfluidics is separating circulating tumor cells (CTCs) and rare cells from whole blood in a short amount of time. Similar to mixing in microfluidics, separation of cells and particles are also divided into two sections, active and passive. Examples of passive methods include field-flow fractionation (FFF), deterministic lateral displacement (DLD), herringbones, grooves, and chevrons. Fuentes et al. [36] employed an FFF called full-feed depletion mode of split flow (FFD-SF) to separate different types of starch granules into different sizes in a six-layer microfluidic system. The separated starch granules were observed under a differential scanning calorimeter to ensure the properties of the fractionated granules. Yang et al. [37] utilized FFF to sort and separate urinary exosomes in patients suffering from prostate cancer and underwent a lipidomic analysis on the recovered exosomes. Kabacaoglu et al. [38] investigated same-size but variable deformability red blood cells separation using DLD and found that deformability-based separation is possible, where cells with a large angle of deformation displace laterally in the DLD while other cells travelled with the flow direction.

Active methods are similar to those of mixing, which include magnetophoresis, electrophoresis and acoustophoresis. Magnetophoresis uses magnetic field to separate particles, and can be categorized into two parts, positive and negative magnetophoresis. Positive magnetophoresis involves separating magnetic particles from nonmagnetic particles/fluid such as the device designed by Kye et al. [39], where a magnetic particles of different diameters were separated using a dual-magnet device. Negative magnetophoresis separates nonmagnetic particles suspended in a magnetic fluid. For example, Zhou et al. [40] applied a uniform magnetic field perpendicular to the flow field to separate ellipsoidal and spherical cells. Next, electrophoresis is the motion of particles that is induced by an electric field. Ge et al. [41] developed disposable paper-based microfluidic channels actuated by a wireless electro chemiluminescence, which detects and separates electro-active and inactive amino acids. Acoustophoresis is using acoustic

field to cause motion in particles for particle separation. This method also separates exosomes from whole blood with a contactless and label-free method, done by Wu et al. [42]. This system as a high purity because of a two-stage separation system, where the first stage is separates large blood components such as red blood cells and the second stage segregates exosomes from extracellular vesicle fluid. Figure 1 summarizes the introduction of this thesis.

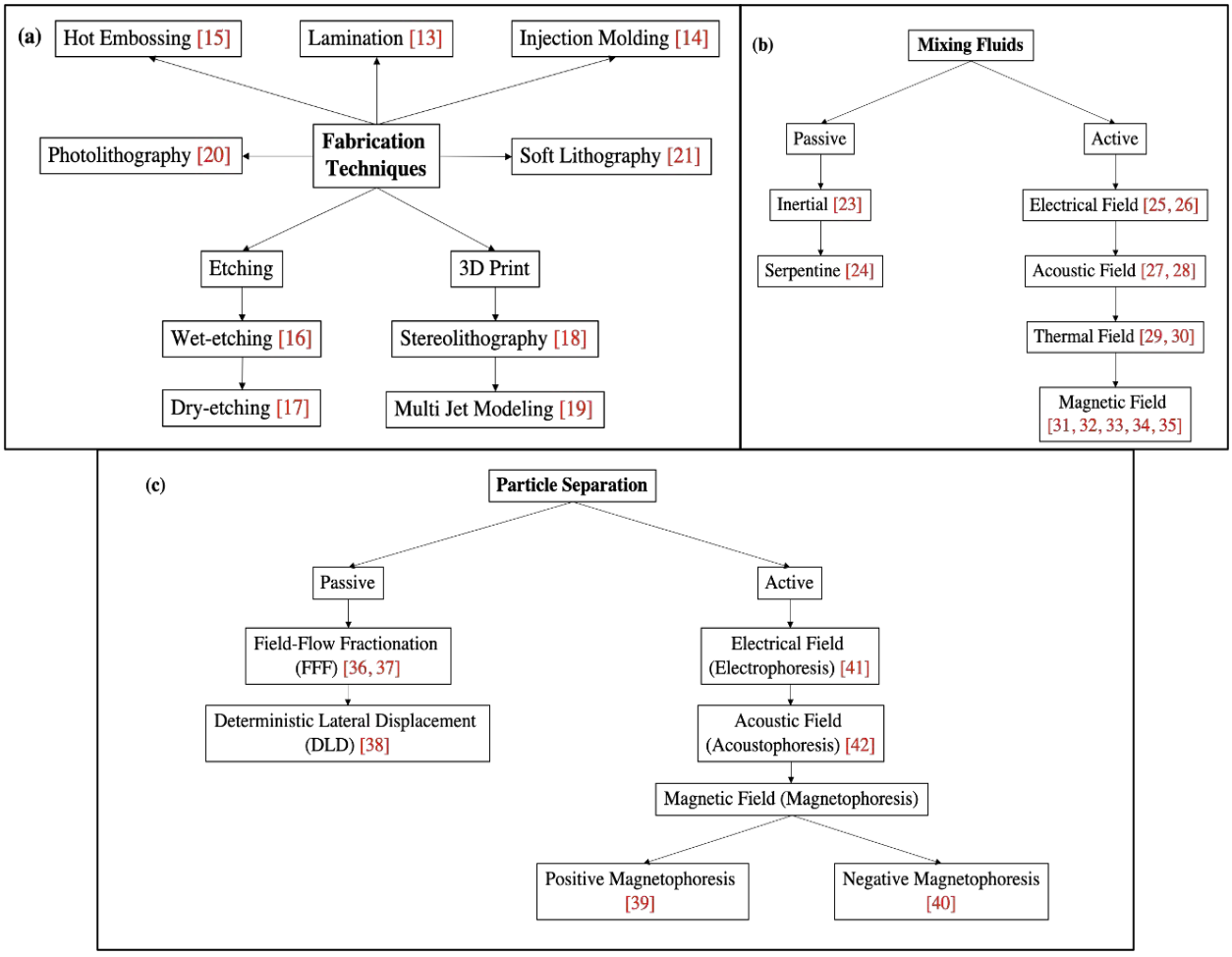

Figure 1. Summary of (a) fabrication methods of microfluidic devices, (b) classification of mixing at microscale and (c) types microparticle separation methods discussed in the body of the introduction.

The current method of separation proposes a highly efficient and low-cost method to separate magnetic and nonmagnetic particles suspended in distilled water using a microscale magnet. A uniform magnetic field imparted from the microscale magnet deviates the magnetic particles from their laminar flow path, ultimately separating them from the nonmagnetic particles. This separation

system is located on the same plane and the microscale magnet is placed perpendicular beside the microchannel, with the magnetic field going perpendicular to the flow field. Similar to the mixing system, a low-cost in-house method was used to fabricate the microfluidic chip for separation to reduce the cost of fabrication. The separation method proposed in this work combines neodymium powder and PDMS to create a micromagnet that does not generate heat while having a small footprint, high throughput and low cost. The advantage of the proposed micromagnet is the precision of micromagnets, where the shape of the micromagnet is designed in-house. Therefore, a strong magnetic field gradient is present at the desired locations and controlled separation is achieved.

1.5 Objective

The objectives and body of this thesis will entail the following topics:

1. Design and development of a stable microfluidic fabrication system
    a. Design and development of ultraviolet-light emitting diode (UV-LED) exposure platform
    b. Fabrication of copper master mold as a base for microfluidic device
    c. Fabrication of one-layer and two-layer Polydimethylsiloxane (PDMS) microfluidic devices
2. Performance study of microfluidic devices fabrication system
    a. SEM analysis for copper master molds
    b. Quality and resolution analysis of the microfluidic devices with different channels and designs
    c. UV-LED light source intensity and uniformity analysis
3. Experimental study of microfluidic mixing and separation
    a. Mixing of ferrofluid and distilled water on a single plane device
    b. Mixing of ferrofluid and distilled water on a two-plane device
    c. Separation of magnetic and nonmagnetic particles

2. DESIGN AND DEVELOPMENT OF A LOW-COST FABRICATION SYSTEM FOR MICROFLUIDIC DEVICES

2.1 Overview

The fabrication platform developed in this work is based on soft lithography. This method is low-cost and easy to fabricate compared to other microfluidic system fabrication methods, since most equipment are common equipment and little training is necessary to fabricate the devices. This method is separated into two parts, which are fabrication of master mold with pre-designed microstructures and fabrication of device using a clear silicon polymer PDMS. To create a master mold, a mold sandwich is created by lamination, UV-LED light exposure and development of photoresist film on copper plate. After creating the master mold, the device fabrication can either be one layer or two layers. For one-layer fabrication, a clear polymer is casted onto the copper plate, cured, peeled and finally bonded to a glass slide to create a microfluidic device. For two-layer fabrication, clear polymer is casted onto two separate copper plates, cured, peeled and bonded onto each other. In this section, the design and fabrication methods will be discussed. The current fabrication system demonstrates several advantages over cleanroom methods, which include low cost of manufacture and maintenance, the ability to fabricate in room temperature and pressure, minimal training for personnel and short fabrication time.

2.2 Design and Fabrication of Copper Master Mold for PDMS Microfluidic Device

The first step for the developed low-cost fabrication method is choosing a smooth surface as the base for designs of microchannels and microstructures. Having a smooth surface ensures a high-quality microfluidic device to be fabricated. If there are imperfections on the copper plate, it will be seen on the microfluidic device and the applications of the device will be hindered. In this project, copper plates were chosen as the base for the master mold. Copper plate (Copper Sheet 101 H02, Online Metals, Seattle, WA, USA) was chosen because it is the best base for the photoresist in this fabrication method according to the manufacturer. The dimension of the copper plate are 3 inches long and 2 inches wide because that surface area covers the microfluidic system sufficiently. The thickness of the copper plate is 2mm, which is suitable for the thermal laminator (brand, model). A thinner or thicker plate will not provide sufficient bonding between the copper

plate and the photoresist film. The copper plate is placed between a thick laminator sheet (0.007" thick 12" x 12" Clear Plastic Film, Grafix, Maple Heights, OH, USA) and a dry negative photoresist film (MM540, 35 μm thick, DuPont, Wilmington, DE, USA). The dimension of the lamination sheet is 5 inches long and 4 inches wide, and the dimension of the photoresist film is 4 inches long and 3 inches wide. The dimensions are chosen to allow sufficient grabbing space while running the three materials through the laminator. The chosen photoresist film is a negative photoresist film, which means that when it is exposed to light source, the photoresist film is bonded to a surface, which is the copper plate. A negative photoresist film is more desirable for this case because of the lower cost of manufacture ($\$12/m^2$).

Figure 2 shows the dimensions and arrangement of the lamination sheet, copper plate and the dry photoresist film, which results in a mold sandwich. The thickness of the photoresist film is 35μm, which is suitable for microfluidic applications. The photoresist film consists of two protective layers to protect from dust and light, since the film is adhesive. The photoresist film is protected by a top and bottom layer, where the top layer is made of polyethylene terephthalate (PET) and the bottom layer is made of polyethylene (PE) [43]. The PE layer of the photoresist is removed while passing the sandwich through the laminator, to ensure air bubbles and wrinkles do not appear between the film and copper plate (Figure 3(a)). The mold sandwich is passed through a heating laminator with a temperature of 100°C because at that temperature, the adhesive in the photoresist film gets melted onto the copper plate and a bonding between the two is established. The copper plate and photoresist film were cut away precisely away from the laminator sheet using an Exacto knife and let rest for 15 minutes. The resting period is important to let the copper plate and the photoresist film to cool down to room temperature together, which fortifies the bond between the copper plate and the photoresist film.

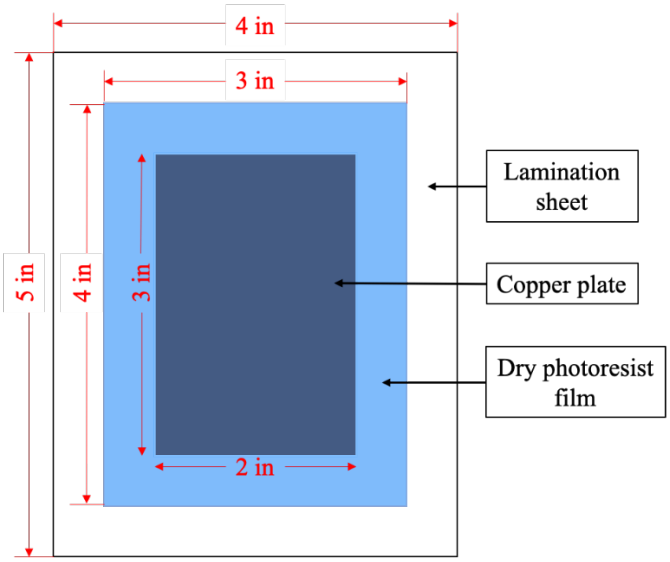

Figure 2. Dimensions of lamination sheet, copper plate and dry photoresist film and the arrangement of the three materials to form a mold sandwich.

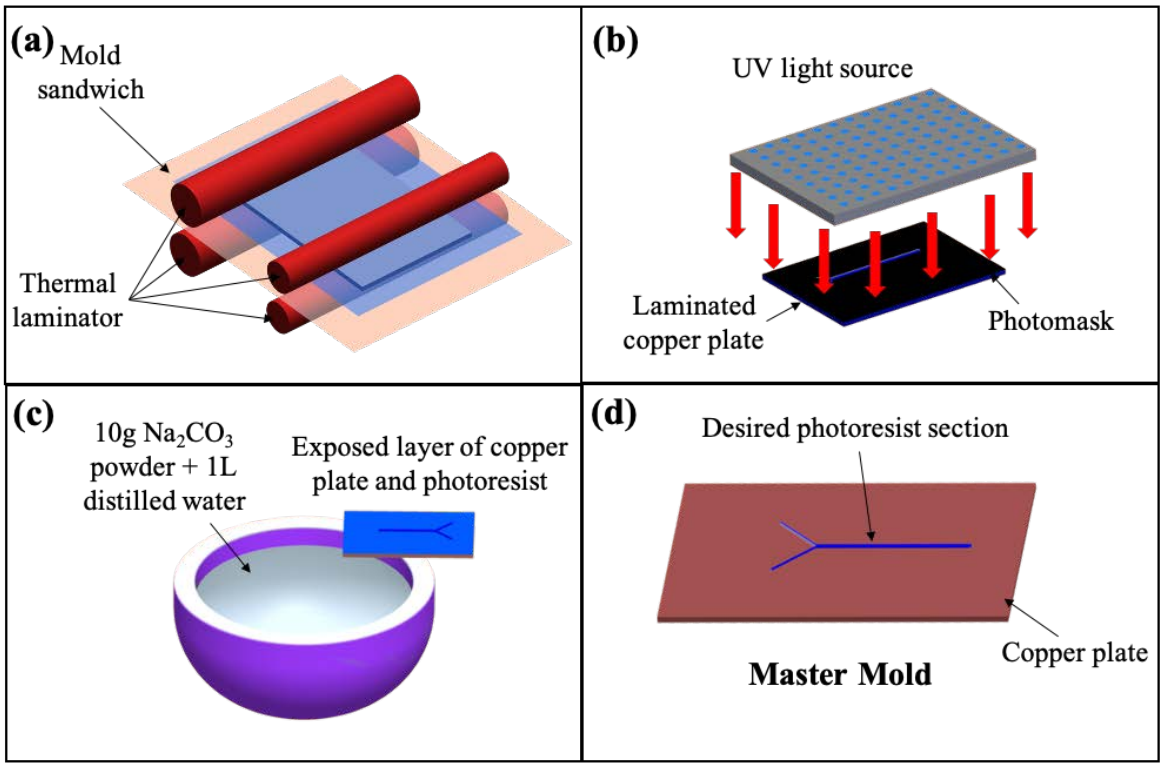

Figure 3. (a) A mold sandwich containing a lamination sheet, a copper plate and a dry photoresist film is passed through a thermal laminator that is heated to 100°C. (b) The laminated copper plate is illuminated by a UV light source for 25 seconds to polymerize sections of the photoresist film. (c) 10g of sodium carbonate (Na_2CO_3) and 1L of distilled water are mixed to create a solvent for the photoresist. The exposed copper plate is developed in the solution until only the desired sections of the photoresist remains. (d) The master mold after development and cleaning.

The microchannel was designed using AutoCAD and sent to a photomask manufacturer to be printed onto a negative photomask. Figure 4 shows an example of negative photomasks (10,000 dpi, CAD/Art Services, Bandon, OR, USA). Next, the PET layer was peeled away from the photoresist film. The photomask was placed on top of the film. A large transparent glass was placed on top of the photomask to ensure there was no gap between the photomask and the photoresist, since having a gap will alter the eventual dimensions of the microchannel. The setup was illuminated for 25 seconds to achieve proper exposure time (Figure 3(b)). Details about the light source will be discussed in section 2.4. The illuminated mold is let rest for at least two hours for maximum curing of the exposed part of the photoresist.

Next, 10g of sodium carbonate (Na_2CO_3) and 1L of distilled water were mixed at 30°C. According to the data sheet for DuPont MM500 from the manufacturer [44], the photoresist film can be developed in sodium or potassium carbonate. Sodium carbonate was chosen because of the lower cost and wider availability. To create a development solution of sodium carbonate and water, a weight percentage of 1.0% of solute is recommended by the manufacturer. DuPont also recommended a temperature of 27-35°C for the temperature of the developing solution. Using this information, 10g of Na_2CO_3 and 1L of distilled water were heated to a temperature of 30°C. The rested copper plate was developed in the sodium carbonate solution (Figure 3(c)). The development is done by submerging the copper plate inside the solution and agitating the solution onto the copper plate until only the microchannel remains on the copper plate. The plate is immediately submerged into distilled water to halt further development. Then, the developed copper plate is cleaned using isopropyl alcohol (IPA), distilled water and compressed air. The resulting master mold is shown in Figure 3(d).

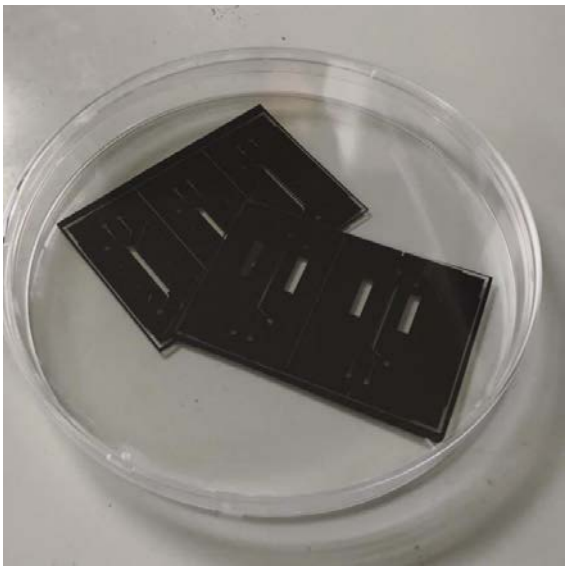

Figure 4. Two negative photomasks contained in a petri dish to avoid accumulation of dust.

2.3 Fabrication of Microfluidic Device

After the master mold is ready, the soft polymer microfluidic device can be fabricated. Polydimethylsiloxane (PDMS) (Sylgard 184, Dow Chemical, Midland, MI, USA) is the chosen soft polymer because it can withstand high heat, is transparent, and biocompatible, which shows that it is non-toxic. In a plastic cup, 25g of PDMS base and 2.5g of PDMS activator were mixed thoroughly until a lot of bubbles form (Figure 5(a)). According the technical data sheet provided by the manufacturer, the specific gravity of the PDMS and activator is 1.03. The desired volume of microfluidic device is 27.1cm^3, where the device size is 2in x 3in x 0.28in (5.08cm x 7.62cm x 0.7cm). The specific gravity is the ratio between the density of the material and the density of water. After some simple calculation, the mass of PDMS is found to be 27.91g, which explains the reason for choosing the amount of PDMS base and activator of 25g and 2.5g. A device thickness of 0.7cm is desired because it is not thin enough to release bonding between PDMS and glass slide and it is not thick enough where the pressure of the PDMS blocks the microchannel by sticking to the glass slide. By adding the base and the activator, the PDMS is activated, which will cure it in a certain period of time depending on the temperature. The mixture was degassed in a vacuum chamber until all the bubbles dissipated.

While the mixture is degassing, an aluminum foil box is prepared to hold and cure the PDMS. The aluminum foil box was made with heavy duty aluminum foil to prevent tearing and leakage, with the box's dimensions being 3 inches long and 2 inches wide. An aluminum foil box is made

because it will be torn away from the copper plate and PDMS after curing. It also helps to keep the cost of fabrication low. The master mold is placed inside the aluminum box, with the structures facing upwards. After all the bubbles have dissipated from the PDMS mixture, it is poured onto the master mold slowly, avoiding bubble creation (Figure 5(b)). Some bubbles will still form due to the interaction between the liquid PDMS and the copper plate that causes rotation and microvortex. After a couple of minutes, the bubbles are diminished by atmospheric pressure. Bigger bubbles that do not disappear are removed using a needle.

The box is placed inside a preheated oven at 60°C for 2 hours (Figure 5(c)) according to manufacturer's directions [45]. Alternatively, the box can be placed in a dark area for 24 hours, but this method allows the risk of leakage of the PDMS out of the box, since the PDMS is at a liquid state for a longer period of time. After the PDMS is cured, the aluminum box is removed and the PDMS layer is peeled away from the master mold. The master mold is kept away in a dark area for future use. The PDMS layer is cut using a precision cutter to prevent rough edges. Rough edges will hinder a tight bond between PDMS and glass slide or other surfaces. The PDMS layer is also injected using a hole cutter to create inlet and outlet holes. Figure 5(d) shows the PDMS layer with a groove in the shape of a microchannel.

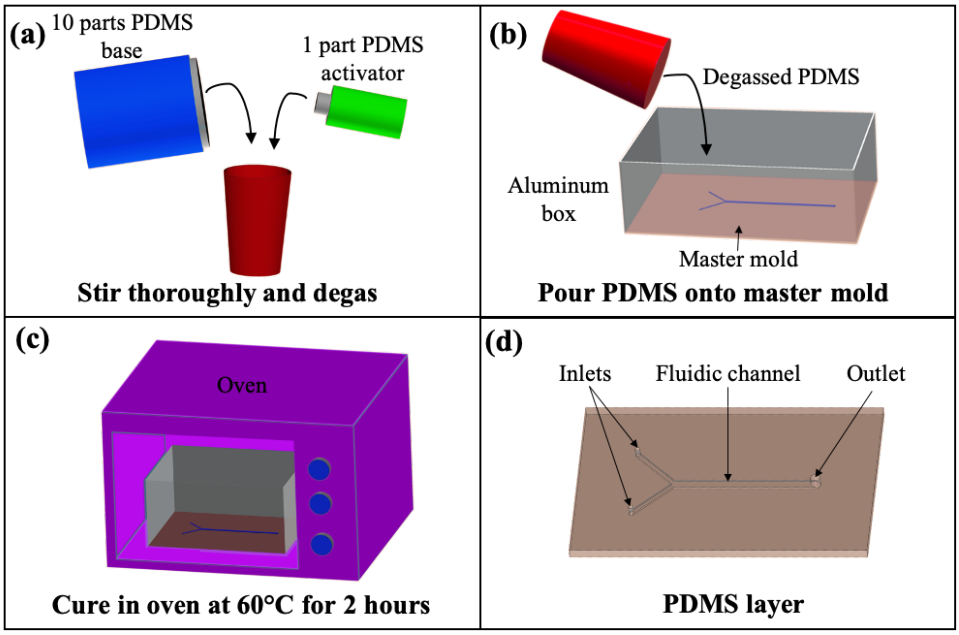

Figure 5. (a) 10 parts of PDMS base and 1 part of PDMS activator are poured into a plastic cup and degassed in a vacuum chamber. (b) A box is built using aluminum foil and the master mold is placed in it. Degassed PDMS is poured onto the master mold and any bubble formation is avoided. (c) The PDMS is cured in the oven at 60°C for 2 hours. (d) The aluminum foil is peeled away from the cured PDMS layer, which was then detached from the master mold. Inlets and outlet holes were injected and the PDMS layer is cut to a dimension of 2 inches by 3 inches.

2.3.1 Fabrication of Single Layer Device

The PDMS layer contains three different microchannels and microstructure systems (Figure 6). Hence, the PDMS layer is cut to three parts, where each part corresponds to a specific system. Using this method, a lot of time and resources are reserved because three devices were fabricated in one cycle. A glass slide with dimensions of 2 inches long and 1 inch wide and the bottom of the PDMS layer are both cleaned using IPA, distilled water and scotch tape. After removing the scotch tape, the glass slide and PDMS were placed inside a vented hood, with the clean side facing up. The vented hood was turned on to remove any particles and dust from the area, keeping it clean. The glass slide and the PDMS layer were treated with corona surface treatment ((N001-020, UV Process Supply, Inc, Chicago, IL, USA) for 60 seconds each side (Figure 7(a)). The corona surface treatment modifies the surface of the treated object using plasma that is discharged from high-voltage electrode. This treatment ensures sufficient bonding between the PDMS layer and the glass slide. The PDMS layer is pressed onto the glass slide, making sure no bubbles were formed. The bonded PDMS was placed on a hot plate at 120°C for

at least 12 hours for complete bonding. A strong bonding allows the device to withstand the pressure exerted from the fluid pumped into the channels.

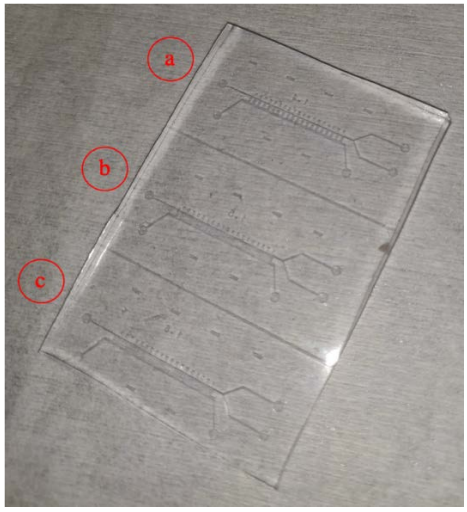

Figure 6. Prototype of PDMS layer containing 3 different microfluidic device designs. (a) Microfluidic design with rectangular protrusions magnetic structures. (b) Microfluidic design with rectangular bar magnetic structures. (c) Microfluidic design with rectangular bar magnetic structures with different spacing between magnetic bar and microchannel.

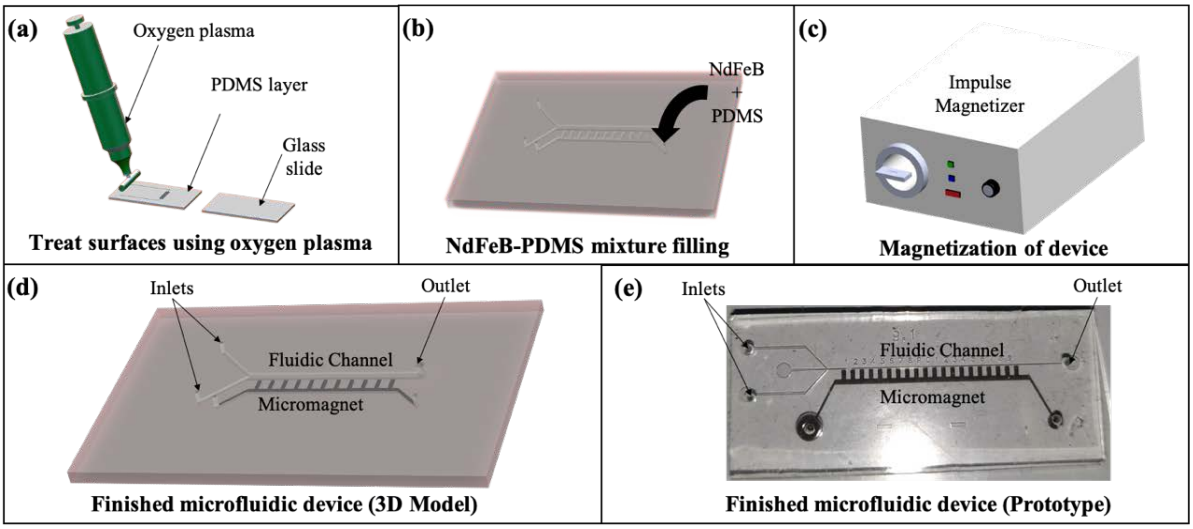

Figure 7. (a) Oxygen plasma treatment on both the PDMS layer and glass slide before bonding and placing on a hot plate at 120°C for 12 hours. (b) A mixture of PDMS and NdFeB powder is injected into the microstructure and cured on the hot plate for 15 minutes at 120°C and 2 hours at 60°C. (c) The cured microfluidic device with magnetic structure is magnetized in an impulse magnetizer to activate the magnet. (d) 3D model of the finished microfluidic device containing 2 inlets and 1 outlet. (e) Finished prototype of magnetized microfluidic device.

After 12 hours, a mixture of neodymium (NdFeB) powder (MQFP-B-20076, Molycorp Magnequench, Singapore) and PDMS is made in a plastic cup. 10g of PDMS base, 1g of PDMS activator and 11g of NdFeB powder is mixed thoroughly in a plastic cup inside the vented hood to remove any loose NdFeB powders. NdFeb powder is the base for the microscale magnet in this system. The mixture is degassed in a vacuum chamber to remove bubbles. Meanwhile, a 1mL syringe is prepared by connecting a slip luer to the syringe, a flexible tube with an inner diameter of 0.031 inch to the luer, and a smaller tube with an outer diameter of 0.03 inch to the bigger tube. This setup is designed so that no leakage happens while injecting the NdFeb-PDMS mixture into the microstructure. The diameter of the luer is too large compared to the size of the inlets in the microfluidic device, hence the bigger tube acts as a bridge to connect the smaller tube and the luer.

Once the NdFeB-PDMS mixture is completely degassed, it is filled into the 1mL syringe. The syringe is tapped on a hard surface while being vertical to remove any air bubbles trapped inside. The luer-tube-tube setup is connected to the syringe and it is filled to ¾ of the length of the tubes. The syringe is placed on a syringe pump (Cole Parmer/KD Scientific 74900, Holliston, MA, USA) and the syringe pump is turned on with a flow rate of 1mL/hr. Once the tubes are filled completely with the NdFeB-PDMS mixture, the flow rate is decreased to 0.5mL/hr. The flow rate is decreased so that it is suitable for the bonding of the microstructure. The syringe is connected to the microstructure after the flow rate is decreased (Figure 7(b)). After the microstructure has been filled completely with the NdFeB-PDMS mixture, the system is placed on a hot plate at 120°C for 15 minutes, then decreased to 60°C for 2 hours. The device is placed in a high temperature for the first 15 minutes after the microstructure has been filled to fast cure the mixture. By doing this, the NdFeB particles in the mixture does not sediment and clump in the microstructure because of the high viscosity of the mixture.

After the mixture is cured, it is magnetized in an impulse magnetizer (IM 10, ASC Scientific, Narragansett, RI, USA) at a charge of 250V (Figure 7(c)). At this point, the single layer microfluidic device is ready with a functioning microscale magnet that does not require the assistance of an external magnetic source to generate a magnetic field. The rectangular structures of the microscale magnet are chosen because it creates a high magnetic field gradient at the corners of the rectangles. This will be discussed further in Section 3.3. The final image of the microfluidic device model and prototype are shown in Figure 7(d) and Figure 7(e) respectively.

2.3.2 Fabrication of Two-Layer Device

The PDMS layer contains a Y-shaped microchannel with a length of 2 cm. This PDMS layer will be called the fluidic layer from this point onwards (Figure 8(a)). The fluidic layer will be kept aside for now. The steps in sections 2.2 and 2.3 are repeated to create a master mold and a PDMS layer for the microstructure, respectively. Figure 8(b) shows the microstructure layer which will then be bonded to a fluidic layer creating the two layers of PDMS for the microfluidic device.

After holes were created on the microstructure layer, the bottom of the layer was cleaned using IPA, distilled water and scotch tape. A 2 in x 3 in glass slide was cleaned using the same method. The clean sides of the glass slide and the microstructure layer were placed inside the vented hood with then clean sides facing up. The lower 1/3 of the glass slide and the corresponding area of the microstructure layer were treated with oxygen plasma and bonded together (Figure 8(c)). The bonded layer is placed on a hot plate for 12 hours at 120°C. A weight is placed on the PDMS-glass slide during this time to ensure a strong partial bonding between the upper non-treated portion of the glass slide and PDMS layer.

After 12 hours, similar to the fabrication of the single layer microfluidic device, a mixture of neodymium (NdFeB) powder and PDMS is created in a plastic cup. 5g of PDMS base, 0.5g of PDMS activator and 5.5g of NdFeB powder is mixed thoroughly in a plastic cup inside the vented hood to remove any loose NdFeB powders (Figure 8(d)). The ratio between PDMS and NdFeB is 1:1 for this setup, so the chosen amount of solution can be varied. In this case, a smaller amount of material was chosen because the cavity for the microstructure is much smaller compared to the single layer device. The mixture is degassed in a vacuum chamber to remove bubbles. Meanwhile, a 1mL syringe is prepared by connecting a slip luer to the syringe, a 0.031-inch diameter flexible tube to the luer and a 0.03-inch diameter flexible tube to the bigger tube, also similar to the previous device. A smaller glass slide is placed on the microstructure layer and the PDMS is secured to the glass slide by a bulldog clip. The purpose of the smaller glass slide is to distribute the pressure exerted by the bulldog clip evenly to the PDMS.

Once the NdFeB-PDMS mixture was completely degassed, it was filled into the 1mL syringe and air bubbles were removed. The luer-tube-tube setup was connected to the syringe and filled to ¾ of the length of the tubes manually. The syringe is placed on the syringe pump with a flow rate of 1mL/hr. Once the tubes are filled completely with the NdFeB-PDMS mixture, the pump is turned off. The syringe is connected to the microstructure layer. The microstructure will

fill up slowly even though the pump is turned off because of the residual pressure left from the previous flow rate of 1mL/hr in the small diameter tubes (Figure 8(e)). After the advancing of the mixture inside the microstructure slows down drastically, the pump is turned on to a flow rate of 0.03mL/hr. A low flow rate is necessary for this microstructure because it is not permanently bonded to the glass slide. If the pressure exerted by the mixture is higher than the pressure exerted by the bulldog clip towards the PDMS and the glass slide, the mixture will leak out of the microstructure. However, if the flow rate is too low (i.e. 0.01mL/hr), the mixture will cure inside the microstructure before filling it up, which is not desirable for the fabrication of the microscale magnet because agglomeration has happened.

After a considerable portion of the microstructure is filled with the mixture, the syringe tube is removed from the PDMS layer and the setup together with the alligator clip is placed in an oven that was preheated to a temperature of 110°C for 15 minutes, then the temperature of the oven is decreased to 60°C for 2 hours (Figure 8(f)). Unlike the previous device, the presence of the bulldog clip for this device prevents the usage of a hot plate for fast curing. The bulldog clip temporarily secures the microstructure layer to the glass slide and contains the NdFeB-PDMS mixture inside the microstructure while preventing leakage. However, the mixture cannot be heated on the hot plate because the bulldog clip creates a gap between the hot plate and the PDMS, which prevents heating. The setup is left at room temperature overnight after heating to make sure that the NdFeB-PDMS mixture is completely cured. Then, the alligator clip and small glass slide were removed, and the microstructure is magnetized in the impulse magnetizer. The microstructure layer is then peeled and cut away from the glass slide as far as it can go.

The fluidic layer is brought back to the workstation. The magnetic array in the microstructure layer and the microchannel are aligned using a protractor to make sure that the angle is 90°. Since the microstructure layer is smaller than the fluidic layer, it is crucial to make sure that the microstructure layer is at least 2cm in length. This ensures that the microstructure layer covers the surface area of the fluidic channel in the fluidic layer. The bottom of the microstructure layer and microchannel layer were cleaned using IPA, distilled water, and scotch tape. They were treated using oxygen plasma and bonded, making sure to avoid any air bubbles (Figure 8(g)). The bonded layers were placed on a hot plate at 120°C overnight for complete bonding (Figure 8(h)). A paperweight is placed on top of the device to make sure that the layers

do not separate, and the heat reaches the position of bonding. After bonding, the two-layer microfluidic channel is ready for experimentation (Figure 8(i)).

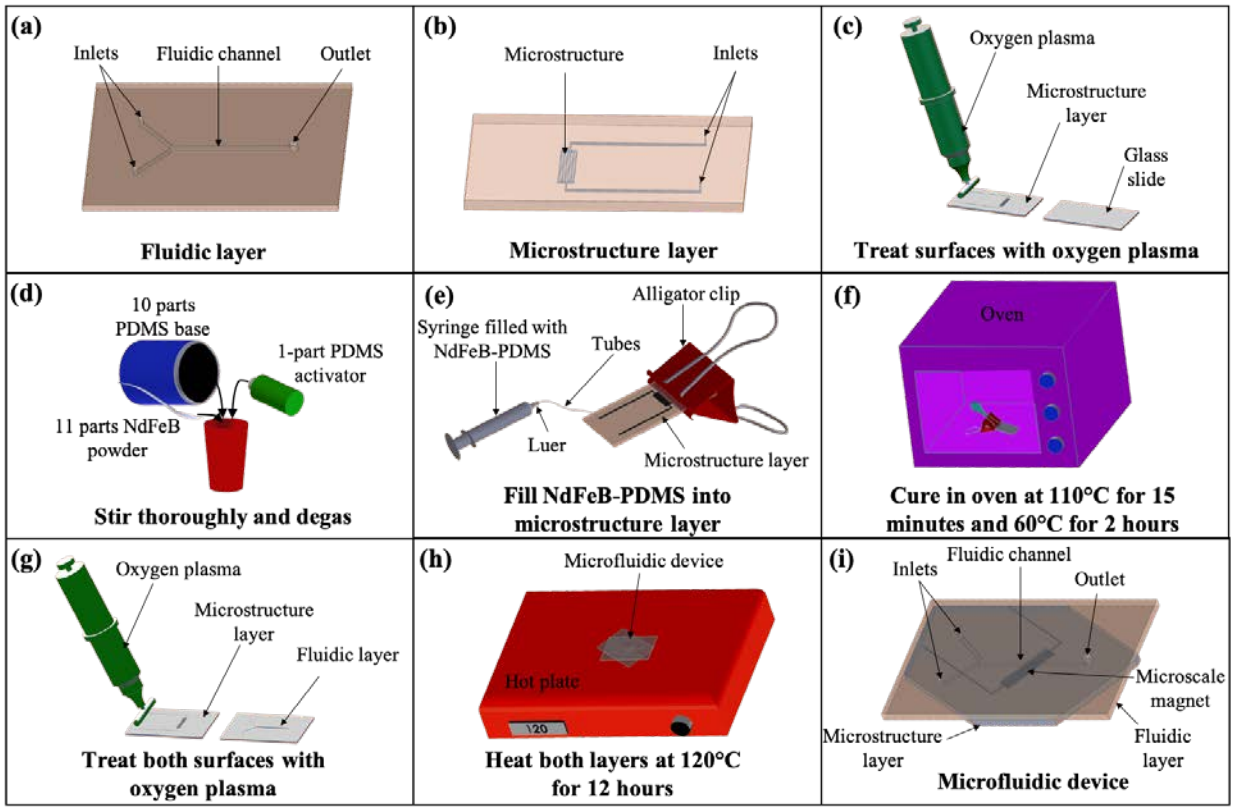

Figure 8. (a) Fluidic layer that contains a microchannel with two inlets and one outlet. (b) Microstructure layer that contains the shape of the magnetic array. (c) The lower one-third of the microstructure layer and the glass slide is treated using oxygen plasma and the two layers are temporarily bonded. (d) 1 part of PDMS and 1 part of NdFeB powder are mixed together and degassed until all bubbles are dissipated. (e) The NdFeB-PDMS is filled into a syringe and injected into the partially bonded microstructure layer which is secured by a bulldog clip. (f) The filled microstructure layer is fast cured for 15 minutes at 110°C and completely cured at 60°C for 2 hours. (g) After the microstructure is peeled from the glass slide, the bottom of the microstructure and microchannel layers are cleaned. Both surfaces are treated with oxygen plasma and bonded together. (h) The bonded microfluidic device is heated on a hot plat at 120°C for 12 hours. (i) Microfluidic device contains microstructure layer on the bottom and fluidic channel on the top.

Table 1 shows the budget form that contains some materials for the fabrication of the one-layer and the two-layer microfluidic devices. Water based ferrofluid is a mixing fluid to create a micromixer from this device. The copper plates are the substrates for the master mold. PDMS is the elastomer for the fabrication of all the devices. The channels and structures are designed in

AutoCAD and printed precisely on a negative photo mask, which is then placed on the photomask to be exposed to UV light. Photoresist film is laminated onto the copper plate and illuminated so the channels can be developed. Neodymium powder generates strong magnetic field by the micro scale magnet.

Table 1. Cost for primary materials used in the fabrication of microfluidic device.

Item	Unit price
Water-based ferrofluid ENG 408, Ferrotec, Santa Clara, CA, USA	$7.15
3in x 2in Copper plate Copper Sheet 101 H02, Online Metals, Seattle, WA, USA.	$3.42
PDMS SYLGARD™ 184, Dow Chemical Company, Midland, MI, USA	$110.00
Photo Mask 10,000 dpi, CAD/Art Services, Bandon, OR, USA	$97.00
Photoresist Film MM540, 35µm thick, DuPont, Wilmington, DE, USA	$74.00
Neodymium powder Molycorp Magnequench, Singapore	$125.00

2.4 Design and Development of a UV light source

As discussed in Section 2.2, a crucial step in this fabrication technique is creating a master mold. The master mold is created by illuminating a dry photoresist film to specific microchannel and microstructure shapes. The chosen dry photoresist film is a negative photoresist, which means that when it is exposed to light, the photoresist forms a bond with the copper plate. The illumination is conducted using a UV light source with a specific intensity. In this section, the construction of the UV light source configuration for the illumination step of this fabrication method will be discussed.

2.4.1 UV Light Source Concept in Soft Lithography

DuPont MM540 dry negative photoresist film was chosen because of its low cost ($12/m^2) and compatibility with microfluidics. When the dry negative photoresist is illuminated with UV light, the polymer that constitutes the photoresist becomes exposed and undergoes UV irradiation cross link [46]. When this phenomenon happens, the photoresist forms a bond between itself and the surface that it is attached to. UV light passes through the photomask and forms UV crosslinking

on the negative photoresist. Figure 9 shows the working principles of a negative photoresist in this fabrication method. First, a photomask is placed on a substrate, in this case a copper plate that is laminated with a photoresist film. The photmask is a dark film that has clear designs for the microfluidic channels and microstructures. When illuminated by a UV light source, only the desired section allows light to pass through. Next, the illuminated portion of the photoresist film is crosslinked to form a stronger bond, hence appearing darker than the rest of the photoresist. Finally, the illuminated copper plate with photoresist is developed, which removes the covered photoresist and creates a master mold.

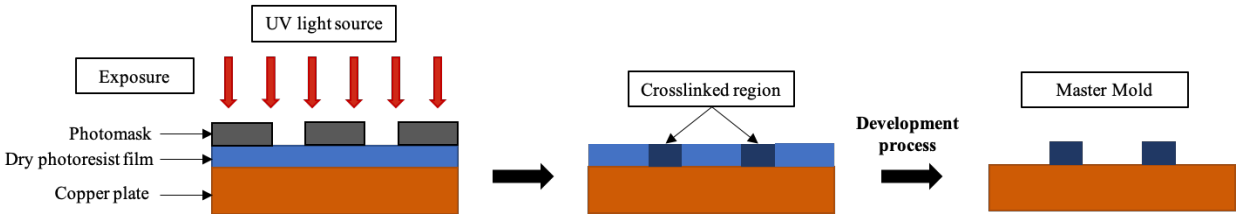

Figure 9. Working principles of negative photoresist film in soft lithography.

A number of factors determine the strength of the crosslinked bond of the photoresist, which include the intensity of the UV light, the exposure time and also the development time. According to the data sheet provided by the manufacturer [44], the recommended UV light exposure range to ensure proper cross-linking of the photoresist film is 25-55 mJ/cm^2. The amount of time needed for cross linking varies with each experiment and application.

2.4.2 UV Light Configuration

In order to illuminate the mold sandwich to create a master mold, a light source platform was built. A sketch of the front view of the UV light setup is shown in Figure 10(a). The height between the platform and the photoresist film, h, is different for various applications. The performance of the light source at different heights will be discussed in Section 3.5. In Figure 10(b), the setup for the exposure step that contains the LED holder and the voltage source is shown. Electrical tape secures the rows of LED lights together and alligator clips connect the LED lights to the voltage source. The prototype for the LED light holder is shown in Figure 11(a), which was designed in SolidWorks and 3D printed with polylactic acid (PLA). Each LED mount holds one LED light. A

staggered pattern was designed to place the individual LED lights because it produces illumination that is the most uniform and least interference [47].

The individual LED lights are connected in series and all rows of LED lights in series are then connected in parallel with each other. After that, a parallel connection between the LED lights and a voltage source is established. Elements that are connected in parallel contain the same voltage while elements that are connected in series contains the same current. The voltage passing through an LED light determines the brightness in this case, since the power source is in constant voltage mode. Hence, a parallel connection is preferred for the entire circuit to maintain the brightness of each LED light. Figure 11(b) shows the electrical schematic of the connection between all the LEDs and the voltage source. A staggered pattern was achieved using an alternating number of LEDs in each row, which are rows of 13 and 12 LEDs. A total of 31 rows of LEDs are connected in parallel with each other.

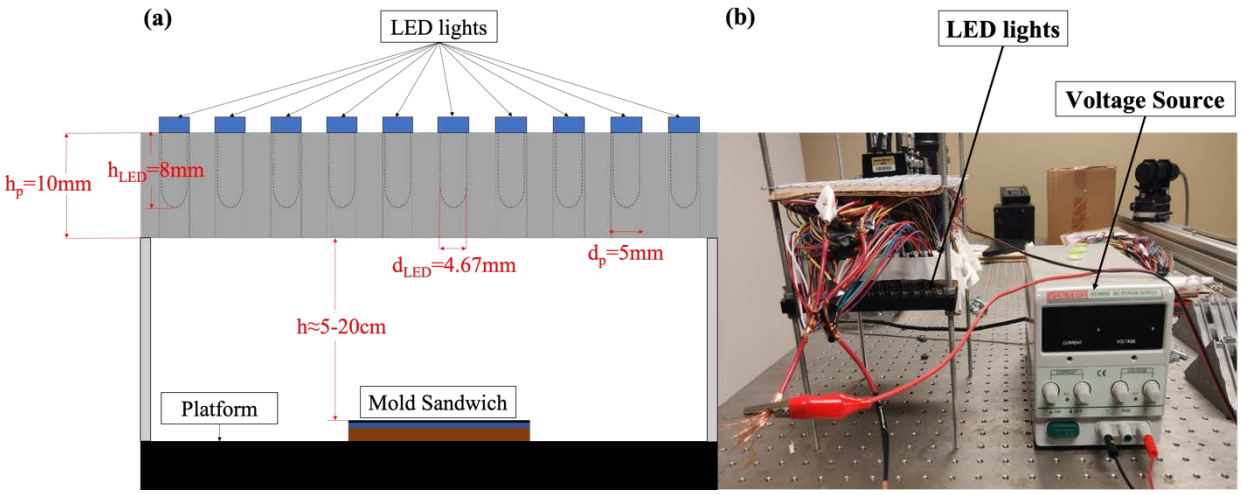

Figure 10. (a) Front view of the light exposure station. The height between mold sandwich and the LED lights, h, is varied to find the optimized height. The height of the platform, h_p, height of LED, h_{LED}, diameter of LED mount on the platform, d_p, and the diameter of the LED light, d_{LED}, are shown in the figure. (b) The light source setup for the exposure step.

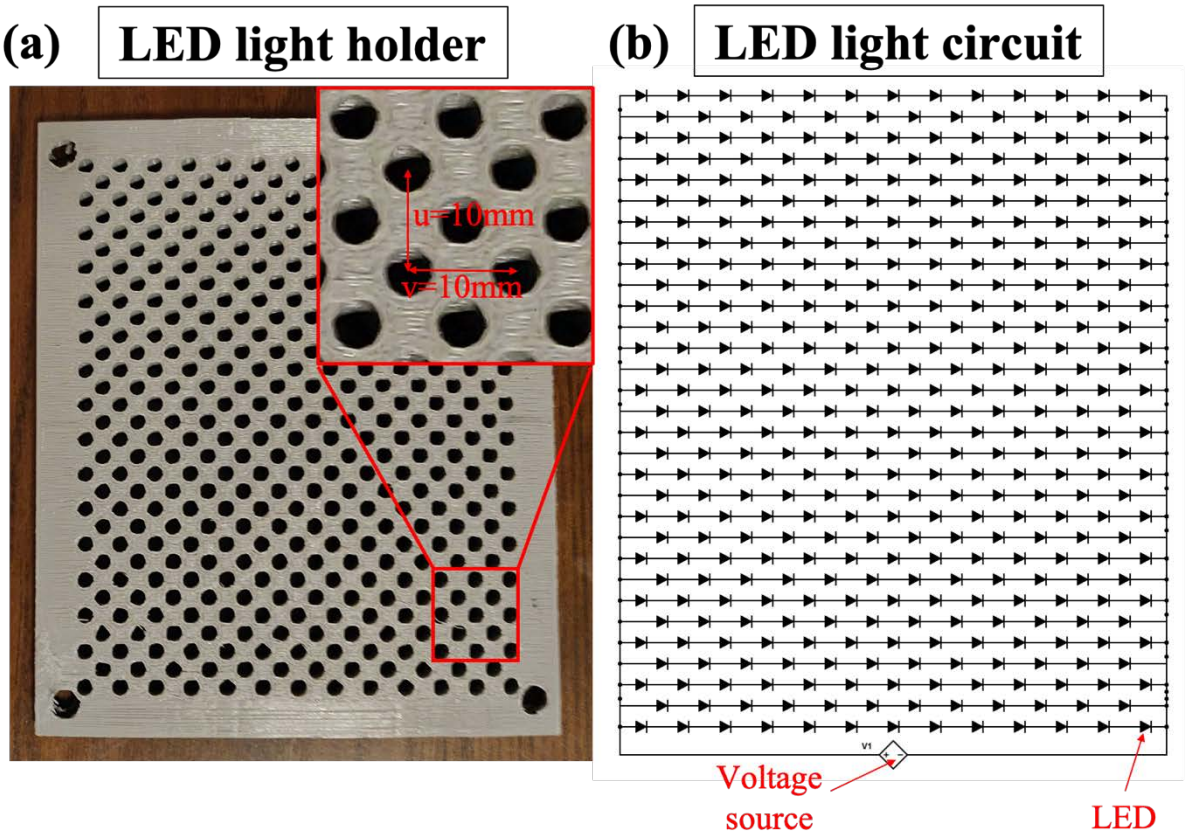

Figure 11. (a) 3D printed LED light holder. The dimensions *v* shows the horizontal distance between two columns of LED light mounts and *u* shows the vertical distance between two rows of LED light mounts. (b) LED light source configuration circuit schematic that shows each LED light that is used in the exposure step.

2.4.3 Design of UV Light Platform

For optimum use of a UV light source, a platform with adjustable height and a reasonable surface area is needed. The platform has to be as flat and horizontal as possible. Figure 12 shows the effect of the thickness of the LED light holes on the illumination rays. The thickness of the platform was designed to be 1cm, which is 2mm more than the length of the LED bulb for the walls of the platform to force the UV rays to point vertically instead of diverging outwards. This minimizes interference with the surrounding LED lights. Each LED light provides a wavelength, λ, 380nm of UV light. When interference happens between multiple LED lights, non-uniform wavelength is produced, which leads to a non-uniform thickness of the crosslinked photoresist film. This is detrimental to the performance of the master mold because a small change in thickness is significant in microscale experiments.

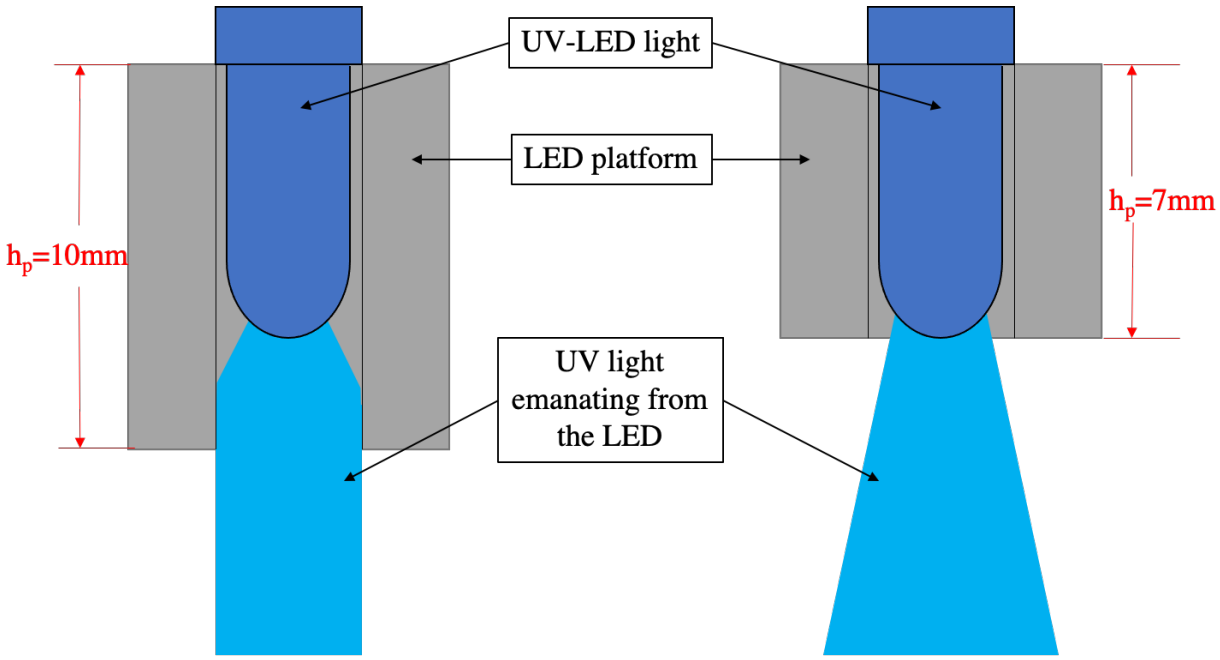

Figure 12. Effect of the thickness, t, of LED lights platform to the LED rays.

The LED lights (RL5-UV0315-380, ledhutlights.com) have a forward voltage of 3.5V. When the LED lights were connected to the power source, the power source is in constant current mode until the voltage is increased to 3.4V, which is close to the forward voltage of the LED lights. Then, the power source changes to constant voltage mode and current is increased to 0.8A to achieve the desired light intensity.

3. PERFORMANCE OF FABRICATION SYSTEM

3.1 Overview of Performance Analysis of the Fabrication System

After developing and optimizing the fabrication system, the next step is validation, which is conducted by evaluating the performance of the fabrication system. This is investigated by testing the finalized product of the fabrication system, which is the microfluidic device and determine that there are no flaws and it is suitable for microfluidic applications. In this section, the design of the microfluidic channels is shown, scanning electron microscopy (SEM) is applied to test the resolution of the master mold and the intensity and uniformity of the UV-LED light source is evaluated.

3.2 Design of Microfluidic Channels and Structures

Microscale drawings were sketched using Autodesk AutoCAD because of the high-resolution engineering drawings outputted by the software. Figure 13 shows an example of a design for the microfluidic channel and magnetic microstructure that was designed using AutoCAD before being sent to the manufacturer to print on a negative photomask. Each microfluidic device design is labelled so that the exact measurements can be retrieved easily. In order to evaluate the resolution of the master mold, a microfluidic design was drawn in AutoCAD that contains different shapes and sizes. Different shapes were investigated to evaluate the fabrication of the master mold.

Figure 14 shows the shapes and sizes of the microstructures that were studied to evaluate the resolution of the master mold. An outline measuring 2in x 3in was first drawn to set the borders of the design. As explained in the previous section, a copper plate measuring 2in x 3in is the substrate for fabrication of master mold. Hence, the borders of the photomask design are measured to be 2in x 3in to fit on the copper plate. The design was repeated eight times in one copper plate to evaluate the consistency of the fabrication at different points of the copper plate. Different lengths and arrays of rectangles, squares and circular patterns were designed, shown in Table 2. From Figure 14, row A contains the largest design of rectangles while row B contains smaller design of rectangles. Row C contains large designs of squares with a larger gap between the squares while row D contains smaller squares. Row E contains large designs of circles with a larger gap between

them while row F contains the smaller circles. In all the rows, the size decreases from the arrays on the left columns to the right columns, which is shown in Table 2. All the rectangles have a length of 3000µm, with the largest rectangle having a width of 100µm, while the smallest rectangle having a width of 10µm. The side length for the largest and smallest square structures are 120µm and 10µm, respectively. Finally, the largest and smallest diameter for the circular structures is 100µm and 10µm, respectively. All the structures have the same gap as their widths and diameters.

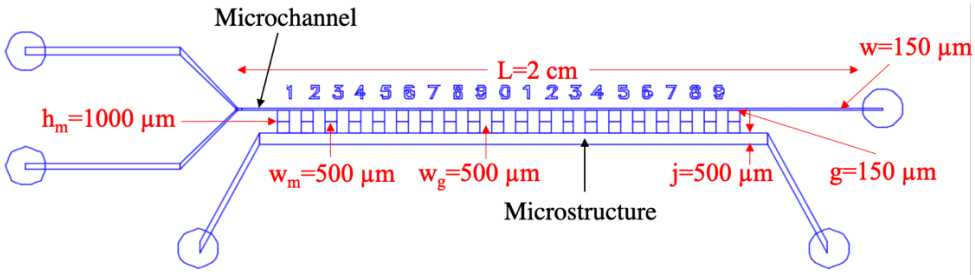

Figure 13. AutoCAD design containing microchannel and microstructures with rectangulas.

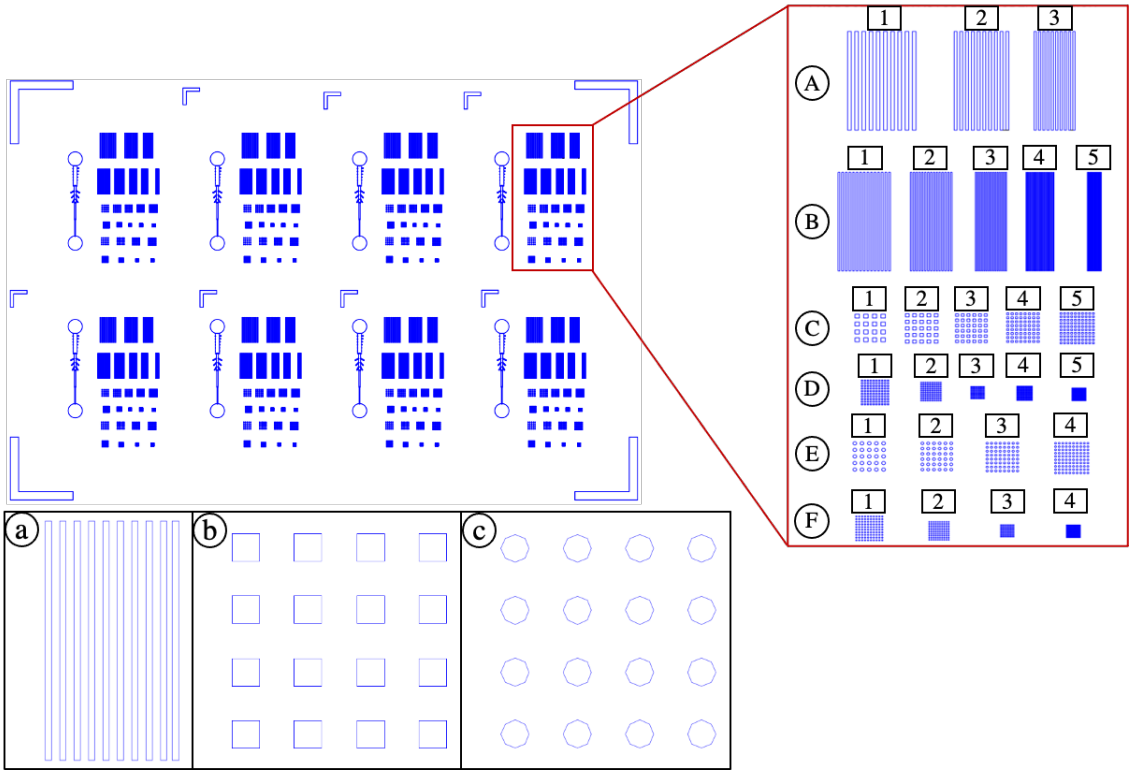

Figure 14. AutoCAD design to test the performance of microfluidic master mold. A-F shows the rows and 1-5 shows the columns of the array placement. The design contains arrays of (a) rectangular, (b) square and (c) circular shapes that are developed onto the copper plate.

Table 2. List of parameters and their respective values for the structures in Figure 14.

Row	Column	Parameter	Values (µm)	Row	Column	Parameter	Values (µm)
A	1	Length	3000	**D**	1	Side Length	40
		Width=Gap	100			Total Length	760
		Total width	1900		2	Side Length	30
	2	Length	3000			Total Length	570
		Width=Gap	80		3	Side Length	20
		Total width	1520			Total Length	380
	3	Length	3000		4	Side Length	15
		Width=Gap	60			Total Length	435
		Total width	1140		5	Side Length	10
B	1	Length	3000			Total Length	390
		Width=Gap	50	**E**	1	Diameter=Gap	100
		Total width	1450			Total Length	900
	2	Length	3000		2	Diameter=Gap	80
		Width=Gap	40			Total Length	880
		Total width	1160		3	Diameter=Gap	60
	3	Length	3000			Total Length	900
		Width=Gap	30		4	Diameter=Gap	50
		Total width	870			Total Length	950
	4	Length	3000	**F**	1	Diameter=Gap	40
		Width=Gap	20			Total Length	760
		Total width	780		2	Diameter=Gap	30
	5	Length	3000			Total Length	570
		Width=Gap	10		3	Diameter=Gap	20
		Total width	390			Total Length	380
C	1	Side Length	120		4	Diameter=Gap	10
		Total Length	840			Total Length	390
	2	Side Length	100				
		Total Length	900				
	3	Side Length	80				
		Total Length	880				
	4	Side Length	60				
		Total Length	900				
	5	Side Length	50				
		Total Length	950				

3.3 Scanning Electron Microscopy (SEM) Analysis of Fabrication Performance

A scanning Electron Microscope (JSM-6010LA, JEOL, Akishima, Tokyo, Japan) was used to precisely detect the smoothness of the microstructures on the master mold after the development process. Procedures detailed in Section 2.2 are carried out to produce a master mold. The purpose of this master mold is to control the quality and resolution of the structures developed by the preliminary fabrication process. This shows the performance of the light source and the development time. The parameters that are varied to evaluate the master mold are the light source exposure time, t_e, and development time, t_d, of photoresist in $NaCO_3$ solution. For the base case, the light exposure time and development time are 25 seconds and 60 seconds, respectively. Five different exposure times of t_e=15s, t_e=25s, t_e=35s, t_e=45s and t_e=55s with a development time of 60s and five different development times of t_d=30s, t_d=45s, t_d=60s, t_d=75s and t_d=90s and an exposure time of t_e=25s were chosen to evaluate the fabrication performance of the master mold.

3.3.1 Effect of Exposure Time under UV Light on Microstructures Resolution

In this section, the effect of different exposure times paired with a development time of t_d=60 seconds were examined for the microstructures observed under an SEM. Figure 15 shows the rectangular structures for different exposure times. Figure 15(a-e) represents exposure times of t_e=15s, t_e=25s, t_e=35s, t_e=45s and t_e=55s respectively. A scale bar of 500μm is shown in each subfigure for the size reference of the microstructures. For an exposure time of t_e=15s, the structures were underexposed. Underexposure is when t_e is less than the optimum time required to expose the photorests film for proper crosslinking to occur. At t_e=15s, only portions of the gap between the rectangles were developed, which means that the rectangles were not fully separated from each other. For an exposure time of t_e=25s, one rectangle has deviated away from the array, but the other parts were exposed properly. At an exposure time of t_e=35s, overdevelopment had occurred, where some rectangular structures have detached from the copper plate. Overdevelopment happens when the photoresist is exposed to the developing solution, which is the sodium carbonate solution, for a long period of time. The bond between the photoresist film and the copper plate is weakened until the illuminated sections of the photoresist film are detached from the copper plate. For an exposure time of t_e=45s, overexposure has occurred. Overexposure happens when the UV-LED light rays are illuminated onto the photoresist film for a period longer

than the optimum amount of time, causing light rays to seep through to the areas where the light was not supposed to be exposed. Hence, the resulting copper master mold does not have sharp corners. For an exposure time of t_e=55s, the structures are not developed properly because of overexposure of the UV light source.

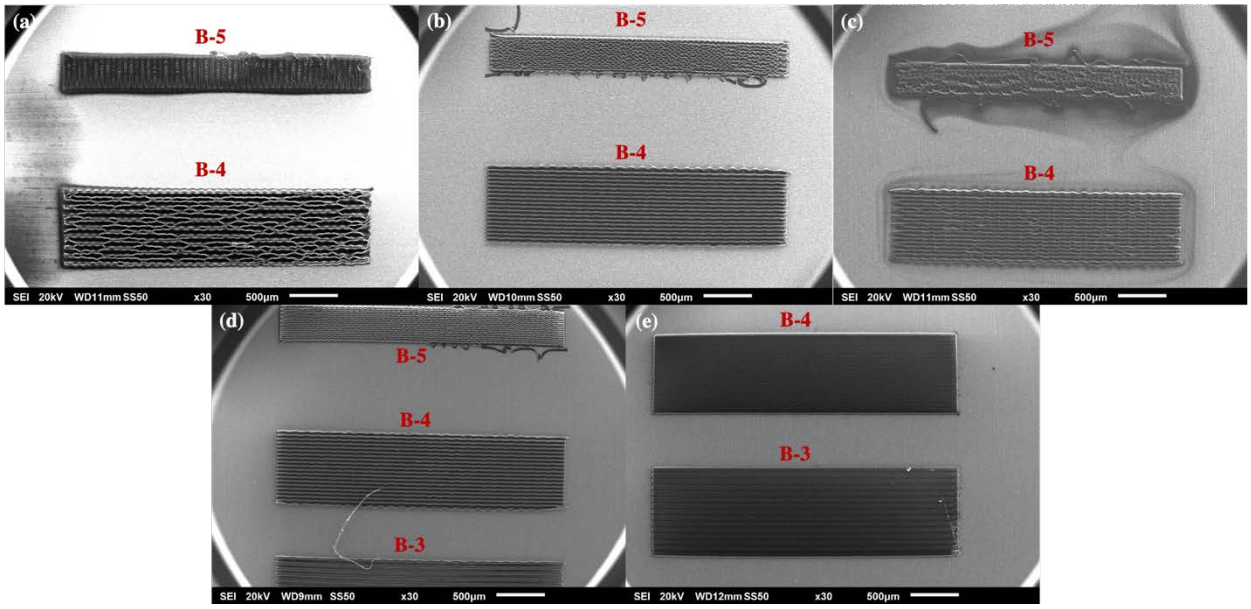

Figure 15. Performance of master mold on the rectangular structures with a development time of t_d=60s and an exposure time of (a) t_e=15s, (b) t_e=25s, (c) t_e=35s, (d) t_e=45s, and (e) t_e=55s.

Next, Figure 16 shows the square structures for different exposure times. For most of the exposure times, array C-1 were developed correctly. The smaller structures developed differently for each exposure time. For an exposure time of t_e=15s, the structures overexposed and in turn have moved and attached themselves to one another. For an exposure time of t_e=25s, the master mold was exposed sufficiently, hence all the structures were developed correctly. For an exposure time of t_e=35s, the smaller structures were overexposed in a non-uniform manner, causing overdevelopment to wash away the structures in D-2. For an exposure time of t_e=45s, underdevelopment and overdevelopment occurred, where D1 was overdeveloped while the D2 underdeveloped. Underdevelopment when the photoresist film is not dissolved sufficiently, causing undesired sections to remain on the copper plate. For the array D-2, the structures contain a dark background, which shows that the structures are underdeveloped. For array D-1, some square structures have deviated away from the array, indicating overdevelopment between the

photoresist film and the sodium carbonate solution. This inconsistency can happen because of a non-uniform exposure that can happen from being overexposed. For an exposure time of t_e=55s, D-1 and D-2 were overdeveloped because the structures were detached from the copper plate, but C-1 and C-2 were underdeveloped because they have rounder edges and the sharp edges of squares were not evident. This can also happen because of overexposure, similar to the t_e=55s case from the rectangular structure.

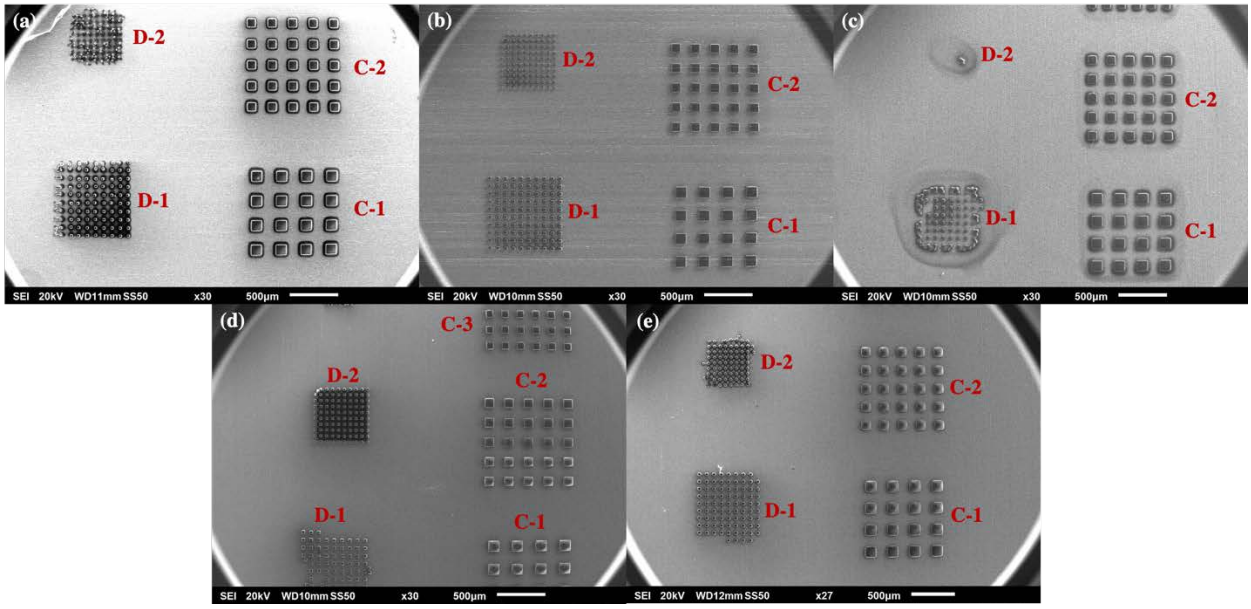

Figure 16. Performance of master mold on the square structures with a development time of t_d=60s and an exposure time of (a) t_e=15s, (b) 2 t_e=25s , (c) t_e=35s, (d) t_e=45s, and (e) t_e=55s.

Lastly, Figure 17 shows circular structures for various exposure times. The array E-1 has developed correctly for all exposure times. For the array D1, at an exposure time of t_e=15s, the structures had overdeveloped since the array of circles were squished together. This happens when the structures are detached from the copper plate slightly and moved around by the development solution. The cause of this phenomenon is underexposure of the UV light. For an exposure time of t_e=25s, arrays D1 and D2 have overdeveloped and underdeveloped at the same time. D1 was almost correctly developed, except for a portion at the top left corner, while D2 was underdeveloped. Array D1 and D2 at exposure times of t_e=35s, t_e=45s and t_e=55s have completely vanished due to extreme overdevelopment and overexposure.

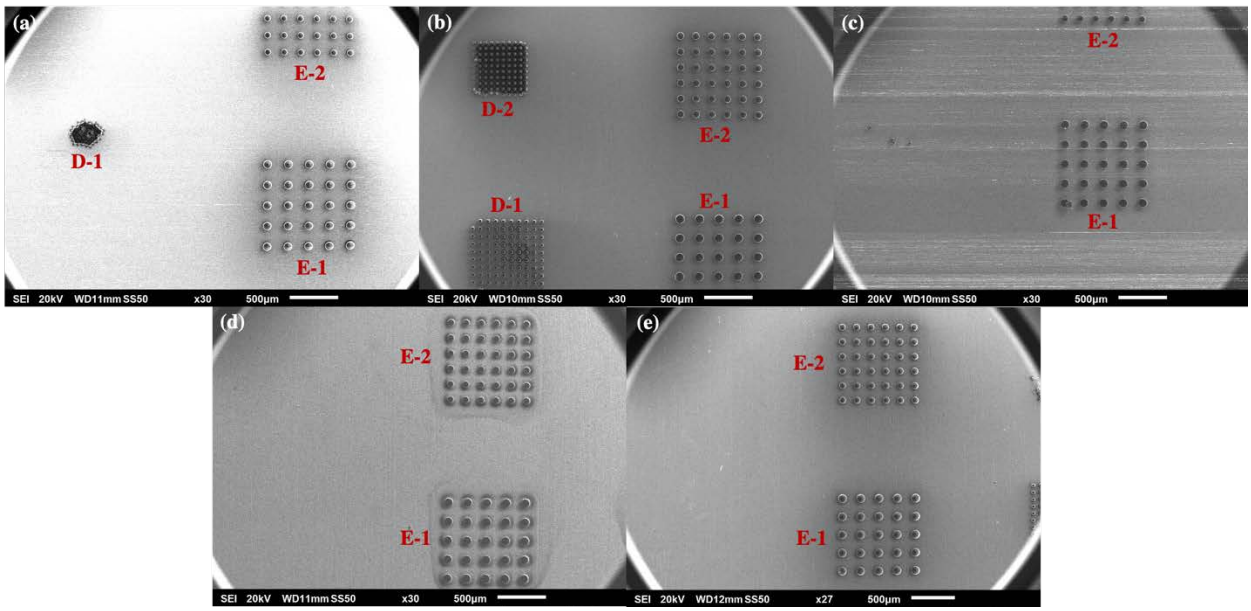

Figure 17. Performance of master mold on the circular structures with a development time of t_d=60s and an exposure time of (a) t_e=15s, (b) 2 t_e=25s , (c) t_e=35s, (d) t_e=45s, and (e) t_e=55s.

3.3.2 Effect of Photoresist Development Time in $NaCO_3$ Solution on Microstructures Resolution

In this section, the effect of different development times, t_d, of photoresist film in $NaCO_3$ solution with an exposure time of t_e=25s will be examined for the microstructures and observed under an SEM. Figure 18 shows the rectangular structures for different development times of photoresist film in $NaCO_3$ solution. Figure 18(a-e) represents development times of t_d=30s, t_d=45s, t_d=60s, t_d=75s and t_d=90s, respectively. A scale bar of 500µm is shown in each subfigure for the size reference of the microstructures. The microstructures appear to be significantly different for each development time. It is evident that for development times of t_d=30s and t_d=45s, the rectangular structures were underdeveloped. The background of the copper plate was darker compared to Figure 18(c), (d) and (e) because residual photoresist film was still present on the copper plate. For a development time of t_d=60s, array B-4 developed correctly while array B-5 was a little overdeveloped, where one rectangular structure deviated away from the array. For a development time of t_d=75s, some rectangular structures have detached themselves from both the arrays, showing overdevelopment of the rectangular photoresist structures. For a development time of t_d=90s, many rectangular structures deviated away from the copper plate and the arrays because of overdevelopment of the master mold.

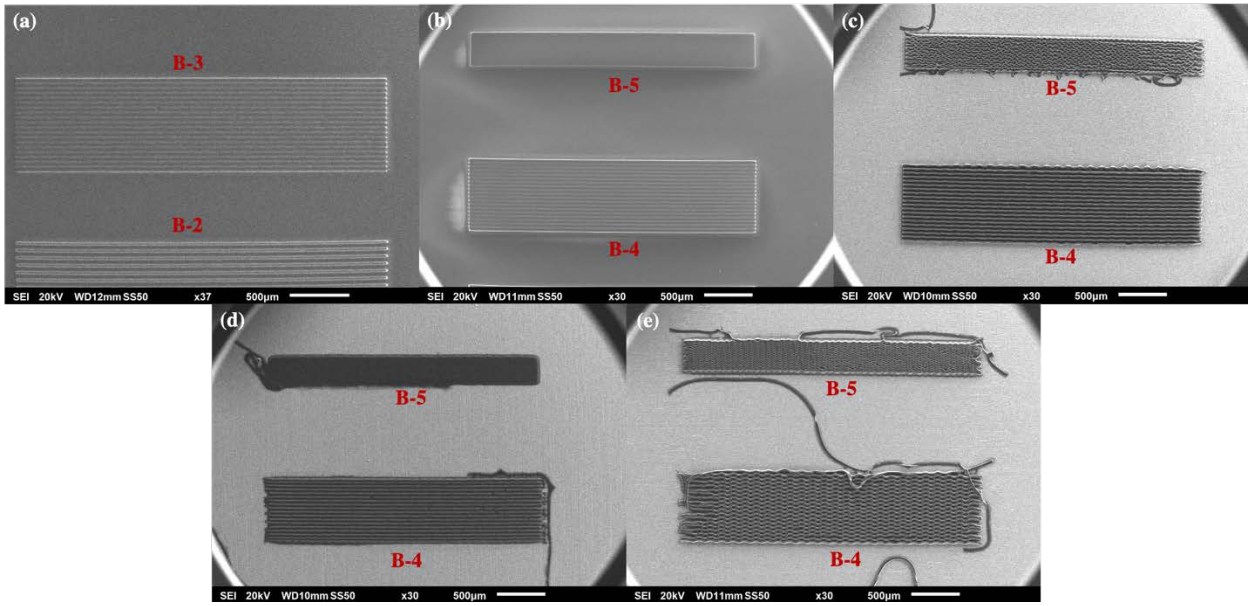

Figure 18. Performance of master mold on the rectangular structures with an exposure time of t_e=25s and a development time of (a) t_d=30s, (b) t_d=45s, (c) t_d=60s, (d) t_d=75s, and (e) t_d=90s.

Next, Figure 19 shows the square structures for different development times. For a development time of t_d=30s and t_d=45s, all the square structures were underdeveloped. Similar to the previous discussion, these structures did not develop properly, and residual photoresist film was still left on the copper plate. This can be seen by the background of Figure 19(a) and Figure 19(b) which are darker than the rest of the subfigures. The outline of the structures can be seen but there seems to be no depth to the structures because of the underdevelopment. For a development time of t_d=60s, the square structures have been developed properly. For a development time of t_d=75s, arrays C-1 and C-2 were developed properly, while D-1 and D-2 were overdeveloped. Both arrays of D-1 and D-2 were lifted off from the copper plate and deviated upwards. For a development time of t_d=90s, similar to t_d=75s, D-1 and D-2 were overdeveloped while C-1 and C-2 developed properly. The structures with t_d=90s have overdeveloped more than the structures with t_d=75s . C-1 and C-2 had sharp edges, but D-1 and D-2 deviated away from the original position. Furthermore, some of the smaller structures from D-1 and D-2 have attached to the larger structures in C-2.

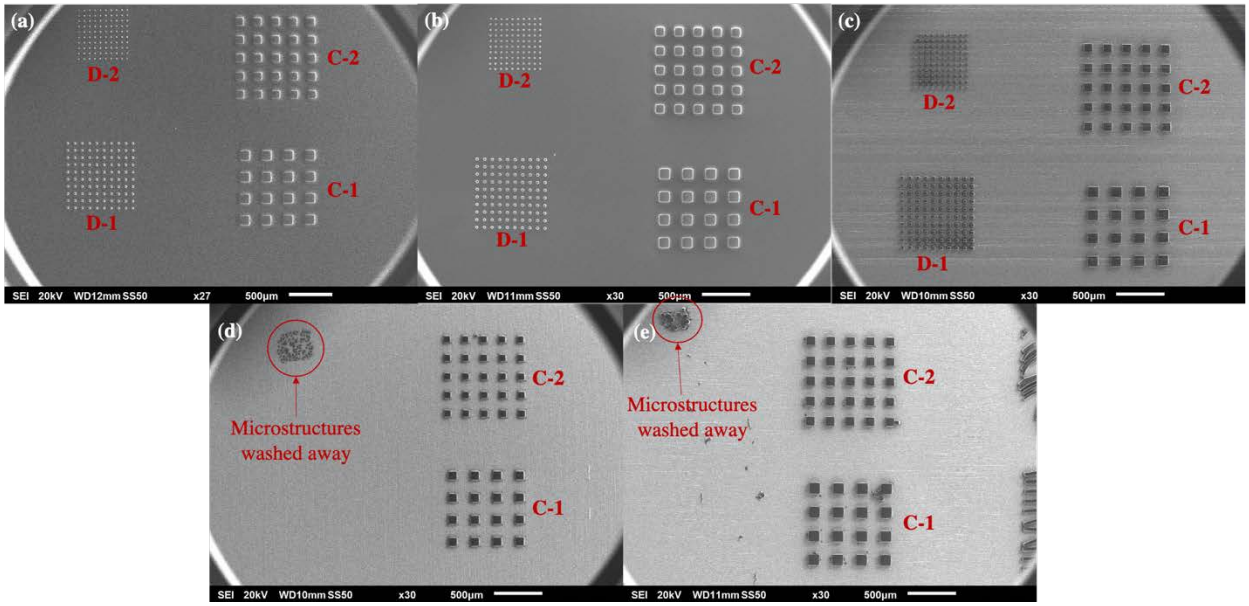

Figure 19. Performance of master mold on the square structures with an exposure time of t_e=25s and a development time of (a) t_d=30s, (b) t_d=45s, (c) t_d=60s, (d) t_d=75s, and (e) t_d=90s.

Lastly, Figure 20 shows circular structures for various development times. For the structures at development times of t_d=30s and t_d=45s, the circular structures are very underdeveloped, where the outlines of E-1 and E-2 can be seen, and the background of the copper plate is dark, showing that photoresist film still remains on the copper plate. The array D-2 from both the subfigures is not seen because the surrounding films was not developed properly (underdevelopment). For a development time of t_d=60s, arrays E-1 and E-2 were developed properly. Arrays D-1 and D-2 were underdeveloped, where one of the circular structures from the bottom array deviated away from the array. For a development time of t_d=75s, D-1 and D-2 were completely removed from the copper plate and some of the larger structures in E-1 and E-2 have also been overdeveloped. Clumps of structures can be witnessed at arbitrary areas, which originated from the structures that were overdeveloped away from the copper plate and migrated towards a different area. At a development time of t_d=90s, array E1 remained on the copper plate. This is because the t_d is huge compared to t_e, which weakens the bond between the photoresist film and the copper plate substantially. This configuration of t_d and t_e is detrimental to a master mold because not only does it removes important microstructures, it also moves it to an area where clogging can occur.

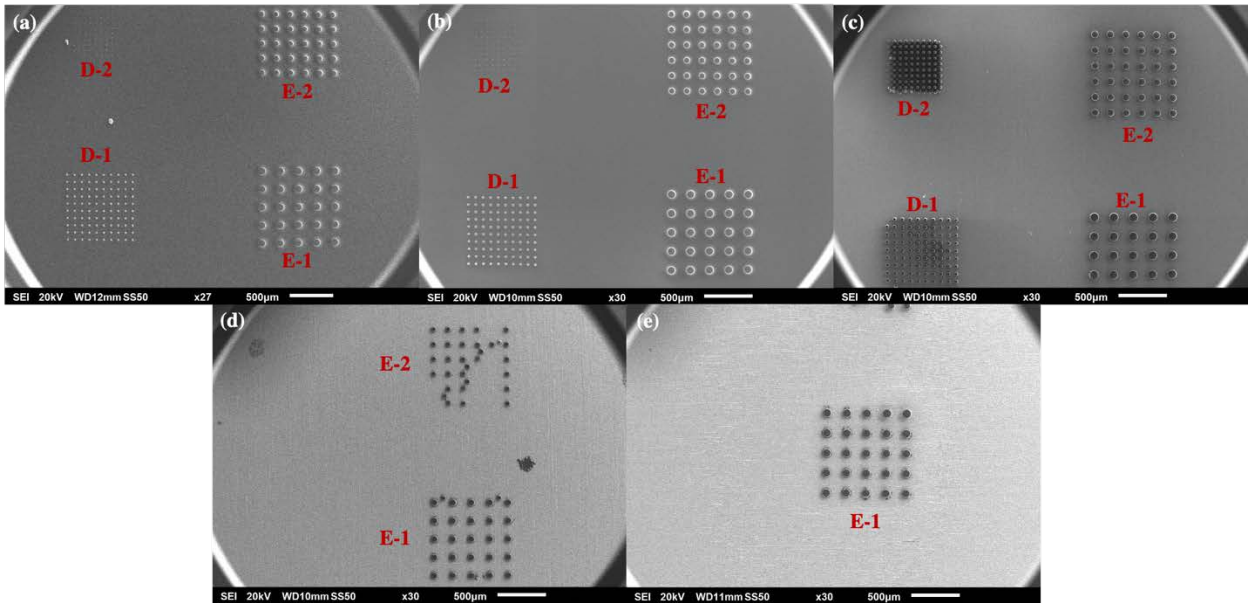

Figure 20. Performance of master mold on the circular structures with an exposure time of t_e=25s and a development time of (a) t_d=30s, (b) t_d=45s, (c) t_d=60s, (d) t_d=75s, and (e) t_d=90s.

From the discussion above, it can be concluded that the best pair of time for the exposure and development operations are an exposure time of t_e=25 seconds and a development time of t_d=60s. A more advanced SEM (Phenom XL G2, Nanoscience Instruments, Phoenix, AZ, USA) was used to capture a more magnified image of the square and circular structures of the master mold with t_e=25s and t_d=60s to show the isometric view of the structure (Figure 21). Figure 21(a) shows the square structures while Figure 21(b) shows the circular structures. A height of d=35µm was achieved, and the resolution of the structures are precise. Since the image from the SEM was taken at an angle, the image is not to scale. The appropriate measurements are shown in the figure.

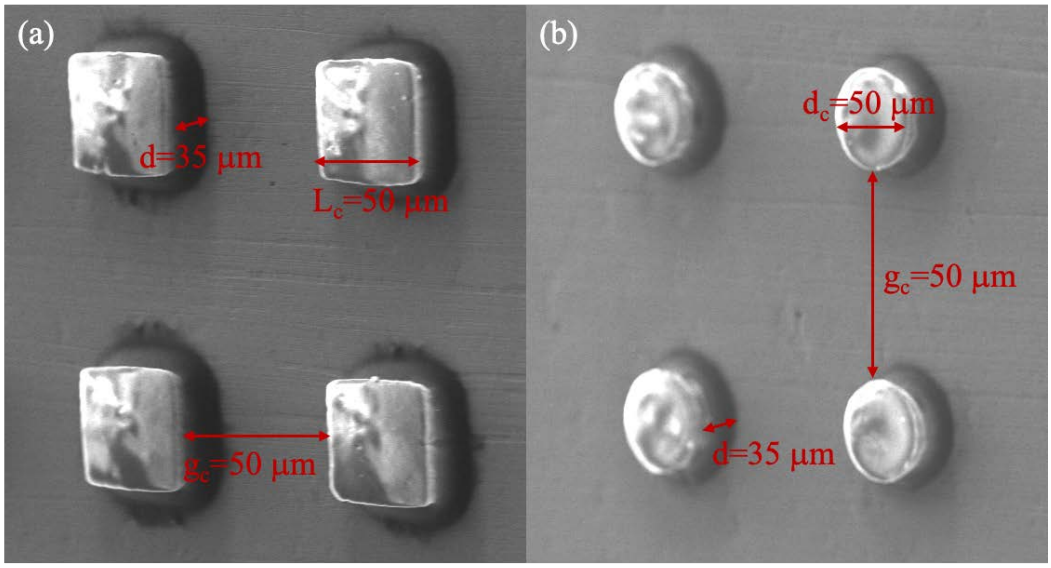

Figure 21. Magnified isometric view for a master mold with t_e=25s and t_d=60s. (a) Square structures with a height, d=35µm and length, L_c=50µm with a spacing of g_c=50µm. (b) Circular structures with a height of d=35µm and a diameter of d_c=50µm with a spacing of g_c=50µm.

3.3.3 Energy Dispersive Spectroscopy (EDS) for NdFeB-PDMS Microscale Magnet

In this section, the energy dispersive spectroscopy (EDS) analysis of the in-house fabricated microscale magnet using Phenom XL microscope is discussed. This method is done to analyze the elements that are present in the microscale magnet. First, a single layer microfluidic device was fabricated according to the Section 2.3.1 and the PDMS was peeled away from the glass slide after curing. After peeling, the NdFeB microscale magnet was attached to the glass slide, removing itself from the PDMS microfluidic device. The peeling is done to provide a direct contact between the material to be tested (NdFeB-PDMS microscale magnet) and the electron spectroscopy.

Figure 22 shows the chosen location on the microscale magnet to run EDS analysis. The image of the microscale magnet looks inconsistent because of the dissipation of elements in the SEM, since a high-vacuum pressure and secondary electron detector (SED) were activated. Table 3 shows the presence of elements at the chosen location together with the atomic and weight concentrations. Carbon was disabled because carbon is present in all organic materials and has close atomic energy to Boron. Oxygen, Silicon, Boron, Iron and Neodymium were present at the chosen location. Since carbon was eliminated from the analysis, the highest concentration was Oxygen. Silicon was the next element that was abundant at the chosen location. This shows that

the PDMS is present in the microscale magnet because PDMS is made of silicon. The final three elements detected in the microscale magnet were Boron, Iron and Neodymium, which are all part of NdFeB powder. This analysis shows that correct elements are present in the microscale magnet, hence validating the properties of the magnet.

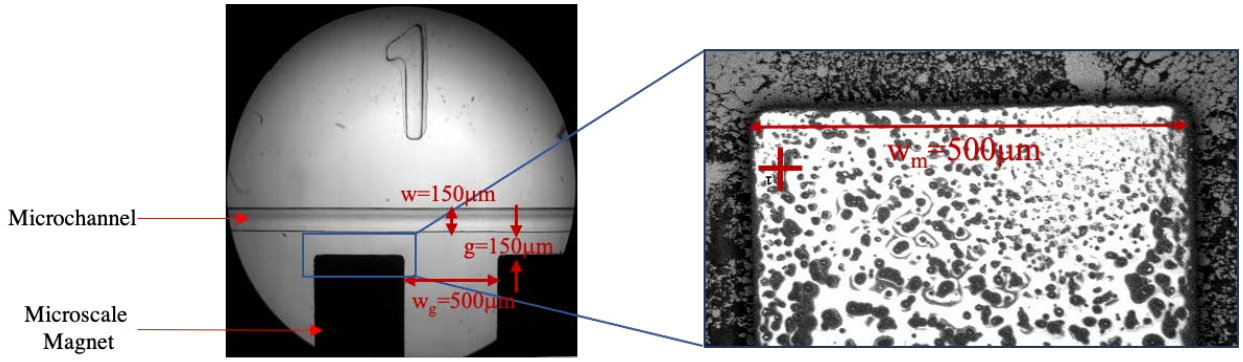

Figure 22. Image of the microscale magnet under EDS. The width of the channel, w=150μm, the width of the rectangular structure, w_m=500μm, the smallest distance between the magnet and the channel, g=150μm, and the distance between each rectangular structure of the magnet, w_g=500μm. The cross on the image shows the chosen location to undergo EDS analysis.

Table 3. Element concentrations in NdFeB-PDMS microscale magnet.

Element Number	Element Symbol	Element Name	Atomic Conc.	Weight Conc.
8	O	Oxygen	58.15	49.40
14	Si	Silicon	25.75	38.41
5	B	Boron	14.89	8.55
26	Fe	Iron	1.19	3.53
60	Nd	Neodymium	0.01	0.11

3.4 PDMS Resolution

The next step after evaluating the performance of the master mold was observing the resolution of the PDMS mold. An inverted light microscope (IN300TC-FL, Amscope, Irvine, CA, USA) was used to observe the resolution of the PDMS because the PDMS layer is transparent. Figure 23 shows some of the crucial areas where high quality fabrication system is important. Figure 23(a) shows the intersection of three inlets of a microchannel, where width of microchannel,

w=200μm. It can be seen that the grooves and edges of the microchannel are crisp and clean. Figure 23(b) shows the microstructure for the two-layer microscale magnet, where the width of the microstructure, l_m=100μm and the width of the gap, l_g=150μm. The rectangles were separated uniformly from one another. Furthermore, no obstruction was found inside or near the microstructure, which is important for the fabrication of the microscale magnet. Figure 23(c) shows the bottom part of the microscale magnet. It is important to note the sharp edges that are resulted from this fabrication system. The PDMS has taken the shape of the photoresist film from the master mold accurately. Having no obstructions and flaws in the PDMS for a microfluidic chip is important to make sure that the microfluidic experiment runs smoothly and that the device has a high-performance rate.

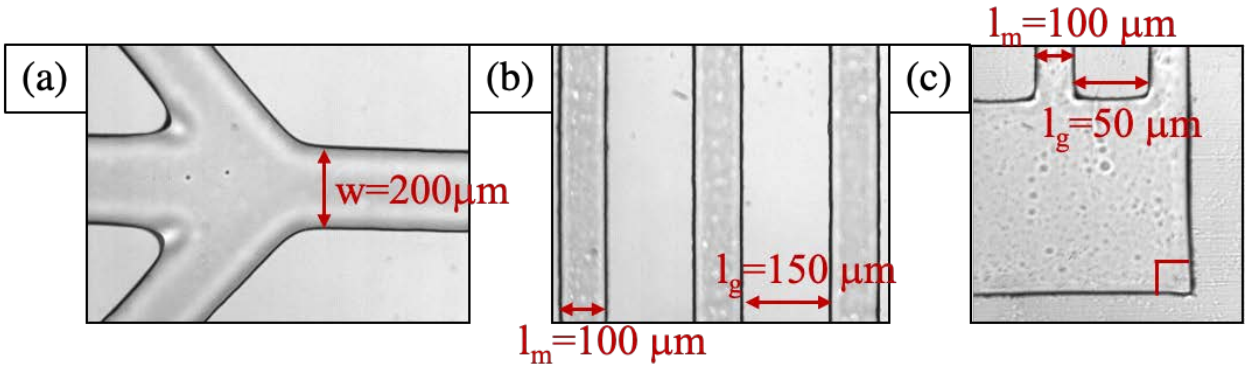

Figure 23. PDMS edges resulted from the low-cost fabrication system. (a) Intersection of three inlets to the main microchannel. (b) Structure to be a microscale magnet for the two-layer mixing system. (c) Edge of the microscale magnet in the two-layer mixing system.

Figure 24 shows the microscale magnet that is present in the one-layer microfluidic device, where the uniformity of the injected microscale magnet was observed. The width of the microchannel, w=150μm, the width of the rectangular structure, w_m=500μm, the smallest distance between the magnet and the channel, g=150μm, and the distance between each rectangular structure of the magnet, w_g=500μm. A mixture of NdFeB powder and PDMS was injected into the microstructure and the consistency of magnet is important for magnetic microfluidic operations. Sedimentation and agglomeration have been avoided and the magnet was very uniform because of the fast curing process. The microscale magnet has the appearance of a permanent magnet that was manufactured in the industry, which is the desired consistency. The consistency of the magnet is crucial because it affects the magnetic field gradient generated by the magnet. If the magnet does

not cure properly, the shape of the magnet will be altered by the presence of air pockets and NdFeB clumps. This will drastically change the magnetic field gradient and in turn the magnetic force imparted on microparticles will not be uniform.

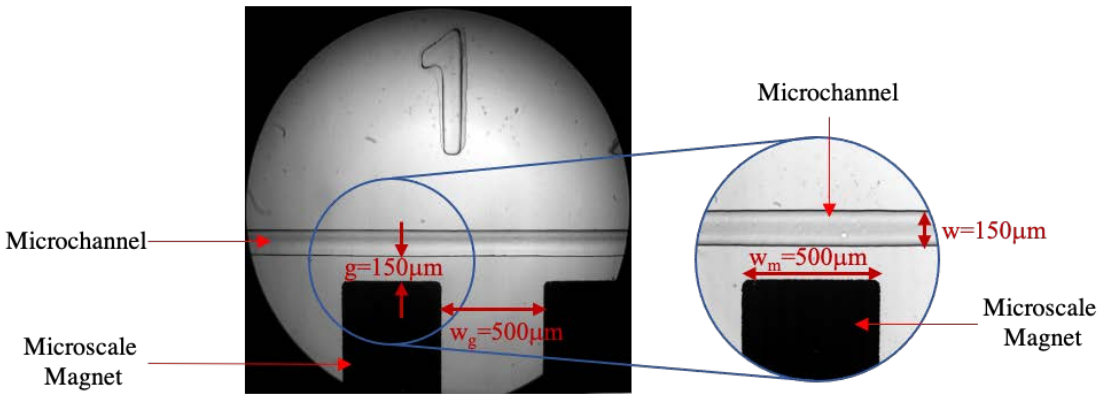

Figure 24. Consistency of the injected microscale magnet in one-layer microfluidic device. The figure shows all the dimensions and the zoomed figure shows clarity of the channel wall and microscale magnet

3.5 Light Intensity Performance

The intensity of the UV light source was detected at 9 different points with a light intensity detector. Figure 25 shows the positions where the light intensity was identified. The Position 5 is the pivotal position for the best exposure with the least amount of interference. Hence, the copper plate was placed at position 5 for the best exposure. In this section, the effect of different platform heights, h_p, ranging from h_p=5 cm to h_p=20 cm on the light intensity emitted onto the platform is investigated.

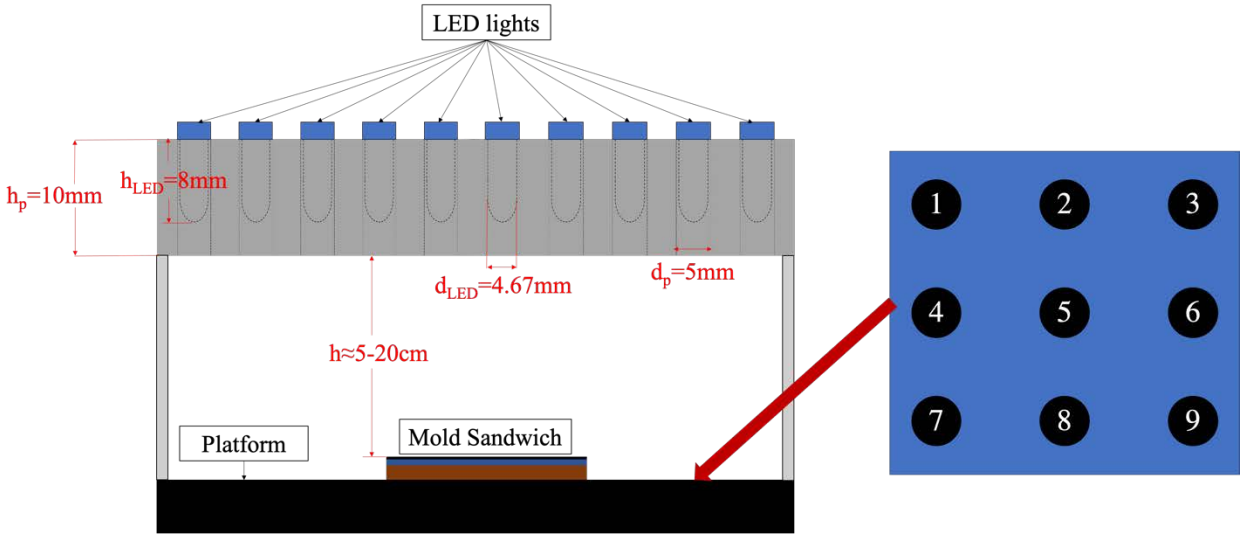

Figure 25. Front view of the exposure setup and possible positions of mold sandwich composed of copper plate, photoresist film and negative photomask on the platform during the exposure.

Figure 26 shows the light intensity at different heights, where the red solid line shows the light intensity read at Position 5 while the blue dashed line shows the average light intensity of all the positions. The light intensity, I, decreases when the distance between the master mold and the light source, h, increase. The highest intensity at Position 5 is I=77 μW/cm^2 and the lowest intensity is I=58 μW/cm^2. The highest average intensity is I=50 μW/cm^2 and the lowest intensity is I=38 μW/cm^2. The standard deviation of the light intensity at different positions at different heights is calculated (Table 4). It was found that the lower the standard deviation is, the more uniform the intensity of the light is. For this fabrication system, light intensity at Position 5 is more important compared to the uniformity of light intensity throughout the exposure platform. This is because the copper plate with the size of 2 inches by 3 inches will be placed at Position 5, so the rest of the locations are not as significant for the fabrication of this microfluidic system. However, having an overall uniform light source is important for the versatility of the light source. Hence, it can be concluded that a height of h=13cm from the platform is the most suitable for this operation because the uniformity is high and the light intensity at this height is suitable for the fabrication of master molds using the photoresist film.

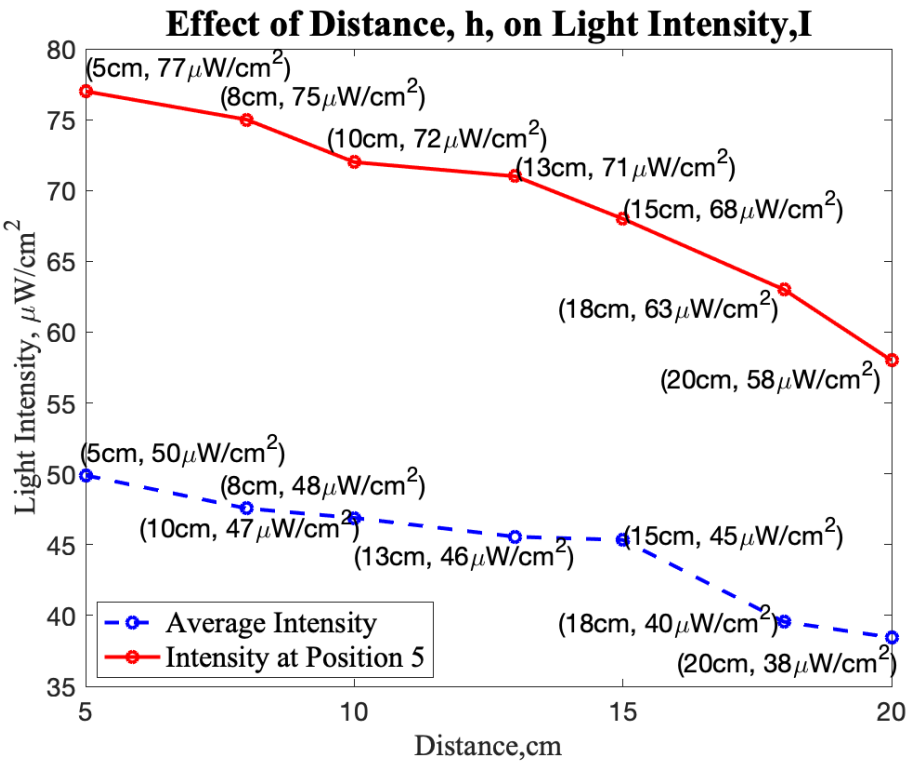

Figure 26. Light intensity, I, against the distance between the light source and the master mold, h. The red solid shows the intensity at position 5 while the blue dashed shows the average intensity between 9 positions.

Table 4. Standard deviation of the light intensity at different distance between the light source and the platform, h.

Distance master mold and light source, h (cm)	**Standard deviation of light intensity at 9 different locations (μW/cm^2)**
5	13.68799149
8	10.79480328
10	18.30604029
13	11.66309469
15	17.66352173
18	11.01261902
20	10.4774891

4. EXPERIMENTAL STUDY OF MICROFLUIDIC MIXING AND SEPARATION OF PARTICLES BASED ON THE DEVELOPED FABRICATION SYSTEM

4.1 Overview of Microfluidic Mixing

The objective of any fabrication system is to provide a stable and consistent method to build and manufacture a lab-on-chip device. The purpose of this fabrication system is to fabricate high throughput, low-cost microfluidic devices that utilizes magnetic fields on a microscale. Some of the applications include mixing of ferrofluid and distilled water with the magnet on the same plane, mixing of ferrofluid and distilled water with the magnet on a different plane and also to deviate and separate magnetic particles from non-magnetic particles. Mixing in microfluidics is a crucial step in mixing chemical reagents to induce reactions between samples and reagents, while separation of particles has been implemented in the detection and separation of circulating tumor cells and immunophenotyping. In this section, the mixing of ferrofluid and distilled water using and embedded microscale magnet, mixing of ferrofluid and distilled water in a two-plane device and the separation of magnetic and nonmagnetic particles using an embedded microscale magnet will be explored.

4.2 Mixing of Ferrofluid and Distilled Water using Embedded Microscale Magnet

The objective of this experiment is to mix ferrofluid and distilled water rapidly under different flow rates. As discussed in section 1.3, mixing on a micro scale is a well-known problem because of the presence of laminar flow, which does not allow easy mixing. The fabrication method in this application was discussed in section 2.3.1. According to this method, the resulting microfluidic device contains a micromagnet and a microfluidic channel on the same plane. The micromagnet generates a magnetic field that reacts with the magnetic nanoparticles in ferrofluid. As a result, the ferrofluid moves towards the magnet under the effect of the magnetic force exerted on the magnetic nanoparticles to be mixed with distilled water.

4.2.1 Work Concept of Mixing in Single Layer Microfluidic Device

Figure 27 shows the dimensions of the microfluidic device. Figure 27(a) shows the microfluidic mixing system that contains a microscale magnet with rectangles. The length of the microchannel and the micromagnet are L=2cm and the width of the microchannel is w=150µm, the closest distance between the micromagnet and the microchannel is g=150µm, the width of the a single rectangular magnetic structure is w_m=500µm, the height of the rectangles is h_m=1000µm, the distance between the rectangular structures are w_g=500µm and the width of the microbar (structure that connects all the rectangular structures) is j=500µm. Figure 27(b) shows the microfluidic mixing system with only a rectangular bar. The depth of all the structures is d=35µm, since the thickness of the photoresist film is 35µm. The microchannel consists of two inlets and one outlet, where ferrofluid is injected into the top inlet and distilled water is injected into the bottom inlet. This configuration is the best because the magnet is located near the lower part of the device and injecting ferrofluid to the top inlet will clearly show the migration and mixing of the two fluids clearly. The saturation magnetization of the microscale magnet is M_s=6.6 mT. The microscale magnet has protruding rectangular structures because this shape generates large magnetic gradients near the corners of the rectangles.

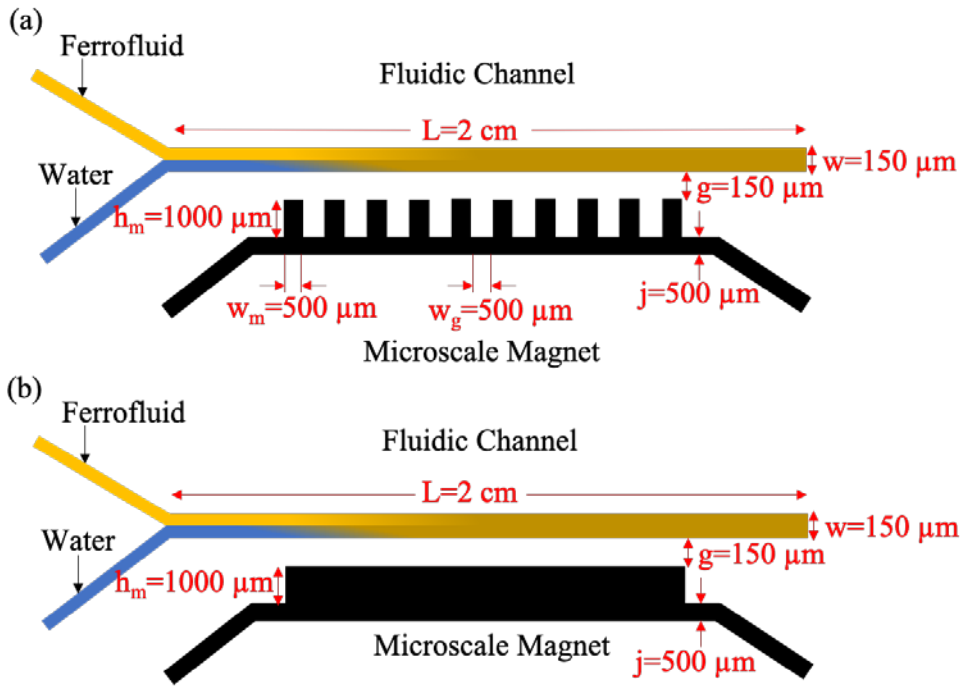

Figure 27. Dimensions of the single layer microfluidic device (a) with rectangular structures. (b) without rectangular structures and only a rectangular bar.

4.2.2 Finite Element Magnetic Analysis of Single Layer Microfluidic Device

In this subsection, the magnetic simulation procedure will be explained, which includes all the boundary conditions and properties. Magnetic field, B, was modelled using Finite Element Method Magnetics (FEMM) software to show the magnetic field gradients generated by the microscale magnet on a single layer device. First, the geometry of the devices is drawn in FEMM. Then, a large circular boundary that has a diameter, D=5L was drawn. Materials are created and set to each geometry. Since the purpose of this section is to solely show the magnetic field gradient of the microscale magnet, the microscale magnet is assigned NdFeB-PDMS while everything else, including the microchannel, is set air. NdFeB-PDMS was not a built-in material in the inventory of the software. Hence, properties were manually set according to the specification sheet from the manufacturer. Table 5 shows the properties of NdFeB-PDMS inputted into the software.

Table 5. Properties of NdFeB-PDMS for simulation of magnetic flux.

Properties	**Value**
Relative μ_x	1.049
Relative μ_y	1.049
Coercivity, H_c (A/m)	998333
Electrical conductivity, σ (MS/m)	0.667

Next, mixed boundary condition is applied to the microscale magnet which has a form as follows,

$$\left(\frac{1}{\mu_r \mu_0}\right)\frac{\partial \mathbf{A}}{\partial n} + c_0\mathbf{A} + c_1 = 0 \quad (1)$$

where μ_r is the relative permeability, μ_0 is the permeability of free space, **A** is the vector magnetic potential, c_0 and c_1 are the coefficients for field intensity. Robin boundary condition was chosen by setting c_0 to 31329713 (according to the property of the neodymium powder) and c_1 to 0. Next triangular mesh is created, and the problem is solved. In the post-processing section, the magnetic field gradient contours are analyzed.

The governing equations for this experiment are the continuity and momentum equations, assuming incompressible, laminar flow in steady state [48]:

$$\nabla \cdot \mathbf{u} = 0 \quad (2)$$

$$\rho(\mathbf{u} \cdot \nabla \mathbf{u}) = -\nabla P + \eta \nabla^2 \mathbf{u} + F_m \quad (3)$$

where **u** is the velocity of the fluid, ρ is the density of the fluid, P is pressure, η is the dynamic viscosity of the fluid and F_m is the magnetic force acting on the ferrofluid nanoparticles. The magnetic field intensity of the micromagnet, **H**, is calculated by solving the Maxwell equations using Finite Element Method Magnetics (FEMM) software. The magnetic flux density, **B**, is calculated using the equation below:

$$\mathbf{B} = \mu_0(1 + \chi_f)\mathbf{H} \quad (4)$$

where μ_0 is the vacuum permeability, which has a universal value of $4\pi\times10^{-7}$ H/m and χ_f is the magnetic susceptibility of the undiluted ferrofluid, which has a value of 0.5. The magnetic flux density can also be represented by the equation:

$$\mathbf{B} = \nabla \times \mathbf{A} \tag{5}$$

where **A** is the magnetic potential of the magnet. Based on previous work, the magnetic force acting on the ferrofluid in the x and y directions, respectively, are [[49]]:

$$F_{m,x} = \frac{C\chi_f}{\mu_0 \mu_r^2}\left(\frac{\partial \mathbf{A}_z}{\partial y}\frac{\partial^2 \mathbf{A}_z}{\partial x\,\partial y} + \frac{\partial \mathbf{A}_z}{\partial x}\frac{\partial^2 \mathbf{A}_z}{\partial x^2}\right) \tag{6}$$

$$F_{m,y} = -\frac{C\chi_f}{\mu_0 \mu_r^2}\left(\frac{\partial \mathbf{A}_z}{\partial x}\frac{\partial^2 \mathbf{A}_z}{\partial x\,\partial y} + \frac{\partial \mathbf{A}_z}{\partial y}\frac{\partial^2 \mathbf{A}_z}{\partial y^2}\right) \tag{7}$$

where C is the concentration of the ferrofluid and μ_r is the relative permeability, which can be represented by $1+ \chi_f$.

Figure 28(a) and (b) shows the contours of the magnetic field generated by a magnetic structure with rectangles and without rectangles, respectively. It can be seen clearly that the magnetic field gradient is higher around the microchannel in Figure 28(a) which contains the micromagnet with rectangles compared to Figure 28(b). The magnetic field is 0.022T along the streamwise direction of the microchannel for the magnet with rectangles. The magnetic field gradient is 0.022T near the inlet outlet of the microchannel for the bar magnet but it is less than 1.023e-7 T along the horizontal direction of the microchannel. This clearly shows the effect of the presence rectangular structures. Figure 29 shows the magnetic field gradient generated by the microscale magnet in the one-layer device to observe the magnetic field gradient closely. It can be seen that there is a strong magnetic field gradient generated near the corners of the rectangles. This is advantageous for particles separation and fluid mixing because strong magnetic forces can be exerted on the magnetic micro and nanoparticles during experiments.

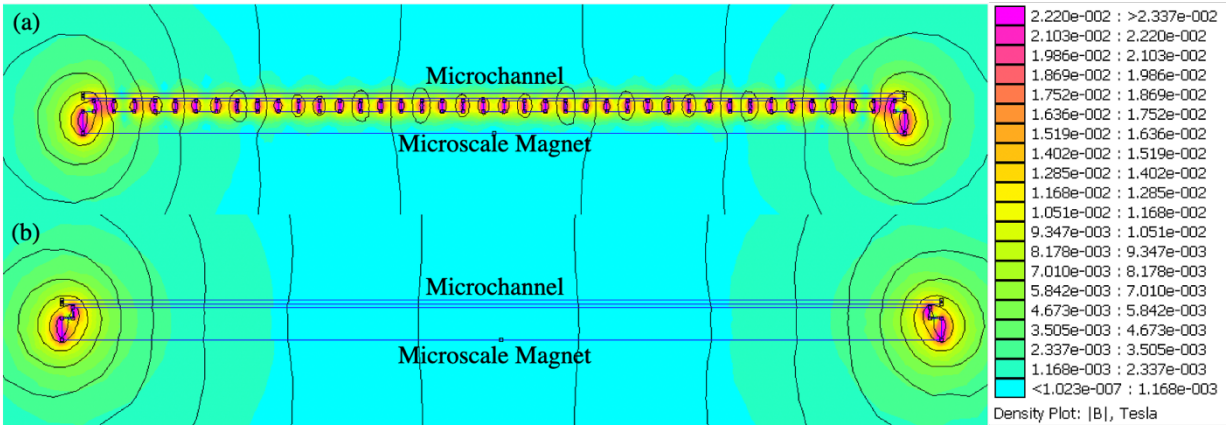

Figure 28. Magnetic flux contours for a micromagnet (a) with rectangular structures and (b) without rectangular structures.

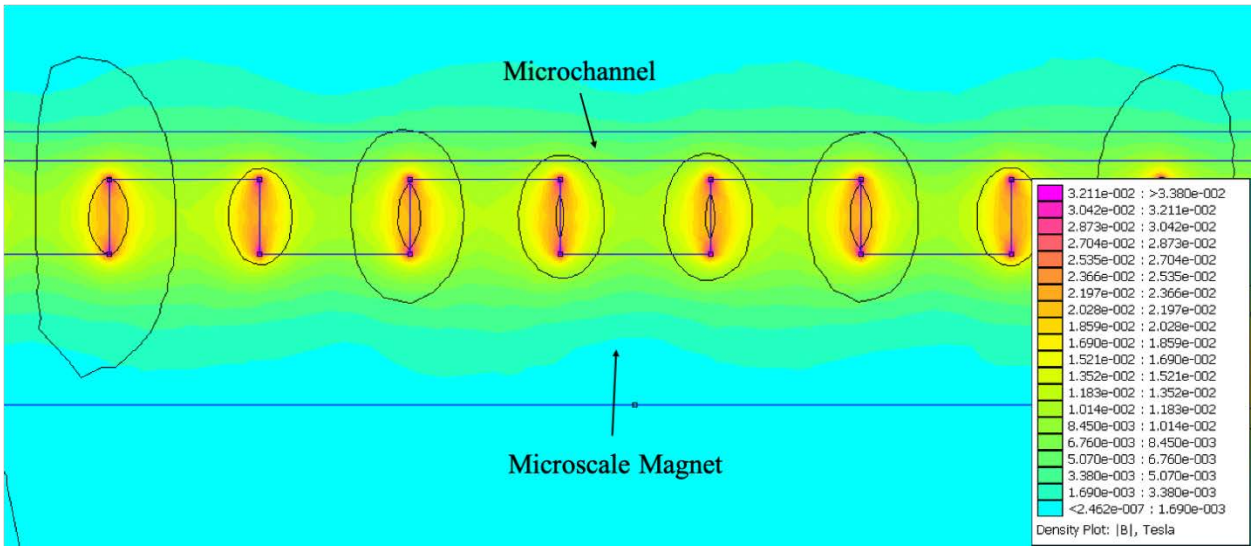

Figure 29. Magnetic field generated by one-layer microscale magnet with rectangular structures.

4.2.3 Experimental Setup and Materials

Figure 30(a) and (b) show the schematic and the arrangement of the experimental setup for this rapid mixing method, respectively. Before the initiation of the experiment, two 1 mL syringes were filled with water-based ferrofluid (EMG 408, Ferrotec Inc., Santa Clara, CA, USA.) and distilled water, respectively. Two syringe pumps (Cole Parmer/KD Scientific 74900, Holliston, MA, USA) were placed on the left side of the experimentation platform and the filled syringes were mounted on the syringe pumps. In order to ensure no disruption and air bubbles occur during

the experiment, the syringes are required to be mounted onto the syringe pumps properly. The instructions for proper mounting are as follows:

1. The syringe is filled with the desired fluid, and all air bubbles are removed.
2. A luer is fitted to a flexible tube with an inner diameter of 0.031 inch, which is fitted to another tube with an outer diameter of 0.03 inch.
3. The luer is connected to the syringe.
4. The fluid is pushed through the tubes until it is ¾ filled.
5. The adjustable pusher block is retracted, and the syringe is placed on the pump. The front part of the syringe flange is aligned to the front stopper and secured to the pump.
6. The pusher block is moved towards the syringe until it barely touches the syringe.
7. A desired flow rate is inputted to the pump and activated.
8. When the syringe fills up fully and droplets exit the 0.03-inch tube, the syringe is connected to the microfluidic device.

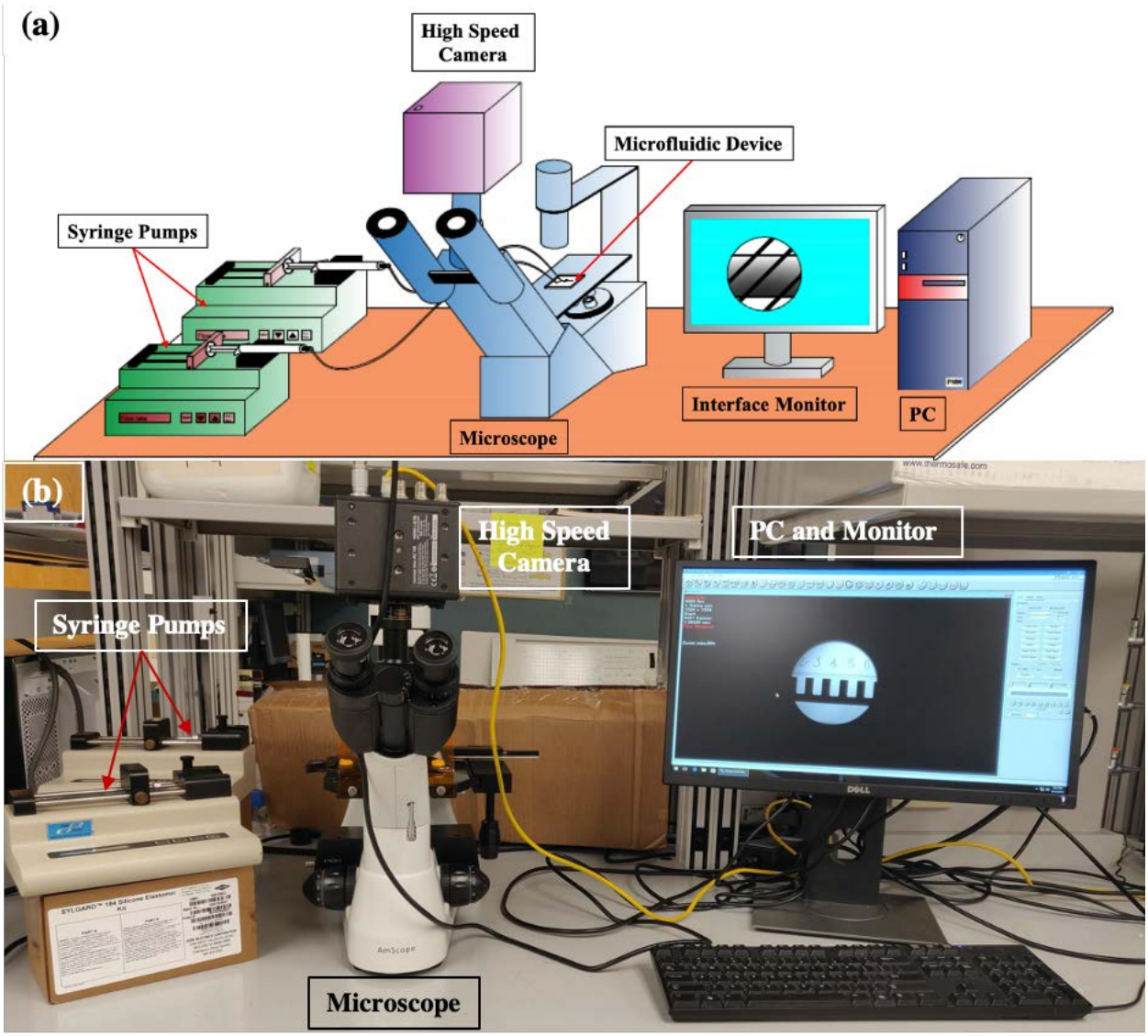

Figure 30. (a) Sketch and (b) Experimental setup for mixing of ferrofluid and distilled water. Syringe pumps are located at the far left, microscope is located in the middle and the computer is located at the far right for analysis.

At the center of the experimentation platform is the Amscope IN300TC-FL inverted microscope, where a high-speed camera (Photron AX100, Photron, Tokyo, Japan) is mounted. A high-speed camera is necessary for experiments on a microscale for post-processing and analysis of the results. A microfluidic device was placed on the observation platform of the microscope. Two tubes from the syringe pumps corresponding to the ferrofluid and distilled water were injected to the top and bottom inlets of the device, respectively. The outlet of the device was connected to a tube that led to an exhaust container that collects the fluid that has been mixed. On the right side

of the platform is a computer that is connected to the high-speed camera. Images and videos of the fluids in microchannel were acquired by Photron AX100, which is an image and video acquisition system that is compatible with the high-speed camera. Images of the fluids before and after passing by the magnet were acquired. The concentration of the magnetic nanoparticles suspended in the ferrofluid is 1.2% (v/v), with a dynamic viscosity of μ=2 mPa·s and magnetic susceptibility of χ_f=0.5. This information was obtained from the data sheet provided by Ferrotec (USA) Corporation [50].

4.2.4 Results and Discussion

In this section, the mixing results of the single layer micromixer are discussed and analyzed using a mixing degree C_m of the fluids [51],[52]. MATLAB computed the mixing degree for all the mixtures with different parameters. For the single layer experiment, mixing performance was analyzed at x=0mm, x=5mm, x=10mm, x=15mm and x=20mm. At each of these locations, the behavior of the mixture was recorded and inputted into MATLAB. The mixing degree is represented by the pixel intensity of the fluids the equation for mixing degree is represented as,

$$C_m = 1 - \frac{\sqrt{\frac{1}{N}\sum_{i=1}^{N}(X_i - \bar{X})^2}}{\bar{X}} \tag{8}$$

where N is the total number of pixels in the image, X_i is the intensity of each pixel in the image and $\bar{X}$ is the average intensity of all the pixels. The top portion, $\sqrt{\frac{1}{N}\sum_{i=1}^{N}(X_i - \bar{X})^2}$, of the equation indicates the standard deviation of the pixel intensity while the bottom portion, $\bar{X}$, shows the average pixel intensity. Three different parameters were varied to find the best configuration for mixing in this device. Case 1 contains a micromagnet with rectangular structures, case 2 contains a micromagnet with no rectangular structures but only a bar, case 3 contains no magnet while case 4 contains a micromagnet with rectangular structures but the volume percentage ratio between distilled water and ferrofluid is 2:1. Figure 31 shows the chosen locations of observation and analysis of x=0mm, x=5mm, x=10mm, x=15mm and x=20mm, where 0mm is the closest to the inlet while 20mm is the closest to the outlet. The flow rates are varied in each experiment.

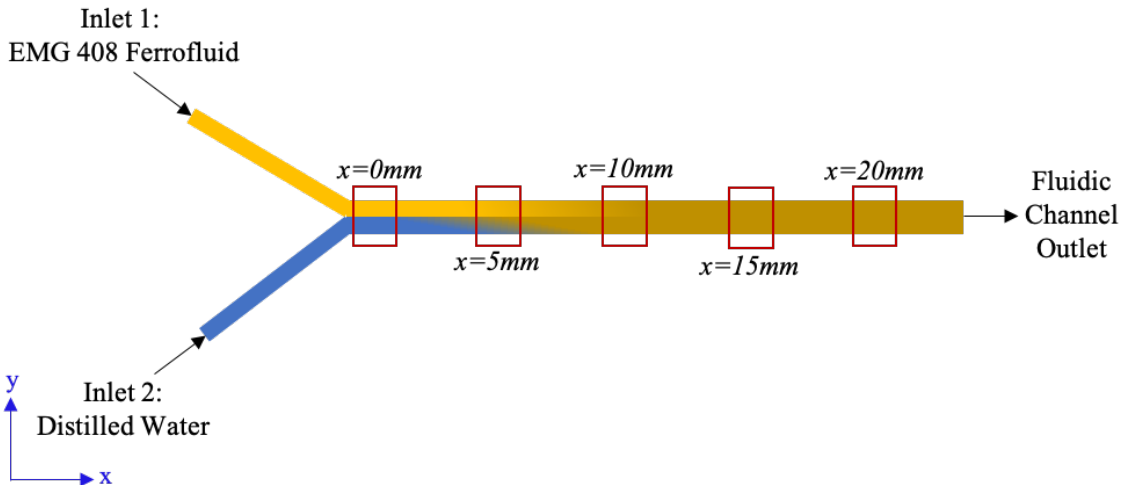

Figure 31. Inlet 1 and inlet 2 of the microfluidic channel are injected with ferrofluid and distilled water, respectively. The five observation locations, x=0mm, x=5mm, x=10mm, x=15mm and x=20mm are shown.

4.2.4.1 Case 1: Micromagnet with Rectangular Structures

Figure 32 shows a graph of mixing degree against the x-location of observation for different flow rates in case 1. Case 1 is performed in a microfluidic device that contains a micromagnet with rectangular structures and a volume percentage ratio of 1:1 between ferrofluid and distilled water. The flow rates shown are Q=0.04ml/hr, Q=0.1ml/hr, Q=0.2ml/hr, Q=0.4ml/hr, Q=1.0ml/hr and Q=2.0ml/hr. It can be seen that the mixing degree for all the flow rates increase with location. When the fluids move away from the inlet, the residence time between the two fluids increases, which leads to a better mixing performance. Another important aspect to be noted is the effect of flow rate on the mixing degree at the same position of the microchannel. The mixing degree decreases for increasing flow rate at the same streamwise x location. As the volumetric flow rate Q increases, the residence time for the nanoparticles to react to the magnetic force created by the uniform magnetic field decreases. Hence, the nanoparticles migrate less with a higher flow rate, resulting in a nonhomogeneous mixture.

Figure 32 also shows the scatter plot for the mixing performance with some images from the experimental results for flow rates of Q=0.04ml/hr and Q=2.0ml/hr. At the inlet, there was a sharp interface between the ferrofluid and distilled water. For a flow rate of Q=0.04ml/hr, the fluids were thoroughly mixed at 10mm. This is because of the phenomenon explained earlier, which is a longer residence time for the magnetic force to act on the nanoparticles in the ferrofluid. For a flow rate of Q=2.0ml/hr, an interface was present at every location, which shows that

complete mixing did not occur. At x=20mm, the area occupied by the ferrofluid was larger than the area occupied by the distilled water, which means that the ferrofluid started to move towards the magnet at x=20mm. This is almost similar to the result at x=5mm for a flow rate of Q=0.04ml/hr, where a small portion of distilled water can be observed at the lower end of the channel. The reason for this is the residence time between the fluids is smaller for a higher flow rate, hence, longer channel length is needed to produce homogenized mixtures at higher flow rates.

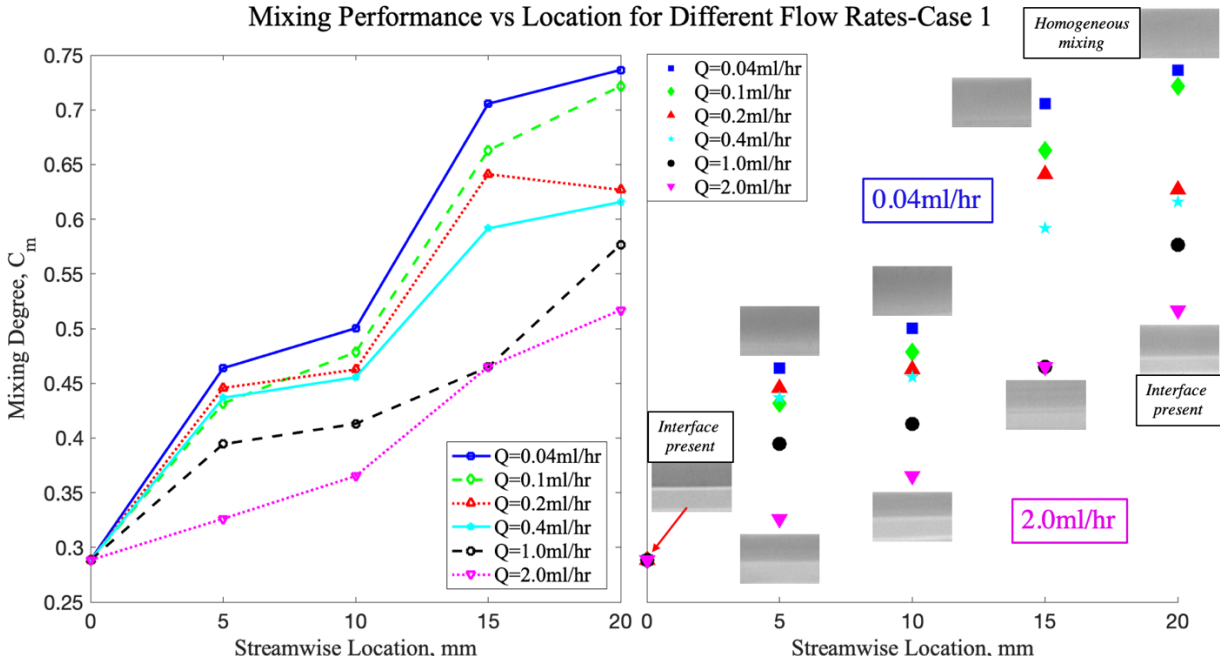

Figure 32. Graph of mixing performance against the streamwise location of mixing for flow rates of Q=0.04ml/hr, Q=0.1ml/hr, Q=0.2ml/hr, Q=0.4ml/hr, Q=1.0ml/hr and Q=2.0ml/hr. Images for Q=0.04ml/hr and Q=2.0ml/hr are shown. The mixing results are for case 1 which contains a micromagnet with rectangular structures and a volume percentage ratio of 1:1 for ferrofluid:distilled water.

4.2.4.2 Case 2: Micromagnet with Rectangular Bar

Figure 33 shows a graph of mixing degree against the location of observation for different flow rates in case 2. Case 2 is performed in a microfluidic device that contains a micromagnet with no rectangular structures, but a rectangular bar and a volume percentage ratio of 1:1 between ferrofluid and distilled water. The flow rates shown are Q=0.04ml/hr, Q=0.1ml/hr, Q=0.2ml/hr, Q=0.4ml/hr, and Q=1.0ml/hr. It is evident that the mixing degree for all the flow rates increase with the streamwise flow. The residence time and flow rates effect the mixing degree of the fluids.

Similar to case 1, mixing degree decreased for increasing flow rate at the same streamwise location. The residence time is not sufficient for the nanoparticles in ferrofluid to react with the magnetic field and migrate.

Figure 33 also includes the scatter plot for the mixing performance with some images from the experimental results for flow rates of Q=0.04ml/hr and 1.0ml/hr. There was a sharp interface between the ferrofluid and distilled water at the inlet. For a flow rate of Q=0.04ml/hr, the interface was very faint at x=20mm, which shows that incomplete mixing has happened. For a flow rate of Q=1.0ml/hr, an interface was present at every location, which shows that mixing did not occur. All of the experimental images for this flow rate look similar because the parameters are not suitable for complete mixing. For case 2, the experiments are only done until a maximum total flow rate of Q=1.0ml/hr because the results shows that mixing did not happen at this flow rate. From the correlation between flow rate and mixing degree, as the flow rate increases, mixing degree decreases. When no mixing is observed at Q=1.0ml/hr, a higher flow rate is not necessary to prove this point. This design of micromagnet is just a straight rectangular bar compared to case 1 which contained a micromagnet with rectangular structures. As mentioned in Section 4.2.2, the magnetic field gradient for a magnetic bar is much lower compared to the rectangular structures, due to the absence of critical geometry that increases the mixing degree. A lower magnetic field gradient imparts a lower magnetic force on the magnetic nanoparticles present in ferrofluid according to equations 6 and 7. When a lower magnetic force acts on the nanoparticles, the nanoparticles, tend to stay in their respectively laminar flow paths to conserve momentum, which in turn leads to a lower mixing degree.

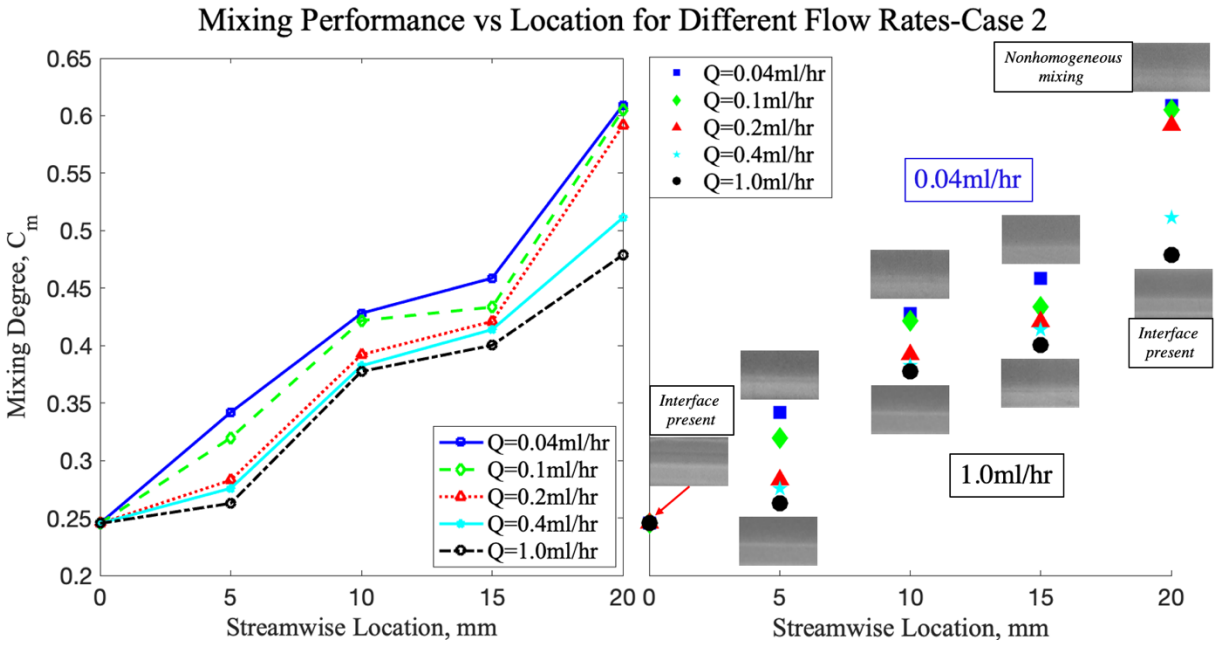

Figure 33. Graph of mixing performance against the streamwise location of mixing for flow rates of Q=0.04ml/hr, Q=0.1ml/hr, Q=0.2ml/hr, Q=0.4ml/hr and Q=1.0ml/hr. The results are for case 2 which contains a micromagnet without rectangular structures and a volume percentage ratio of 1:1 for ferrofluid:distilled water. Images for 0.04ml/hr and 1.0ml/hr are shown.

4.2.4.3 Case 3: Absence of Micromagnet

Figure 34 shows a graph of mixing degree against the location of observation for different flow rates in case 3. Case 3 is performed in a microfluidic device that does not contains a micromagnet and a volume percentage ratio of 1:1 between ferrofluid and distilled water. The flow rates shown are Q=0.04ml/hr, Q=0.1ml/hr, Q=0.2ml/hr, and Q=0.4ml/hr. Although the mixing degree is not as high as those from case 1 and case 2, they increased with increasing distance from the inlet for all flow rates. However, the mixing degree decreased with increasing flow rate.

Figure 34 also portrays the scatter plot for the mixing performance with some images from the experimental results for flow rates of Q=0.04ml/hr and Q=0.4ml/hr. A sharp interface is apparent at every experimental image, except for flow rate of Q=0.04ml/hr at x=20mm. This is because molecular diffusion had been initiated by the ferrofluid, where the nanoparticles have started to migrate towards the magnetic field gradient. The area of ferrofluid was more than the area of distilled water for flow rate of Q=0.04ml/hr at x=15mm because the ferrofluid migrated towards the magnet. For a flow rate of Q=0.4ml/hr, a sharp interface was present at every location, which shows that mixing did not occur. For case 3, the experiments were only done until a

maximum total flow rate of Q=0.4ml/hr because the results showed that mixing did not happen at this flow rate. The highest degree of mixing achieved was C_m=0.52, which means that the mixing is not homogeneous. Since a trend is found for this case, which is as the flow rate increases, the mixing degree decreases, experiments are stopped at Q=0.4ml/hr to conserve resources. Unlike previous experimental group, case 3 has no magnet to expedite the mixing process. Hence, molecular diffusion was the sole cause for the partial mixing at the outlet at a flow rate of Q=0.04ml/hr. Since the diffusion coefficient of ferrofluid is higher than that of distilled water, the molecules from the ferrofluid tends to move towards areas with no ferrofluid nanoparticles to reach an equilibrium state. However, as mentioned in the introduction (Section 1.3), the process of molecular diffusion for mixing takes a long channel length and reaction time, which in turn increases the sample size.

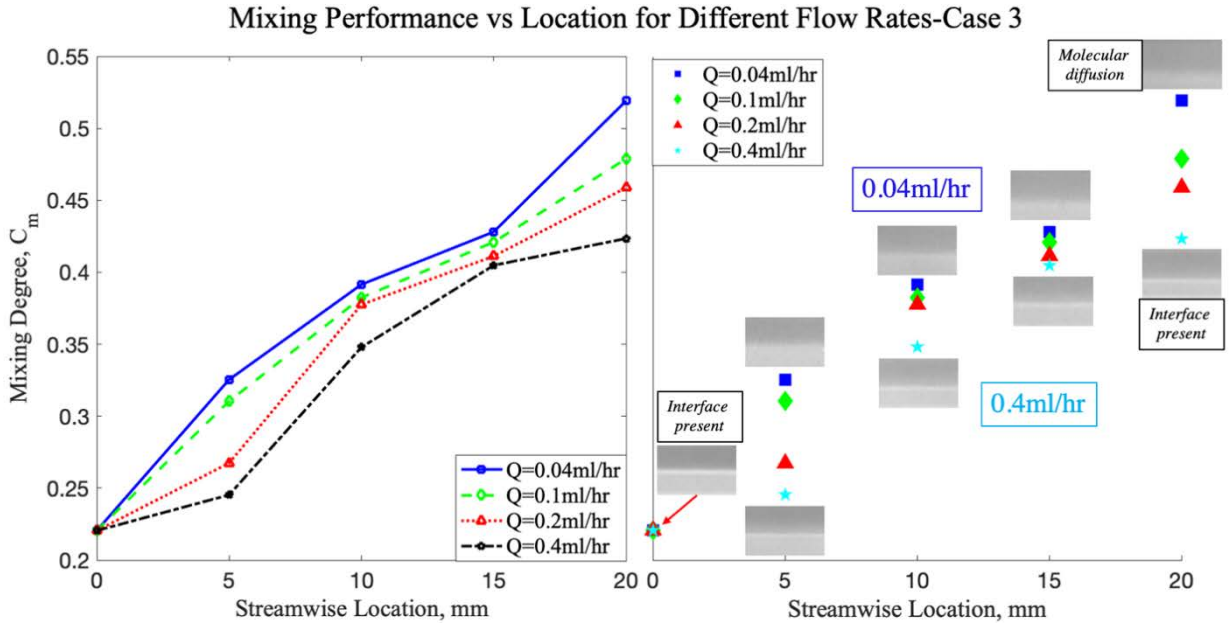

Figure 34. Graph of mixing performance against the streamwise location of mixing for flow rates of Q=0.04ml/hr, Q=0.1ml/hr, Q=0.2ml/hr and Q=0.4ml/hr. Images for Q=0.04ml/hr and Q=0.4ml/hr are shown. The results are for case 3 which contains a volume percentage ratio of 1:1 for ferrofluid:distilled water and does not contain a micromagnet.

4.2.4.4 Case 4: Volume Percentage Ratio of 2:1 between Distilled Water and Ferrofluid

Figure 35 shows a graph of mixing degree against the location of observation for different flow rates in case 4. Case four is performed in a microfluidic device that contains a micromagnet with rectangular structures and a volume percentage ratio of 2:1 between distilled water and ferrofluid. The flow rates shown are Q=0.04ml/hr, Q=0.1ml/hr, Q=0.2ml/hr, Q=0.4ml/hr, Q=1.0ml/hr and Q=2.0ml/hr. It is apparent that the mixing degree for all the flow rates increase with increasing distance from the inlet. The residence time and flow rates effect the mixing degree of the fluids. The mixing degree increased for decreasing flow rate at the same horizontal location.

Figure 35 also shows the scatter plot for the mixing performance with some images from the experimental results for flow rates of Q=0.04ml/hr and Q=2.0ml/hr. There was a sharp interface between the ferrofluid and distilled water at x=0mm to x=10mm and the interface fades after that point. The results for flow rates of Q=0.04ml/hr and Q=2.0ml/hr at x=20mm appeared to be similar, but after analysis, the mixing degree is higher for the lower flow rate. One can also observe that the area occupied by the ferrofluid is larger at the lower flow rate. For case 4, the experiments were continued up to Q=2ml/hr, similar to case 1, because the results and analysis show some degree of mixing happening even at a high flow rate of Q=1.0ml/hr. Hence, all the flow rates were tested to find a trend between the flow rate and the mixing degree.

The residence time and flow rates effect the mixing degree of the fluids. The mixing degree increases for decreasing flow rate at the same horizontal location. Even though the volume concentration of ferrofluid was lower in this group, the mixing performance was relatively high because of the usage of the micromagnet with rectangular structures. As mentioned in Section 4.3.2, the magnetic field gradient for the rectangular structures is much higher compared to only the rectangular bar. Hence, after the experimentation of this group, it can be concluded that the effect of magnetic field is greater than the effect of volume percentage on the mixing degree of ferrofluid.

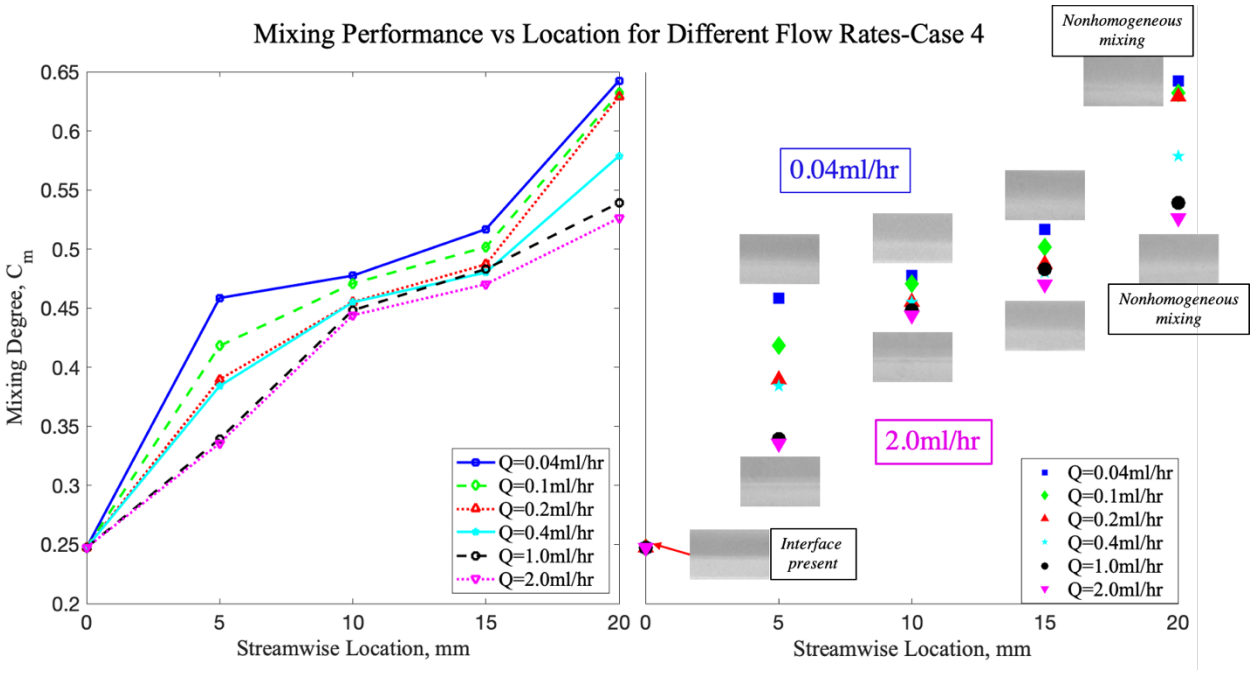

Figure 35. Graph of mixing performance against the streamwise location of mixing for flow rates of Q=0.04ml/hr, Q=0.1ml/hr, Q=0.2ml/hr, Q=0.4ml/hr, Q=1.0ml/hr and Q=2.0ml/hr. Images for Q=0.04ml/hr and Q=2.0ml/hr are shown. The results are for case 4 which contains a micromagnet with rectangular structures and a volume percentage ratio of 2:1 for distilled water:ferrofluid.

4.2.4.5 Discussion

This subsection discusses the relationship between all the cases and the comparison of the parameters. Table 6 shows all the mixing performances for cases 1-4 with respect to the flow rate and streamwise location. Figure 36(a) and (b) shows the graphs of mixing degree against the streamwise location of observation for the four different cases at flow rates of Q=0.04ml/hr and Q=0.4ml/hr, respectively. These flow rates are chosen because they showcase the best mixing degrees suitable for discussion, where Q=0.04ml/hr is the lowest flow rate while Q=0.4ml/hr is the highest common flow rate between all four groups. To recap, case 1 has a magnet with rectangular structures, case 2 has a rectangular bar magnet, case 3 does not have a magnet while case 4 has a 2:1 volume percentage ratio between distilled water and ferrofluid.

Table 6. Table of mixing performances for cases 1-4 at different flow rates and locations

		Mixing Degree, C_m			
Cases	**Flow Rates, Q(ml/hr)**	**x=5mm**	**x=10mm**	**x=15mm**	**x=20mm**
1	0.04	0.4638	0.5003	0.7055	0.7365
	0.1	0.4317	0.4784	0.6628	0.7216
	0.2	0.4457	0.4626	0.6411	0.6268
	0.4	0.4367	0.4555	0.5916	0.6157
	1	0.3944	0.413	0.4648	0.5768
	2	0.3262	0.3652	0.4651	0.517
2	0.04	0.3419	0.4281	0.4587	0.6091
	0.1	0.3197	0.4217	0.4335	0.6048
	0.2	0.2829	0.3921	0.421	0.5915
	0.4	0.2758	0.3824	0.4139	0.5112
	1	0.2627	0.3775	0.4002	0.4788
3	0.04	0.3254	0.3915	0.4281	0.5191
	0.1	0.3104	0.3824	0.421	0.4788
	0.2	0.2674	0.3775	0.4112	0.4587
	0.4	0.2453	0.3479	0.4048	0.4235
4	0.04	0.4586	0.4775	0.5168	0.6425
	0.1	0.4181	0.4709	0.5017	0.6321
	0.2	0.3897	0.4552	0.487	0.629
	0.4	0.3841	0.455	0.4802	0.5788
	1	0.3393	0.4482	0.4831	0.5392
	2	0.3357	0.444	0.4703	0.5262

The trends for both the flow rates are similar, where case 1 has the highest mixing degree, followed by case 4, case 2 and lastly, case 3. Case 1 and case 4 have higher mixing degree compared to case 2 and case 3 because case 1 and case 4 contains the micromagnet with rectangular structures. From Figure 28, the difference in the magnetic field gradient between the rectangular bar and rectangular structures is evident because of the presence of sharp corners in the rectangular structures. Since the magnetic field gradient is more prominent in the micromagnet with rectangular structures, the magnetic force imparted on the ferrofluid nanoparticles is higher. Hence, a considerable migration of the ferrofluid nanoparticles happened, which led to a completely mixed solution.

Even though both the devices in cases 1 and 4 contain the micromagnet with rectangular structures, case 4 had lower mixing degree because of the lower volume percentage of ferrofluid that was present in the mixing solution. Case 1 contained a volume percentage ratio of 1:1 while case 4 contained a volume percentage ratio of 2:1 between the distilled water and ferrofluid. In other words, for case 1, 50% of the fluid is ferrofluid while 50% is distilled water. For case 4, only 33.33% is ferrofluid while the rest (66.67%) is distilled water. Hence, a smaller number of nanoparticles were present in case 4, which decreased the cumulative magnetic force experienced by the nanoparticles to mix homogeneously with distilled water, which in turn decreased the mixing degree.

Case 3 has the lowest mixing degree because no magnet was present to accelerate the mixing process. As mentioned in the introduction, without hydrodynamic or external forces, mixing on a micro level happens solely due to molecular diffusion, which led to a very low mixing degree in case 3. Case 3 can be considered as a control case to show that mixing was expedited by the presence of magnetic field and not any other unknown parameter. Case 2 has a higher mixing degree compared to case 3 because of the presence of a magnetic bar. However, the magnetic gradient created by the magnetic bar is not prevalent because the force imparted on the nanoparticles was insufficient to induce motion for mixing of ferrofluid and distilled water.

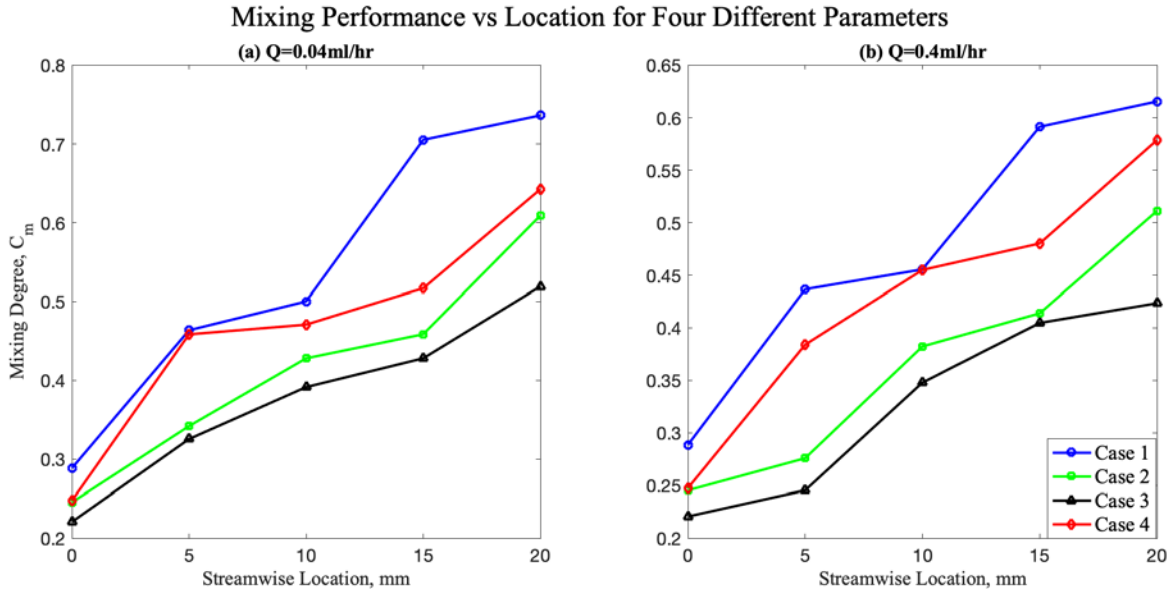

Figure 36. Graph of mixing performance against the horizontal location of mixing for cases 1-4 for flow rates of (a) 0.04 ml/hr and (b) 0.4 ml/hr.

4.3 Mixing of Ferrofluid and Distilled Water on a Two-Layer Device

The purpose of this experiment is to rapidly mix ferrofluid and distilled water using a microscale permanent magnet that is located on a different plane with respect to the microchannel. This experiment is similar to the experiment in Section 4.2 because of the similarity in the application, but the novelty of this device is the location and the design of the microscale magnet. The fabrication method in this application is discussed in Section 2.3.2, which produces two different layers of PDMS containing a microchannel and a magnetic microstructure, respectively.

4.3.1 Work Concept of Mixing in Two-Layer Microfluidic Device

Figure 37 shows two views of the two-layer microfluidic mixing device, where Figure 37(a) is the top view while Figure 37(b) is the front view. After the bonding procedure, the microchannel and micromagnet are coincident, which increases the magnetic force intensity that is imparted by the permanent magnet towards the ferrofluid. The length and width of the microchannel are L=2cm and w=1000μm, respectively. The magnetic microstructure is in an array of magnetic bars, which each have a width of l_m=100μm, the width of the entire array is n=2100μm, and the distances between each magnetic bar is l_g=100μm. Similar to the single layer device, the depth of all the structures is d=35μm, since the thickness of the photoresist film is 35μm. The microchannel consists of two inlets and one outlet, where ferrofluid is injected into the bottom inlet and distilled water is injected into the top inlet. This configuration is the best because the direction of magnetization of the microscale magnet is upwards, which will migrate the ferrofluid nanoparticles upwards towards the distilled water. The saturation magnetization of the microscale magnet is M_s=6.6 mT. The microscale magnet contains bars that generate a cumulative magnetic field and gradient, which mixes the fluids rapidly.

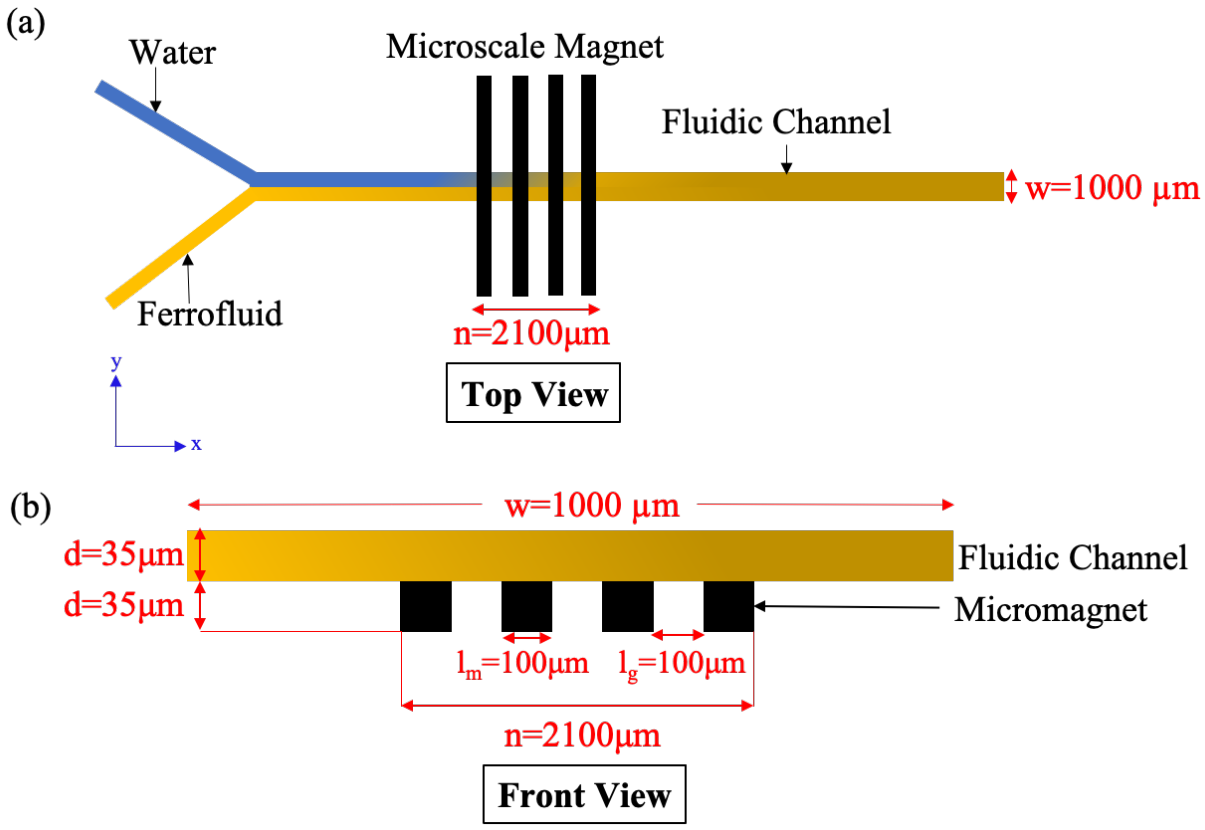

Figure 37. (a) Top view of two-layer mixing. Water is injected in the top inlet and ferrofluid is injected into the bottom inlet. (b) Side view of two-layer mixing.

Parametric study was conducted, where two parameters and their effects were evaluated. The parameters chosen were total flow rate, Q, and the density of the magnetic array to find the optimum mixing efficiency of this device. Two devices were fabricated, where one microfluidic chip had an array of 4 magnetic structures bonded perpendicular to the channel. The alternative case was a microfluidic chip with an array of 7 magnetic structures bonded perpendicular to the microchannel. The ratio of flow rate between the ferrofluid and distilled water was 1:1, which means that the volume flow rate of ferrofluid and distilled water is the same at all times. Eight different flow rates were chosen to show the influence of flow rate of the mixing performance of the system. The magnetic nanoparticle concentration of the ferrofluid is 1.2% (v/v).

4.3.2 Finite Element Magnetics Analysis of Two-Layer Microfluidic Device

The magnetic simulation, materials and boundary conditions are similar Section 4.2.2. In this two-layer mixing device, the maximum magnetic flux, which is present at the location of the magnets, is 0.0321T (Figure 38). The governing equations for this experiment are the same as the previous experiment because of the similar concept of mixing of ferrofluid using a microscale magnet.

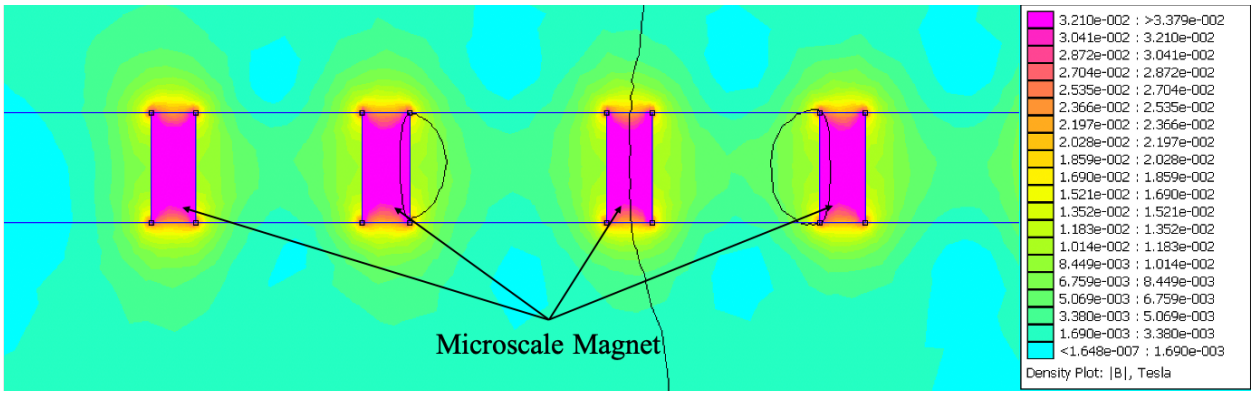

Figure 38. Magnetic field generated by the two-layer NdFeB microscale magnet. This device contains an array of 4 magnetic bars.

4.3.3 Experimental Setup and Materials

The experimental setup and materials in this study is the same as the setup and materials discussed in Section 4.2.3.

4.3.4 Results and Discussion

In this section, the results of the two-layer micromixer are discussed. The results were analyzed using a mixing degree, C_m of the fluids, which was discussed in Section 4.2.4. For the two-layer experiment, mixing was analyzed at the streamwise location where the magnet was located. The behavior of the mixture after passing by the magnetic array was recorded and inputted into MATLAB. The mixing degree is calculated using pixel intensity discussed in Equation 8. Since this is a novel experimental setup, a microchannel width of w=1000μm was chosen to show the trend and theory behind this micromixer.

Two different parameters were varied to find the best configuration for mixing in this device. Case 1 contains a magnetic array with 4 magnetic strips and a volume percentage ratio of 1:1 between distilled water and ferrofluid. Case 2 contains a magnetic array with 4 magnetic bars and a volume percentage ratio of 2:1 between distilled water and ferrofluid. Case 3 contains a magnetic array with 7 magnetic strips and a volume percentage ratio of 1:1. The flow rates were varied in each experiment.

4.3.4.1 Case 1: Two Layer Device with 4 Array Micromagnet and Volume Percentage Ratio of 1:1 for Distilled Water to Ferrofluid

Figure 39 shows a graph of mixing degree against the flow rate at flow rates ranging from Q=0.02ml/hr to Q=4ml/hr. Case 1 for the two-layer micromixer contains a magnetic array with 4 magnetic bars and a volume percentage ratio of 1:1 between distilled water and ferrofluid. It is evident that the mixing degree decreased with increasing flow rates. As the flow rate increases, the residence time between ferrofluid and distilled water becomes smaller, resulting in incomplete mixing. The experimental pictures are shown for some of the important flow rates. At a flow rate of Q=0.04ml/hr, the mixture was found to be homogenized because the ferrofluid and distilled water cannot be distinguished. At a flow rate of Q=0.2ml/hr, an interface was observed but the area that contained distilled water is dark, which shows that ferrofluid has migrated, but the mixing is not complete. At a flow rate of Q=1.6ml/hr, the interface was more prominent and at a flow rate of Q=4.0ml/hr, no mixing was observed.

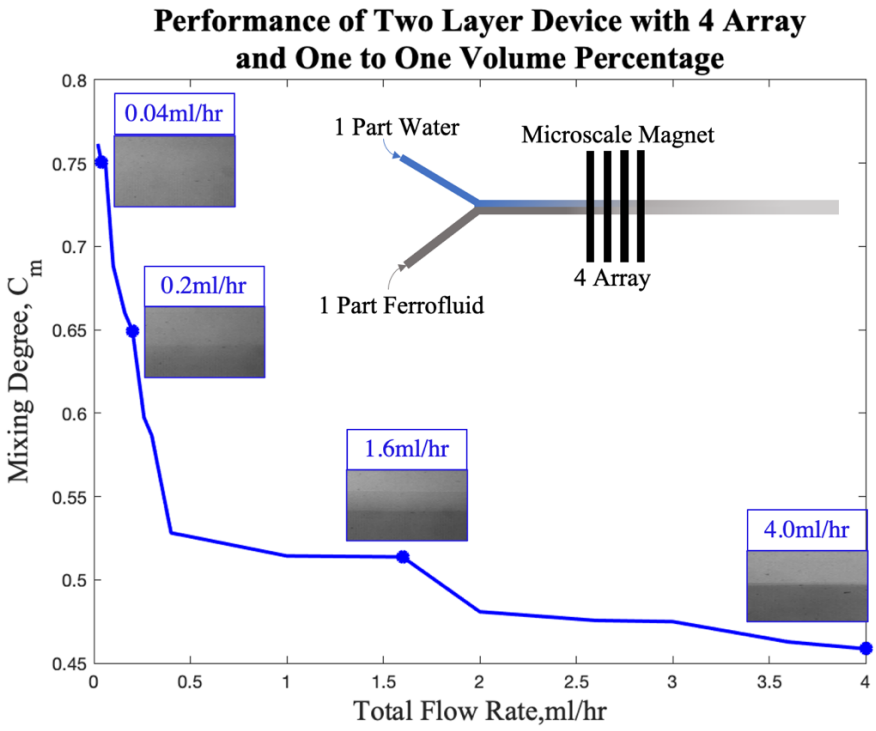

Figure 39. Graph of mixing performance against the flow rate for 4 array micromagnet for a volume percentage of 1:1 for distilled water to ferrofluid. The top right corner shows a two-dimensional top view of the two-layer device. The images show the ferrofluid and distilled water at the outlet.

4.3.4.2 Case 2: Two Layer Device with 4 Array Micromagnet and Volume Percentage Ratio of 2:1 for Distilled Water to Ferrofluid

Figure 40 shows a graph of mixing degree against the flow rate at flow rates ranging from Q=0.02ml/hr to Q=4.0ml/hr. Case 2 for the two-layer micromixer comprises of a magnetic array with 4 magnetic bars and a volume percentage ratio of 2:1 between distilled water and ferrofluid. It can be seen that as the flow rate increases, the mixing degree decreases because of the same reasons for the experiments above. The experimental pictures are shown for Q=0.04ml/hr, Q=0.2ml/hr, Q=1.6ml/hr and Q=4.0ml/hr. The mixture at a flow rate of Q=0.04ml/hr had a mixing degree of C_m=0.7684 because of the long residence time between the fluids. The mixing degree was the lowest at a flow rate of Q=4.0ml/hr, and it is evident with the appearance of the sharp interface. The interface was still present at a flow rate of Q=1.6ml/hr, but it was not as sharp as the interface at Q=4.0ml/hr. Similar to case 1, the ferrofluid has migrated towards the distilled water at a flow rate of Q=0.20ml/hr and this can be seen from the upper half that is darker at this flow rate compared to the higher flow rates.

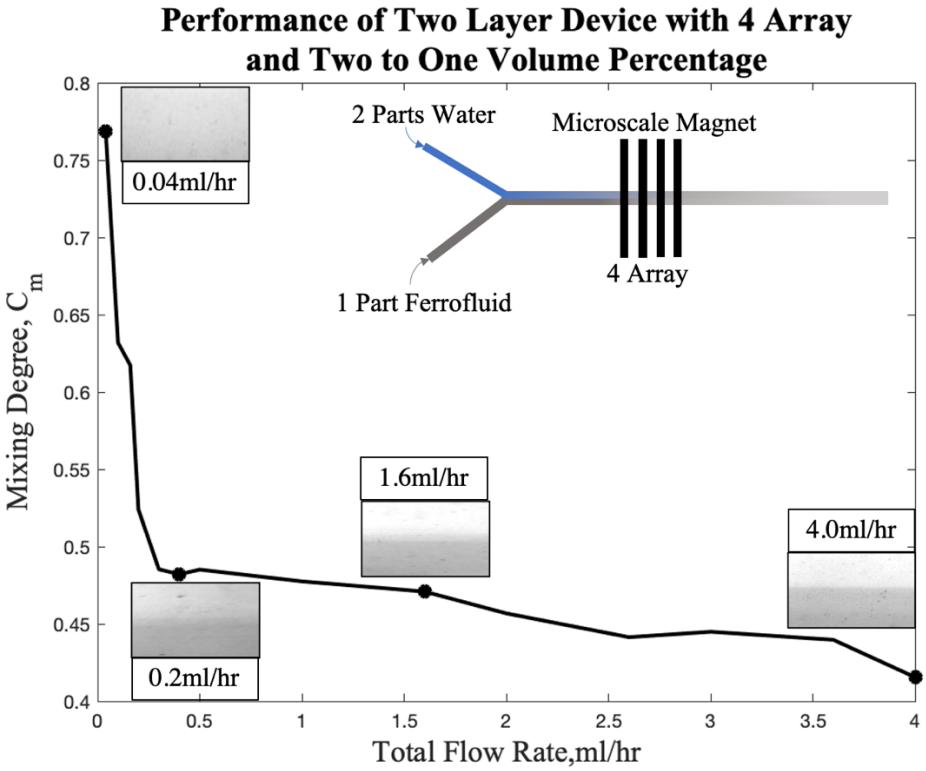

Figure 40. Graph of mixing performance against the flow rate for 4 array micromagnet with a volume percentage ratio of 2:1 for distilled water to ferrofluid. The top right corner shows a two-dimensional top view of the two-layer device. The images show the ferrofluid and distilled water at the outlet.

4.3.4.3 Case 3: Two Layer Device with 7 Array Micromagnet and Volume Percentage Ratio of 1:1 for Distilled Water to Ferrofluid

Figure 41 shows a graph of mixing degree against the flow rate at flow rates ranging from Q=0.02ml/hr to Q=4ml/hr for case 3 that contains a magnetic array with 7 magnetic bars and a volume percentage ratio of 1:1 between ferrofluid and distilled water. Similar to the previous experiments and parametric studies, the mixing degree decreases when the flow rate increases. At a flow rate of Q=0.04ml/hr, the mixture was homogenized, with a mixing degree of more than C_m=0.8. The mixture was still mixed well at a flow rate of Q=0.2ml/hr. This can be explained by the increased number of magnetic strips in the array, which increased the magnetic field gradient. An increased magnetic field gradient increases the magnetic force imparted on the ferrofluid nanoparticles. The difference between the fluids was evident at a flow rate of Q=1.6ml/hr where an interface was seen, but the interface was not sharp. At a flow rate of Q=4.0ml/hr, there was a distinct segregation between the fluids.

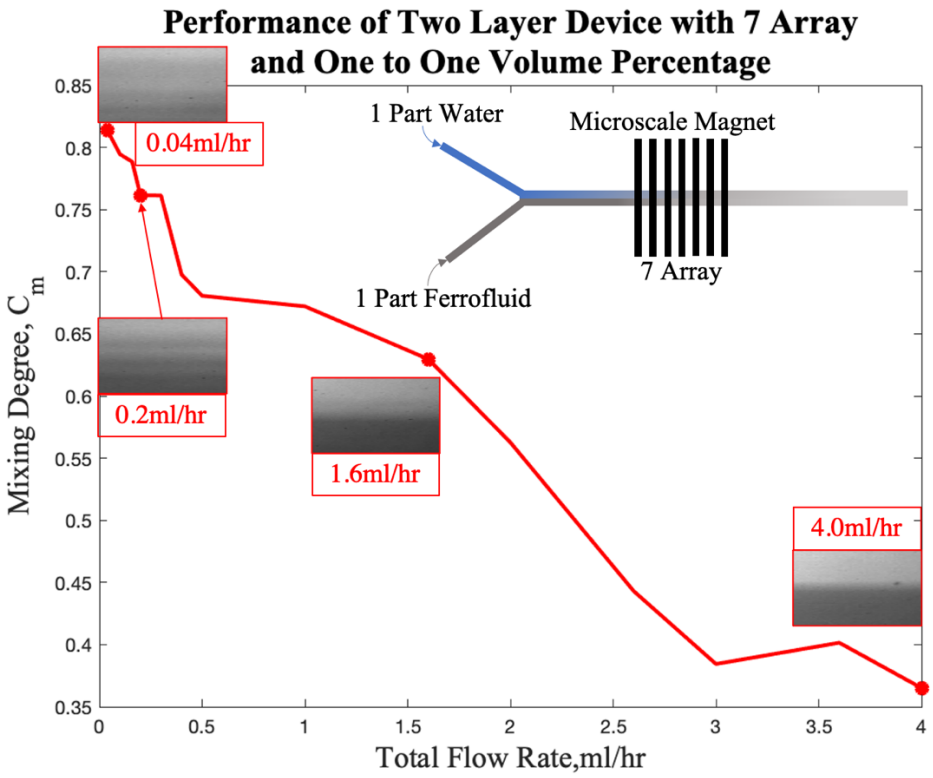

Figure 41. Graph of mixing performance against the flow rate for 7 array micromagnet for a volume percentage of 1:1 for distilled water to ferrofluid. The top right corner shows a two-dimensional top view of the two-layer device. The images show the ferrofluid and distilled water at the outlet.

4.3.4.4 Discussion

This subsection discusses the relationship between all the cases and comparison of the parameters. To recap, case 1 is the base case with a micromagnet containing 4 bars of magnet, case 2 has a 2:1 volume percentage between distilled water and ferrofluid, while case 3 contains 7 bars of magnet in the micromagnetic array. Table 7 shows the mixing degree for cases 1-2 at flow rates ranging from Q=0.04ml/hr to Q=4.0ml/hr. Figure 42(a) shows the graph of mixing degree against the flow rate for the three different cases.

Table 7. Table of mixing performances for cases 1-3 at different flow rates

	Mixing degree =equation (C_m)		
Flow rates (ml/hr)	**Case 1**	**Case 2**	**Case 3**
0.04	0.7506	0.7684	0.8135
0.1	0.6885	0.6319	0.7945
0.16	0.6602	0.6173	0.7884
0.2	0.6495	0.5239	0.7615
0.3	0.5866	0.4853	0.7613
0.4	0.5281	0.4821	0.6977
0.5	0.5259	0.4851	0.6806
1	0.5143	0.4775	0.6721
1.6	0.5137	0.4709	0.6297
2	0.4808	0.4568	0.5626
2.6	0.4756	0.4414	0.443
3	0.4749	0.4449	0.3844
3.6	0.4627	0.4397	0.4015
4	0.4586	0.4155	0.3651

At the lowest flow rate (Q=0.04ml/hr), case 3 yielded the highest mixing degree, followed by case 2 and then case 1. Case 3 had the highest flow rate because of the array of 7 magnetic bars, which impart a higher accumulated magnetic force on the ferrofluid nanoparticles. This allows the ferrofluid nanoparticles to migrate upward, hence mixing with distilled water. The mixing degree for cases 1 and 2 are similar, which shows that the volume percentage of ferrofluid is not a big factor that affects the mixing degree at a low flow rate. Since the residence time is high at a low flow rate, the particles had enough time to interact the other fluids regardless of volume percentage.

Case 2 contains a volume percentage ratio of 2:1 between the distilled water and ferrofluid, which means only 33.33% was ferrofluid while 66.67% was distilled water. Since the amount of ferrofluid was less than the amount of distilled water, the mixing performance was the least among the three cases. From a flow rate of 0.1ml/hr to 2ml/hr, case 3 had a considerably higher flow rate compared to case 2 and case 1. This shows that the number of magnets in an array has a higher effect on the mixing degree than the volume percentage of ferrofluid in the mixture. However, at a flow rate of Q=2.6ml/hr, the mixing degree of case 3 deteriorated. This is because at a higher flow rate, the number of arrays does not affect mixing degree, since the width of the magnetic

array itself is the same for all the cases. The gap between each magnetic bar is decreased to increase the number of bars in an array, which decreases the residence time between ferrofluid and distilled water.

Figure 42(b) shows the trendlines for the three different cases for mixing of ferrofluid and distilled water. This graph of trendlines was created to show the predicted mixing performance if the flow rate was higher at a range of 0-100ml.hr. The equation of best fit line for case 1 is y=-0.137log(x)+0.8468, case 2 is y=-0.127log(x)+0.7349 and case 3 is y=-0.191log(x)+0.962. Case 2 has the lowest mixing performance until a flow rate of 35ml/hr. Case 3 had the highest performance at lower flow rate but the lowest performance past 35ml/hr.

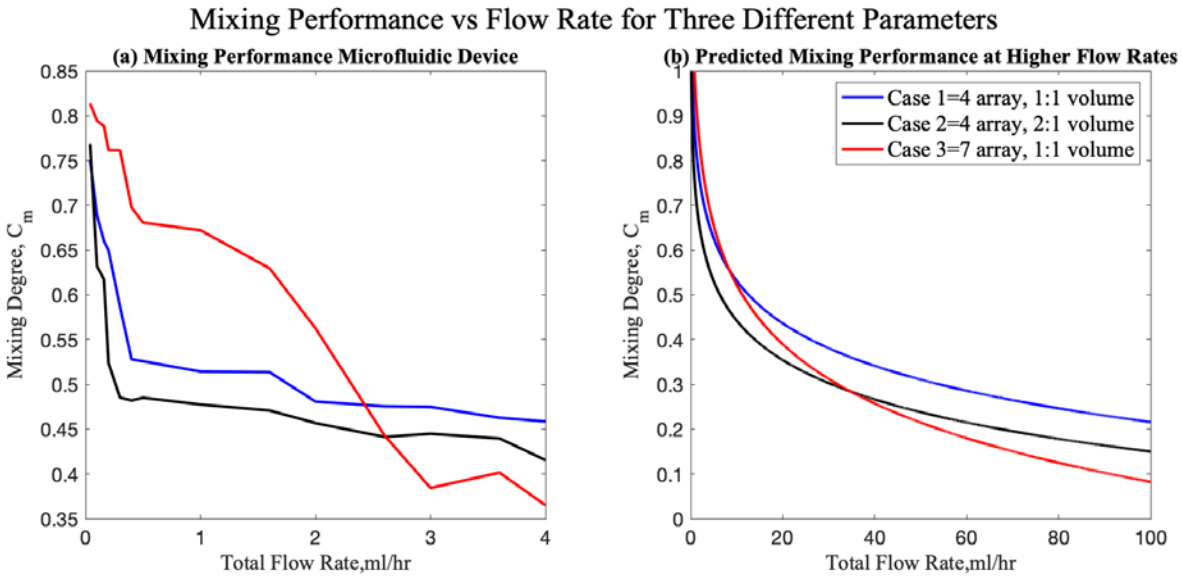

Figure 42. Graphs (a) of comparison and (b) predicted trendline of mixing performance against the flow rate for three different cases with different parametric variations using the two-layer device.

4.4 Separation of Magnetic Microparticles

The goal of this experiment is to first show the deviation of magnetic particles suspended in distilled water. Next, the separation of magnetic microparticles and nonmagnetic particles is discussed. Separation of particles in microfluidics can be applied in DNA processes, parallel genetic analysis and disease diagnosis. Similar to the mixing phenomenon on a microscale, particles that are suspended in a fluid in a microfluidic channel, i.e. blood vessels, tend to follow their laminar flow path because of the laminar flow regime in microchannels. The fabrication

method in this application was discussed in Section 2.3.1. which was also repeated for the application in Section 4.2. The single layer of microfluidic chip was bonded to a glass slide, which enables it to withstand high pressure inside the microchannel. The microscale permanent magnet generates a magnetic field, which when coupled with the rectangular shape, induces a large magnetic gradient. Hence, the magnetic microparticles deviated from their laminar flow path as a result of the force imparted onto the particles.

4.4.1 Deviation of the Magnetic Microparticles Suspended in Distilled Water

4.4.1.1 Work concept

Figure 43 shows the dimensions of the microfluidic device. The length of the microchannel and the micromagnet are L=2cm and the width of the microchannel is w=150 µm. The closest distance between the micromagnet and the microchannel is g=150 µm, the width of the rectangles in the magnet is w_m=500 µm and the height of the rectangles is h_m=1000 µm. The distance between the rectangular structures is w_g=500 µm and the width of the microbar (structure that connects all the rectangular structures) is j=500 µm. The depth of all the structures is d=35 µm, since the thickness of the photoresist film is 35 µm. The microchannel consists of two inlets and one outlet, where magnetic microparticles are injected into the top inlet and distilled water is injected into the bottom inlet. This configuration is the best because the magnet is located near the lower part of the device, hence pumping the particles into the top inlet shows the migration and of the microparticles. The microscale magnet has protruding rectangular microstructures because this shape generates large magnetic gradients near the corners of the rectangles.

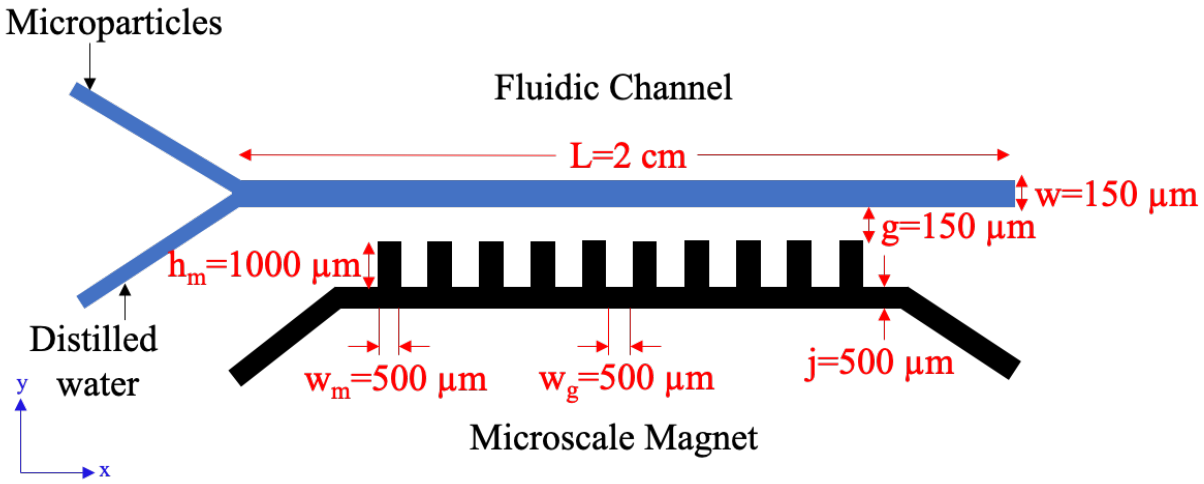

Figure 43. Top view of the microfluidic device. Magnetic microparticles are injected into the top inlet and distilled water is injected into the bottom inlet.

The forces acting on the magnetic microparticles are magnetic ($\mathbf{F}_m$), buoyancy ($\mathbf{F}_b$), gravitational ($\mathbf{F}_g$), and drag ($\mathbf{F}_d$), force. First, magnetic force, $\mathbf{F}_m$, that acts on the microparticles is [53]

$$F_m = \mu_0(m_p \cdot \nabla)H \tag{9}$$

where $\mathbf{m}_p = \mathbf{M}_p V_p$ is the dipole moment of the particle, where $\mathbf{M}_p$ is the field-dependent particle magnetization and V_p is the volume of the microparticle. After some simplification and specification of the problem, magnetic force on the microparticles is

$$F_m = \mu_0 V_p \frac{3\chi_p}{\chi_p+3}(H \cdot \nabla)H \tag{10}$$

where χ_p is the magnetic susceptibility of the microparticle. The drag force acting on the particles is derived from Stoke's law for low Reynolds number [54],

$$F_d = 6\pi\eta r(u_f - u_p)f_D \tag{11}$$

where η is the dynamic viscosity of the fluid, r is the radius of the microparticle, $\mathbf{u}_f$ is the velocity of the fluid, $\mathbf{u}_p$ is the velocity of the particle and f_D is the hydrodynamic drag force coefficient. The difference between the Stokes law and equation (9) is the presence of f_D, which takes the effects imposed by the walls of the channel into account. It is expressed by [55],

$$f_D = [1 - \frac{9}{16}\left(\frac{r}{r+d'}\right) + \frac{1}{8}\left(\frac{r}{r+d'}\right)^3 - \frac{45}{256}\left(\frac{r}{r+d'}\right)^4 - \frac{1}{16}\left(\frac{r}{r+d'}\right)^5]^{-1} \tag{12}$$

where d′ is the distance between the wall of the channel and the bottom surface of the microparticle. Buoyant force, $\mathbf{F}_b$, experienced by the microparticles is given by [[56]]

$$F_b = \frac{1}{2\mu_0}\Delta\chi V_p \nabla B^2 \tag{13}$$

where $\Delta\chi = \chi_p - \chi_f$ is the difference in magnetic susceptibilities between the magnetic microparticle (χ_p) and surrounding fluid (χ_f). Lastly, gravitational force, $\mathbf{F}_g$, although it is miniscule, can be represented as follows [57],

$$F_g = V_p(\rho_p - \rho_f)g \tag{14}$$

where ρ_p is the density of the particle, ρ_f is the density of the fluid and **g** is the gravitational acceleration. Figure 44 shows a schematic of the flow path of the magnetic particles with and without the presence of a magnetic field.

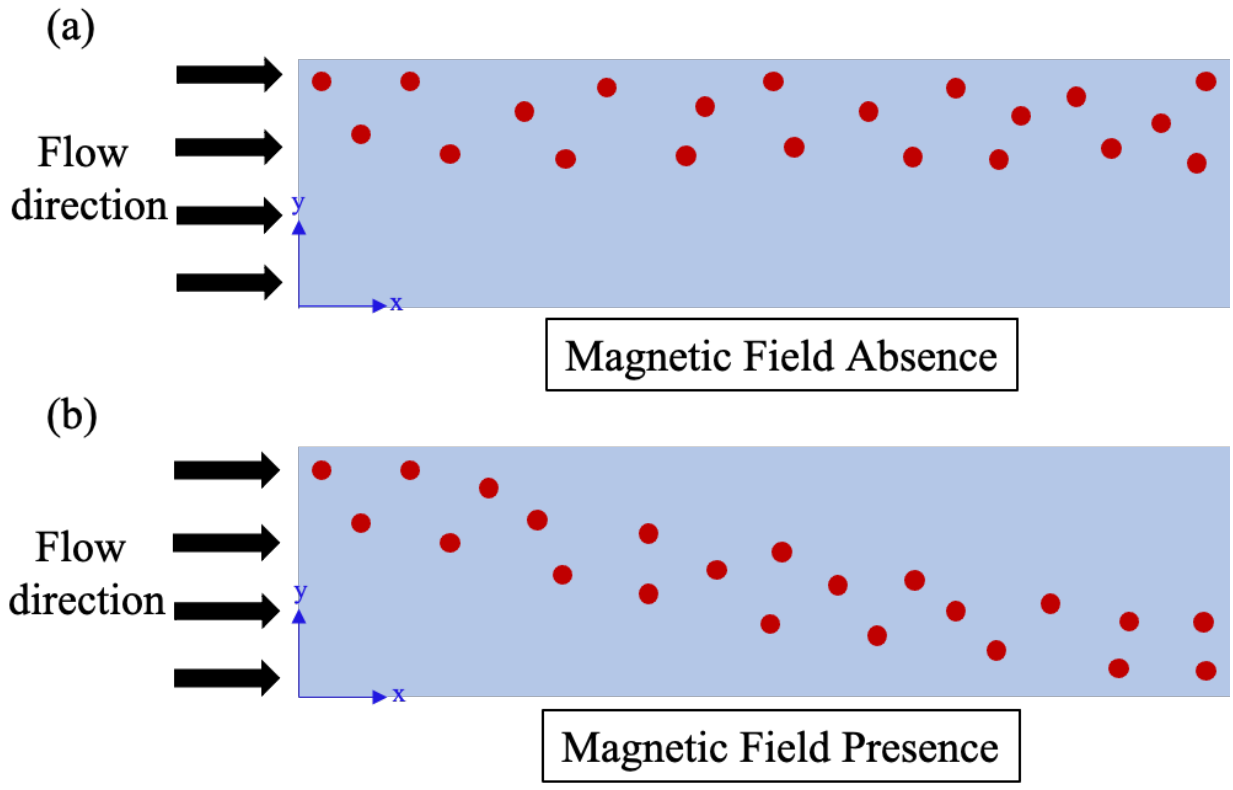

Figure 44. Flow path of magnetic particles, which are shown in red color in the (a) absence and (b) presence of a magnetic field

4.4.1.2 Experimental Setup and Materials

A clean 1mL syringe was used to extract 0.2 mL of magnetic particles (Magsphere, Pasadena, CA, USA) from the original solution. The particles were moved to Vial 1. In a cup, distilled water was prepared by adding Tween 20 (Tween 20 (=Polyoxyethylene Sorbitan Monolaurate), TCI Chemicals, Tokyo, Japan), which is a particle lubricant that prevents particles from sticking to each other. 0.8 mL of prepared distilled water was added to Vial 1 to create a solution that was diluted 5 times. 0.1mL of diluted sample from Vial 1 was transferred to Vial 2. 0.9 mL of prepared distilled water was added to Vial 2 to create a solution that was diluted 50 times. 0.1mL of diluted sample from Vial 2 was transferred to Vial 3. 0.9 mL of prepared distilled water was added to Vial 3 to create a solution that was diluted 500 times. Figure 45 shows the preparation of the magnetic particle solution clearly. Samples from Vial 3 was taken for this experiment because the particles can be seen clearly under the microscope and the particles have a lower tendency of clumping together.

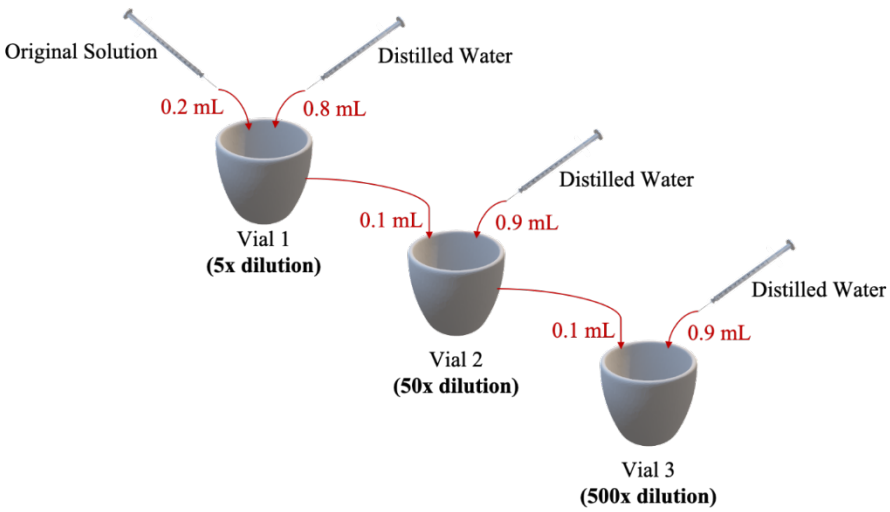

Figure 45. Dilution steps to generate a 500x diluted magnetic particle solution. Vial 1 contains a solution diluted 5 times, vial 2 contains a solution diluted 50 times and vial 3 contains a solution diluted 500 times.

Two 1 mL syringes were filled with magnetic particles and prepared distilled water, respectively. The experimental setup for this experiment is shown in Figure 30 and the procedures are similar to the procedure described in Section 4.2.3. The syringe containing magnetic microparticles was connected to the top inlet while the syringe containing prepared distilled water

was connected to the bottom inlet. The frame rate of the high-speed camera was increased to capture the movements of the magnetic particles. Particles' motion on a micro scale is very fast because of the small channel width and particle size. In order to observe and process the data output from the high-speed camera, the frame rate needs to be high. A higher frame rate means that the camera takes more pictures (frames) in a given time, which means that a slow-motion video can be obtained, and the position of the particles can be seen clearly.

4.4.1.3 Results and discussion

Figure 46 shows the labels on the microchannel to better understand the results in this section. The upper wall is located at y=60µm, the midline is at y=0µm and the lower wall is located at y=-60µm. The magnetic particles were injected into the upper inlet and the goal for the particles was to deviate towards the lower wall where the magnet was located. The closer the particles moved to y=-60µm, the better the deviation performance. Figure 47 shows the vertical location of the magnetic particles against the respective flow rates. The magnetic particles moved towards the lower wall when the flow rate was small. Similar to the mixing phenomenon, in particle manipulation, residence time is a big factor to determine the separation efficiency of a device. The residence time is long at a flow rate of 0.02ml/hr, which gave the magnetic field sufficient time to impart a strong magnetic force on the magnetic particles. Hence, the deviation observed at this flow rate was the highest at -45.8µm.

At a flow rate of 1.5ml/hr, the magnetic particles were located at y=0µm. Since 0µm is the midline of the fluidic channel, the deviation of the particles that travelled to the midline are not desirable. In the application of this separation system, there will be two outlets to collect the magnetic and nonmagnetic particles respectively. If the magnetic particles stayed at the midline, there is a high tendency that the particles will flow into the wrong outlet and decrease the performance of the device. At the highest flow rate of 2ml/hr, the y-location of the magnetic particles was 3.125µm, which is above the midline. This means that the magnetic particles will travel into into the wrong outlet, which is undesirable. The experimental images clearly show the difference in positions of particles at the inlet and the outlet of different flow rates.

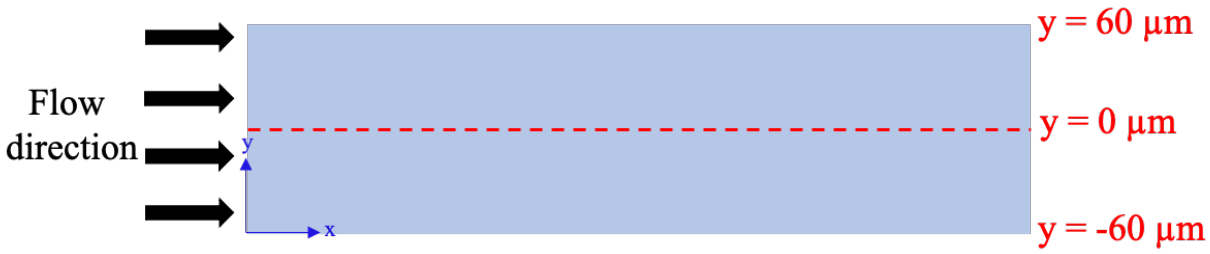

Figure 46. Labels on the microchannel to show the flow field and the vertical positions.

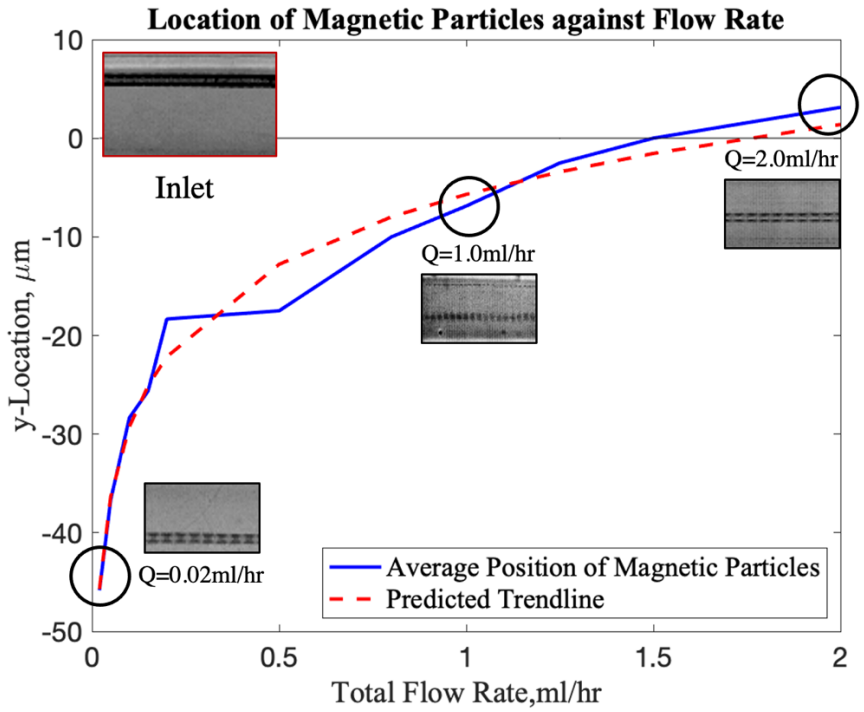

Figure 47. Vertical locations of magnetic particles at the outlet for different flow rates.

4.4.2 Separation of Magnetic and Nonmagnetic Particles

4.4.2.1 Work concept

The microfluidic chip in this experiment is the same as the chip in the deviation experiment. In this experiment, both magnetic and nonmagnetic particles were injected into the top inlet of the microfluidic device and distilled water was injected into the bottom inlet. Since there were two types of particles, the forces acting on the particles are different. Both particles have a diameter of 12 µm. The forces acting on the magnetic particles are magnetic, drag, buoyant and gravitational forces, which are the same as discussed in Section 4.4.1.1. The forces acting on the nonmagnetic

particles are only drag, buoyant and gravitational forces. The equations to calculate the forces are shown in Equations 9-14. Figure 48(a) shows the forces acting on a magnetic particle and Figure 48(b) shows the forces acting on a nonmagnetic particle. Figure 48(c) shows the expected flow path of both particles in the presence of a magnetic field.

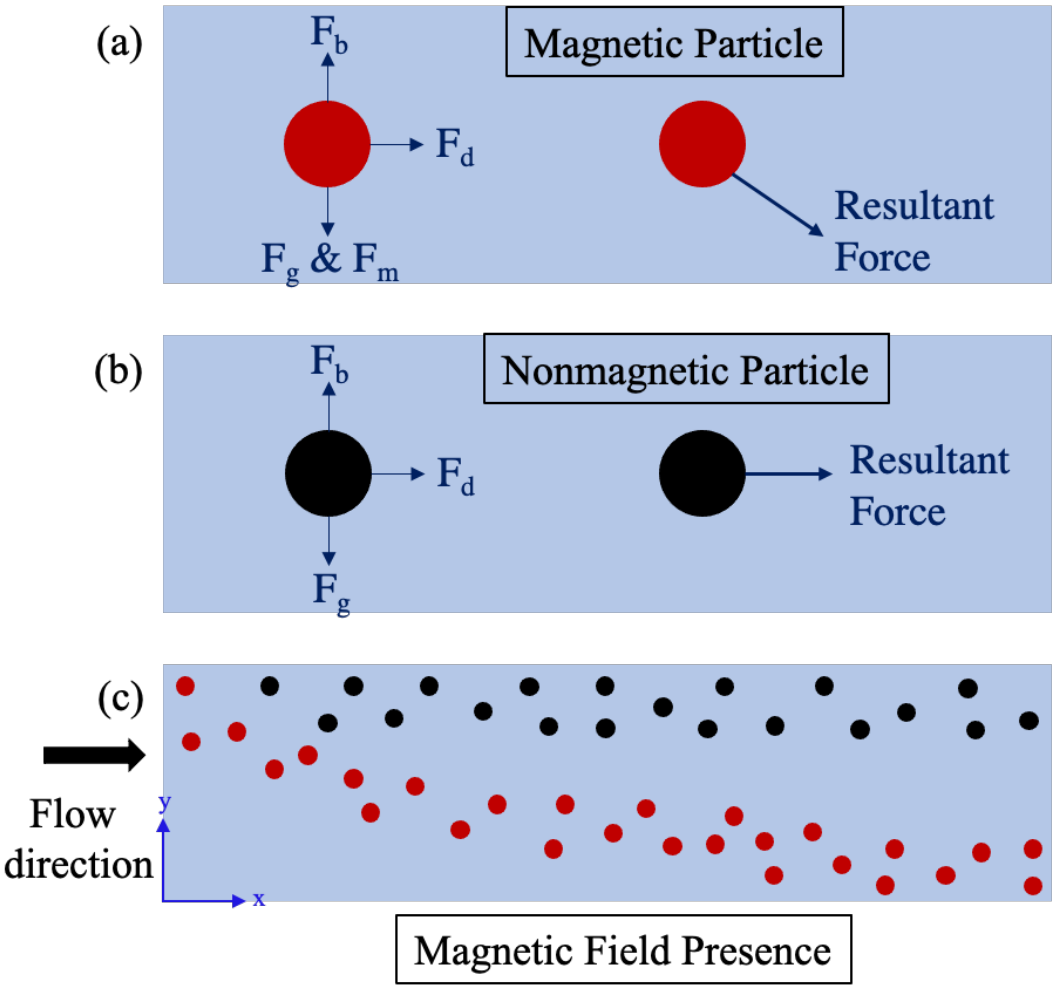

Figure 48. (a) Forces acting on magnetic particles. (b) Forces acting on nonmagnetic particles. (c) Flow paths of magnetic and nonmagnetic particles in the presence of a magnetic field.

4.4.2.2 Setup and materials

0.1 mL of magnetic particles were extracted from the original solution with a clean 1mL syringe. The particles were moved to Vial 1. 0.1 mL of nonmagnetic particles (Magsphere, Pasadena, CA, USA) were extracted from the original solution and also moved to Vial 1 with a clean 1mL syringe. In a cup, distilled water was prepared by adding Tween 20, which is a particle

lubricant that prevents particles from sticking to each other. 0.8 mL of prepared distilled water was added to Vial 1 to create a solution that was diluted 5 times. 0.1mL of diluted sample from Vial 1 was transferred to Vial 2. 0.9 mL of prepared distilled water was added to Vial 2 to create a solution that was diluted 50 times. 0.1mL of diluted sample from Vial 2 was transferred to Vial 3. 0.9 mL of prepared distilled water was added to Vial 3 to create a solution that was diluted 500 times. Samples from Vial 3 were taken in this experiment because the particles can be seen clearly under the microscope and the particles have a lower tendency of clumping together. Figure 49 shows the preparation of the magnetic and nonmagnetic particle solution clearly.

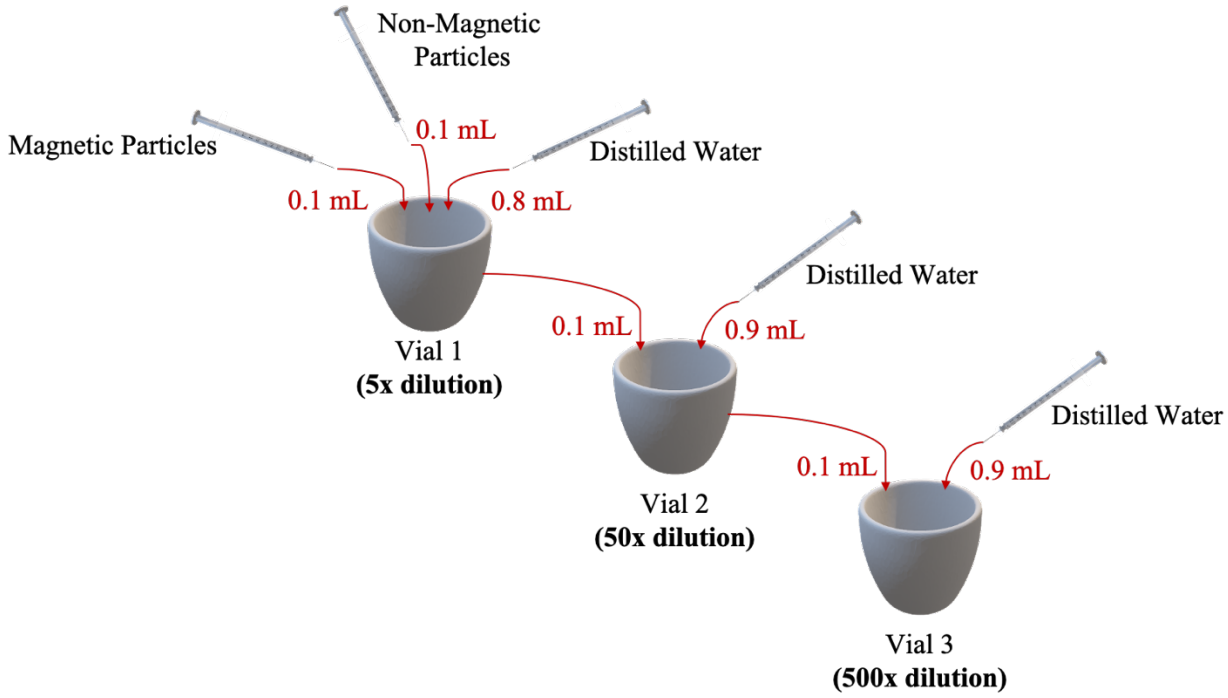

Figure 49. Dilution steps to generate a 500x diluted magnetic particle solution. Vial 1 contains a solution diluted five times, vial 2 contains a solution diluted 50 times and vial 3 contains a solution diluted 500 times.

Two 1 mL syringes were filled with the sample from Vial 3 and prepared distilled water, respectively. The experimental setup for this experiment is shown in Figure 30 and the procedures are similar to the procedure described in Section 4.2.3. The syringe containing the microparticles was connected to the top inlet while the syringe containing prepared distilled water was connected to the bottom inlet. Similar to Section 4.4.1.2., the frame rate of the high-speed camera was increased to capture the movements of the magnetic and nonmagnetic microparticles.

4.4.2.3 Results and Discussion

Figure 50 shows the vertical location, y, of the magnetic and nonmagnetic particles against the respective flow rate. The goal is for the magnetic particles to move towards the lower half of the channel while the nonmagnetic particles need to maintain their location at the upper half of the channel. This experiment ultimately shows the capability of this device to separate magnetic particles from a pool of magnetic and nonmagnetic particles. In this experiment, the residence time was yet again an important factor in determining the mixing performance of the device. It is evident that the nonmagnetic particles are not affected by the magnetic field, since all of the nonmagnetic particles stayed at the top half of the channel. The location of the magnetic and nonmagnetic particles at a flow rate of Q=0.02ml/hr were y=-50.01µm and y=17.5µm, respectively. There was a significant distance between the magnetic and nonmagnetic particles. At a flow rate of Q=0.8ml/hr, the magnetic particles were located at y=-21.27µm while the nonmagnetic particles were located at y=40µm. All the flow rates up to Q=1.25ml/hr show a significant difference between the location of the magnetic and nonmagnetic particles.

At the highest flow rate of Q=2.0ml/hr, the y-location of the magnetic particles was y=1.24µm, while the nonmagnetic particles were located at y=36.345µm, both of which were above the midline. This means that the magnetic particles will go into the wrong outlet, which is undesirable. Similar to the deviation experiment, at flow rates of Q=1.5-2.0ml/hr, the magnetic particles were located close to the midline, which leads to a lower separation performance. As mentioned before, this is due to the lower residence time that each particle spends interacting with the microscale magnet. According to equations 9 and 10, the magnetic force, F_m imparted on the magnetic particles cause the motion of the magnetic particles towards the microscale magnet. A lower residence time allows for a higher F_d while a higher residence time allows higher F_m. At a lower flow rate, the residence time is higher, hence the magnetic force acting on the magnetic particles are higher, causing the magnetic particles to deviate towards to micromagnet, hence separating themselves from the nonmagnetic particles.

Table 8. Vertical locations of magnetic and nonmagnetic particles at different flow rates

Flow Rate, Q (ml/hr)	Vertical location of magnetic particles, μm	Vertical location of nonmagnetic particles, μm
0.02	-50.01	17.495
0.05	-25.6325	51.2425
0.1	-24.1675	28.3325
0.2	-22.5025	35.825
0.5	-21.6675	25
0.8	-21.27	40
1	-20.8475	40.7825
1.25	-16.2525	37.5
1.5	-2.5025	32.4825
1.75	0	45
2	1.24	36.345

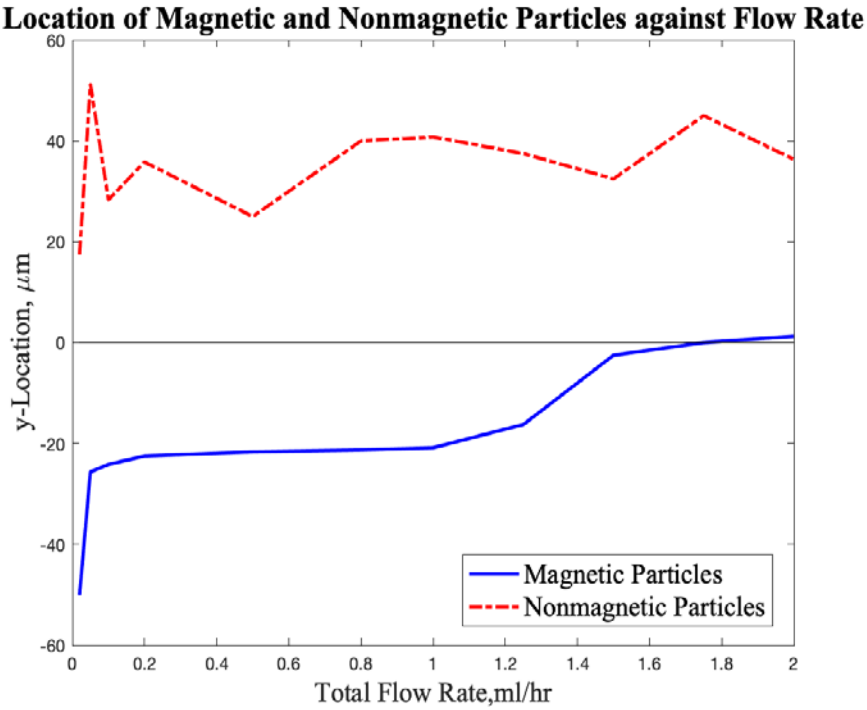

Figure 50. Vertical locations of magnetic and nonmagnetic particles at microchannel outlet for different flow rates.

5. CONCLUSION

A low-cost fabrication platform was developed to decrease the cost of manufacture for microfluidic devices. This work has presented the fabrication process, evaluation of the fabrication performance and the applications of the fabrication system. A high-resolution and high-throughput microfluidic device was fabricated for mixing of ferrofluid and separation of magnetic and nonmagnetic particles. A systematic experimental study was conducted to determine the performance of the fabricated device by analyzing the pixel intensity at the outlet for mixing and the degree of deviation for separation of particles.

Chapter 1 introduced the readers to previous works in the field and how the present work presents a novelty and advantage over similar devices. In chapter 2, the developed soft-lithography fabrication process was discussed, which included detailed steps and the reasoning behind the choice of materials and steps. First, a master mold comprising a copper plate and negative photoresist film was developed in a sodium carbonate solution. For the single layer device, PDMS was casted onto the master mold, cured and then bonded to a glass slide. Then a mixture of PDMS-NdFeB was injected into the microstructure, cured and magnetized to activate the microscale magnet. For the two-layer device, two layers of PDMS were casted onto two different master molds, where one is of the microchannel and the other is of the microstructure for the magnetic array. The microstructure layer was partially bonded to a glass slide and filled with a mixture of PDMS-NdFeB, cured and magnetized to activate the magnetic array. The magnetic layer was peeled away from the glass slide and bonded coincident under the microchannel layer.

Chapter 3 explored the performance of the fabrication system by evaluating the device with three methods: using an SEM on the master mold, observing the PDMS microfluidic device under the light microscope and testing the light intensity. For the master mold, the effect of exposure times and development times on the quality of the photoresist film was tested. An exposure time of 25 seconds and a development time of 60 seconds was found to be the best combination that provided high quality master mold. Next, important structures (i.e. sharp corners and channels that are close together) were observed under the light microscope for any discrepancies to assess the performance of the PDMS. Finally, the light source platform was evaluated by running an intensity and uniformity test at different heights from the exposure platform.

Finally, chapter 4 introduced the applications of the in-house fabricated microfluidic device by conducting mixing and separation experiments. The first experiment was mixing of ferrofluid and distilled water in a one-layer microfluidic device, where three parameters, the presence of a magnet, the shape of the magnet and the volume percentage of ferrofluid were varied. The magnetic field gradient generated by the microscale magnet with rectangular structures was stronger than that of only a magnetic bar. The mixing performance was evaluated by analyzing the mixing degree by calculating the pixel intensity at different streamwise location of the microfluidic channel. As the flow rate increased, the mixing degree decreased due to the lower residence time between the fluids. The results of this experiment showed the device containing a micromagnet with rectangular structures yielded the highest mixing degree with a homogenized mixture.

The second experiment was the mixing of ferrofluid and distilled water on a two-layer device, where the number of magnets in an array and the volume percentage of ferrofluid used for mixing were varied. The mixing degree was evaluated by analyzing the pixel intensity, similar to the embedded magnet experiment. It was found that as the flow rate increased, the mixing degree decreased for all the parameters. The microfluidic device that contained 7 magnetic bars in an array provided the highest mixing degree because the combined magnetic field gradient was higher. The mixing degree decreased significantly at higher flow rates for case 3 because of the lower residence time of the fluids, which decreased the force imparted by the micromagnet on the nanoparticles, thus decreasing the motion of the nanoparticles.

The third and fourth experiments were deviation of magnetic particles and separation of magnetic and nonmagnetic particles using embedded microscale magnet, respectively. The third experiment was conducted to show the deviation of the magnetic particles, where the performance of the device was evaluated by analyzing the location of the magnetic particles near the outlet. The magnetic particles deviated well at lower flow rates, where the particles deviated to a lowest location of y = -45.8μm, but at a flow rate of Q=1.5ml/hr, the location of magnetic particles near the outlet was at y = 0μm. For flow rates higher than 1.5ml/hr, the magnetic particles stayed in the upper half of the channel. The final experiment was conducted to show the separation of magnetic and nonmagnetic particles. As the flow rate increased, the location of the magnetic particles at the outlet shifted away from the lower wall. The magnetic particles moved to the bottom half of the channel while the nonmagnetic particles stayed at the upper half of the channel. This is due to the magnetic force imparted on the magnetic particles, which is not experienced by the nonmagnetic

particles. The magnetic particles were deviated away from their laminar flow paths because of the strong magnetic force generated by a high magnetic field gradient, which was higher that the drag force.

This work is beneficial for applications in the biomedical and biochemical engineering sector because the usage of a microscale magnet provides a smaller footprint and does not harm biological particles while having a high-throughput and performance. A simple and low-cost microfluidic device is desirable to conduct more research that can be applied in critical areas. Chemical synthesis and analysis in the food industry can be facilitated by having a high throughput and efficient device such as the ones that are fabricated in this work. Separation of particles using magnetic field is useful in detecting and sorting cancer causing cells.

REFERENCES

[1] Nguyen, N., Wereley, S.T., & Shaegh, S. (2019) *Fundamentals and Applications of Microfluidics*. Norwood, MA: Artech House

[2] Lin, B. (2013) *Microfluidics Technologies and Applications*. Berlin: Springer Berlin.

[3] Zhang, Y., & Ozdemir, P. (2009) Microfluidic DNA Amplification—A Review. *Analytica Chimica Acta,* 638(2), 115–25. doi:10.1016/j.aca.2009.02.038.

[4] Dittrich, P., & Manz, A. (2006) Lab-on-a-Chip: Microfluidics in Drug Discovery. *Nature Reviews Drug Discovery* 5(3): 210–18. doi:10.1038/nrd1985.

[5] Krupenkin, T. (2011). *U.S. Patent No. US7898096B1*. Washington, DC: U.S. Patent and Trademark Office.

[6] Parikesit, G., Prasetia, F., Pribadi, G. A., Simbolon, D. C., Pradhana, G. Y., Prastowo, A. R., Gunawan, A., Suryopratomo, K., & Kusumaningtyas, I. (2012) Textile-Based Microfluidics: Modulated Wetting, Mixing, Sorting, and Energy Harvesting. *Journal of the Textile Institute* 103(10): 1077–87. doi:10.1080/00405000.2012.660756.

[7] Schiphorst, J., Saez, J., Diamond, D., Benito-Lopez, F., & Schenning, A. (2018) Light-Responsive Polymers for Microfluidic Applications. *Lab on a Chip* 18(5): 699–709. doi:10.1039/c7lc01297g.

[8] Zhang, X, Li, L., & Luo, C. (2016) Gel Integration for Microfluidic Applications. *Lab on a Chip* 16(10): 1757–76. doi:10.1039/c6lc00247a.

[9] Lee, C., Wang, W-T, Liu, C-C, & Fu, L-M. (2016) Passive Mixers in Microfluidic Systems: A Review. *Chemical Engineering Journal* 288: 146–60. doi:10.1016/j.cej.2015.10.122.

[10] Hartvig, N., Farquharson, G., Mielke, R., Varney, M., & Foster, M. (2011) Sampling Plan for Cleanroom Classification with Respect to Airborne Particles. *Journal of the IEST* 54(1): 1–15. doi:10.17764/jiet.54.1.x034466930341406.

[11] Yang, L., & Gan C.E. (2007) Costing Small Cleanrooms. *Building and Environment* 42(2): 743–51. doi:10.1016/j.buildenv.2005.09.010.

[12] Gale, B., Jafek, A., Lambert, C., Goenner, B., Moghimifam, H., Nze, U., & Kamarapu, S. (2018) A Review of Current Methods in Microfluidic Device Fabrication and Future Commercialization Prospects. *Inventions* 3(3): 60. doi:10.3390/inventions3030060.

[13] Ontiveros, F., & McDowell, R. (2016) “Ultra-Thin Microfluidic Devices Built via Thermal Lamination.” *Proceedings of the ASME 14th International Conference on Nanochannels, Microchannels, and Minichannels*. New York, NY: The American Society of Mechanical Engineers.

[14] Giboz, J., Copponnex, T., & Mélé, P. Microinjection Molding of Thermoplastic Polymers: a Review. (2007) *Journal of Micromechanics and Microengineering* 17(6). doi:10.1088/0960-1317/17/6/r02.

[15] Kumuditha, W., O'neil, C. E., Uba, F. I., & Soper, S. A. (2017) Thermoplastic Nanofluidic Devices for Biomedical Applications. *Lab on a Chip* 17(3): 362–81. doi:10.1039/c6lc01173j.

[16] Grosse, A., Grewe, M., & Fouckhardt, H. (2001) Deep Wet Etching of Fused Silica Glass for Hollow Capillary Optical Leaky Waveguides in Microfluidic Devices. *Journal of Micromechanics and Microengineering* 11(3): 257–62. doi:10.1088/0960-1317/11/3/315.

[17] Garra, J., Long, T., Currie, J., Schneider, T., White, R., & Paranjape, M. (2002) Dry Etching of Polydimethylsiloxane for Microfluidic Systems. *Journal of Vacuum Science & Technology A: Vacuum, Surfaces, and Films* 20(3): 975–82. doi:10.1116/1.1460896.

[18] Tumbleston, J. R., Shirvanyants, D., Ermoshkin, N., Janusziewicz, R., Johnson, A. R., Kelly, D., Chen, K., et al. (2015) Continuous Liquid Interface Production of 3D Objects. *Science* 347(6225): 1349–52. doi:10.1126/science.aaa2397.

[19] Paydar, O. H., Paredes, C. N., Hwang, Y., Paz, J., Shas, N. B. & Candler, R. N. (2014) Characterization of 3D-Printed Microfluidic Chip Interconnects with Integrated O-Rings.” *Sensors and Actuators A: Physical* 205: 199–203. doi:10.1016/j.sna.2013.11.005.

[20] Revzin, A., Russell, R. J., Yadavelli, V. K. Koh, W-G, Deister, C. Hile, D. D., Mellott, M. B., & Pishko, M. V. (2001) Fabrication of Poly(Ethylene Glycol) Hydrogel Microstructures Using Photolithography. *Langmuir* 17(18): 5440–47. doi:10.1021/la010075w.

[21] Zhang, F., Fu, Y., & Yu, X-Y. (2018) Microfluidics and Interfacial Chemistry in the Atmosphere. *Physical Chemistry of Gas-Liquid Interfaces*: 245–70. doi:10.1016/b978-0-12-813641-6.00009-1.

[22] Lee, C. Y., & Fu, L.-M. (2018) Recent Advances and Applications of Micromixers. *Sensors and Actuators B: Chemical* 259: 677–702. doi:10.1016/j.snb.2017.12.034.

[23] Yang, J., Qi, L., Chen, Y., & Ma, H. (2012) Design and Fabrication of a Three-Dimensional Spiral Micromixer. *Chinese Journal of Chemistry* 31(2): 209–14. doi:10.1002/cjoc.201200922.

[24] Clark, J., Klaufman, M., & Fodor, P. S. (2018) Mixing Enhancement in Serpentine Micromixers with a Non-Rectangular Cross-Section. *Micromachines* 9(3): 107. doi:.3390/mi9030107.

[25] Lynn, N. S., Henry, C. S., & Dandy, D. S. (2008) Microfluidic Mixing via Transverse Electrokinetic Effects in a Planar Microchannel. *Microfluidics and Nanofluidics* 5(4): 493-505. doi:10.1007/s10404-008-0258-8.

[26] Chen, C.-K., Cho, & C.-C. (2008) Electrokinetically Driven Flow Mixing Utilizing Chaotic Electric Fields. *Microfluidics and Nanofluidics* 5(6): 785–93. doi:10.1007/s10404-008-0286-4.

[27] Yeo, L. Y., & Friend, J. R. (2009) Ultrafast Microfluidics Using Surface Acoustic Waves. *Biomicrofluidics* 3(1): 012002. doi:10.1063/1.3056040.

[28] Ahmed, D., Mao, X., Juluri, B. K., & Huang, T. J. (2009) A Fast Microfluidic Mixer Based on Acoustically Driven Sidewall-Trapped Microbubbles. *Microfluidics and Nanofluidics* 7(5): 727–31. doi:10.1007/s10404-009-0444-3.

[29] Kunti, G., Bhattacharya, A. & Chakraborty, S. (2017) Rapid Mixing with High-Throughput in a Semi-Active Semi-Passive Micromixer. *Electrophoresis* 38(9-10): 1310-1317. doi:10.1002/elps.201600393.

[30] Ajarostaghi, S., Delavar, M. A., & Poncet, S. (2019) Thermal Mixing, Cooling and Entropy Generation in a Micromixer with a Porous Zone by the Lattice Boltzmann Method. *Journal of Thermal Analysis and Calorimetry* 140(3): 1321–1339. doi:10.1007/s10973-019-08386-3.

[31] Ballard, M., Owen, D., Mills, Z. G., Hesketh, P. J., & Alexeev, A. (2016) Orbiting Magnetic Microbeads Enable Rapid Microfluidic Mixing. *Microfluidics and Nanofluidics* 20(6). https://doi.org/10.1007/s10404-016-1750-1.

[32] Nouri, D., Zabihi-Hesari, A. & Passandideh-Fard, M. (2017) Rapid Mixing in Micromixers Using Magnetic Field. *Sensors and Actuators A: Physical* 255: 79–86. doi:10.1016/j.sna.2017.01.005.

[33] Maleki, M. A., Soltani, M., Kashaninejad, N., & Nguyen, N-T. (2019) Effects of Magnetic Nanoparticles on Mixing in Droplet-Based Microfluidics. *Physics of Fluids* 31(3): 032001. doi:10.1063/1.5086867.

[34] Owen, D., Ballard, M., Alexeev, A., & Hesketh, P. J. (2016) Rapid Microfluidic Mixing via Rotating Magnetic Microbeads. *Sensors and Actuators A: Physical* 251: 84–91. doi:10.1016/j.sna.2016.09.040.

[35] Hejazian, M., & Nguyen, N-T. (2017) A Rapid Magnetofluidic Micromixer Using Diluted Ferrofluid. *Micromachines* 8(2): 37. doi:10.3390/mi8020037.

[36] Fuentes, C., Kang, I., Lee, J., Song, D., Sjöö, M., Choi, J., Lee, S., & Nilsson, L. (2019) Fractionation and Characterization of Starch Granules Using Field-Flow Fractionation (FFF) and Differential Scanning Calorimetry (DSC). *Analytical and Bioanalytical Chemistry* 411(6): 3665–74. doi:10.1007/s00216-019-01852-9.

[37] Yang, J. S., Lee, J. C., Byeon, S. K., Rha, K. H., & Moon, M. H. (2017) Size Dependent Lipidomic Analysis of Urinary Exosomes from Patients with Prostate Cancer by Flow Field-Flow Fractionation and Nanoflow Liquid Chromatography-Tandem Mass Spectrometry. *Analytical Chemistry* 89(4): 2488–96. doi:10.1021/acs.analchem.6b04634.

[38] Kabacaoğlu, G., & Biros, G. (2018) Sorting Same-Size Red Blood Cells in Deep Deterministic Lateral Displacement Devices. *Journal of Fluid Mechanics* 859: 433–75. doi:10.1017/jfm.2018.829.

[39] Kye, H. G., Park, B. S., Lee, J. M., Song, M. G., Song, H. G., Ahrberg, C. D., & Chung, B. G. (2019). Dual-neodymium magnet-based microfluidic separation device. *Scientific Reports, 9*(1). doi:10.1038/s41598-019-45929-y

[40] Zhou, R., Bai, F., & Wang, C. (2017) Magnetic Separation of Microparticles by Shape. *Lab on a Chip* 17(3): 401–6. doi:10.1039/c6lc01382a.

[41] Ge, L., Wang, S., Ge, S., Yu, J., Yan, M., Li, N., & Huang, J. Electrophoretic Separation in a Microfluidic Paper-Based Analytical Device with an on-Column Wireless Electrogenerated Chemiluminescence Detector. *Chemical Communications* 50(43): 5699. doi:10.1039/c3cc49770d.

[42] Wu, M., Ouyang, Y., Wang, Z., Zhang, R., Huang, P-H., Chen, C., Li, H., et al. (2017) Isolation of Exosomes from Whole Blood by Integrating Acoustics and Microfluidics. *Proceedings of the National Academy of Sciences* 114(40): 10584–89. doi:10.1073/pnas.1709210114.

[43] Vulto, P., Glade, N., Altomare, L., Bablet, J., Tin, L. D., Medoro, I. G., Chartier, N. M., Tartagni, M., & Guerrieri, R. (2005) Microfluidic Channel Fabrication in Dry Film Resist for Production and Prototyping of Hybrid Chips. *Lab on a Chip* 5(2): 158. doi:10.1039/b411885e.

[44] Riston® MultiMaster Series Dry Film Photoresist: Dupont Electronic Solutions. (2020) Retrieved on July 28, 2020, from https://www.dupont.com/products/riston-multimaster-dry-film-photoresist.html.

[45] SYLGARD™ 184 Silicone Elastomer Kit.: Dow Chemical Inc. (2020). Retrieved on July 28, 2020, from https://www.dow.com/en-us/pdp.sylgard-184-silicone-elastomer-kit.01064291z.html.

[46] Huang, J., Dahlgren, D. A., & Hemminger, J. C. (1994) Photopatterning of Self-Assembled Alkanethiolate Monolayers on Gold: A Simple Monolayer Photoresist Utilizing Aqueous Chemistry. *Langmuir* 10(3): 626–28. doi:10.1021/la00015a005.

[47] Shin, J. Y., Soo, J. K., Do, K. K., Dong, H. K. (2015) Fundamental Characteristics of Deep-UV Light-Emitting Diodes and Their Application to Control Foodborne Pathogens. *Applied and Environmental Microbiology* 82(1): 2–10. doi:10.1128/aem.01186-15.

[48] Nouri, D., Zabihi-Hesari, A., & Passandideh-Fard, M. (2017) Rapid Mixing in Micromixers Using Magnetic Field. *Sensors and Actuators A: Physical* 255: 79–86. doi:10.1016/j.sna.2017.01.005.

[49] Wen, C. Y., Kuok, P. L., Chen, H., & Lung, M. F. (2011) Numerical Analysis of a Rapid Magnetic Microfluidic Mixer. *Electrophoresis* 329(22): 3268–76. doi:10.1002/elps.201100254.

[50] EMG Series - Water-Based Audio FerrofluidType: EMG-408 Ferrofluid: Ferrotec (2020). Retrieved on March 30, 2018, from https://ferrofluid.ferrotec.com/products/ferrofluid-emg/water/emg-408/.

[51] Hashmi, A., & Xu, J. (2014) On the Quantification of Mixing in Microfluidics. *Journal of Laboratory Automation* 19(5): 488–91. doi:10.1177/2211068214540156.

[52] Ma, Y., Chien, P. S., Fields, M., Li, Y., Haake, D. A., Churchill, B. M., & Chih, M. H. (2008) An Unsteady Microfluidic T-Form Mixer Perturbed by Hydrodynamic Pressure. *Journal of Micromechanics and Microengineering* 18(4): 045015. doi:10.1088/0960-1317/18/4/045015.

[53] Furlani, E. P., Ng, K. C. (2006) Analytical Model of Magnetic Nanoparticle Transport and Capture in the Microvasculature. *Physical Review E* 73(6). doi:10.1103/physreve.73.061919.

[54] Zhu, T., Marrero, F., & Mao, L. (2010) Continuous Separation of Non-Magnetic Particles inside Ferrofluids. *Microfluidics and Nanofluidics* 9(4-5): 1003–9. doi:10.1007/s10404-010-0616-1.

[55] Gijs, M. A. M., Frédéric, L., & Lehmann, U. (2010) Microfluidic Applications of Magnetic Particles for Biological Analysis and Catalysis. *Chemical Reviews* 110(3): 1518–63. doi:10.1021/cr9001929.

[56] Mccloskey, K. E., Chalmers, J. J., & Zborowski, M. (2003) Magnetic Cell Separation: Characterization of Magnetophoretic Mobility. *Analytical Chemistry* 75(24): 6868–74. doi:10.1021/ac034315j.

[57] Samiei, E., Nejad, H. R., & Hoorfar, M. (2015) A Dielectrophoretic-Gravity Driven Particle Focusing Technique for Digital Microfluidic Systems. *Applied Physics Letters* 106(20): 204101. doi:10.1063/1.4921630.

PUBLICATIONS

1. **Surendran, Athira N.,** Ran Zhou and Yang Lin. “Microfluidic Device for Magnetic Separation of Biological Particles: A Review.” Journal of Medical Devices, American Society of Mechanical Engineers (ASME), (2020). DOI: 10.1115/1.4048912.
2. **Surendran, Athira N.** and Ran Zhou. “Active High-Throughput Micromixer using Injected Magnetic Mixture Underneath Microfluidic Channel.” Virtual International Conference of Nanochannels, Microchannels and Minichannels 2019, Orlando, FL, USA.
3. Zhou, Ran, **Athira N. Surendran**. “Study on micromagnets induced local wavy mixing in a microfluidic channel.” Applied Physics Letter 117, (2020). DOI: 10.1063/5.0024011.
4. Zhou, Ran, **Athira N. Surendran**, Marcel Mejulu, and Yang Lin. “Rapid Microfluidic Mixer Based on Ferrofluid and Integrated Microscale NdFeB-PDMS Magnet.” *Micromachines* 11, no. 1 (December 25, 2019): 29. https://doi.org/10.3390/mi11010029.
5. Zhou, Ran, Mark Parra, and **Athira N. Surendran**. “A Low-Cost, High-Resolution Fabrication Method for a Microfluidic Device.” *International Journal of Engineering Research and Innovation* 11, no.2 (October 2019): 5.
6. Zhou, Ran, **Athira N. Surendran**. “Experimental and Numerical Study of Ferrofluid Mixing in A Double-Layer Magnetic Micromixer.” Virtual COMSOL Conference 2020 North America.